Development of Extracellular Matrix Based Biomaterials for Articular Cartilage Repair

by

Jeanne Emily Barthold

B.A., Colby College, 2015

M.S., University of Colorado Boulder, 2017

A thesis submitted to the
Faculty of the Graduate School of the
University of Colorado in partial fulfillment
of the requirement for the degree of
Doctor of Philosophy
Department of Mechanical Engineering
2020

Committee Members:

Corey Neu

Virginia Ferguson

Stephanie Bryant

Sarah Calve

Maureen Lynch

Barthold, Jeanne Emily (Ph.D., Mechanical Engineering)

Development of Extracellular Matrix Based Biomaterials for Articular Cartilage Repair

Thesis directed by Corey P. Neu, Ph.D.

Abstract

Osteoarthritis, a degenerative joint condition prevalent in the knee joint, affects over 350 million people. Following injury to articular cartilage, disease progression can be exponential; there is a significant need to develop materials that can repair cartilage defects to delay or inhibit total joint degradation. Despite decades of research, the unique architecture and function of articular cartilage is difficult to replicate, and many engineered biomaterials fail to integrate with surrounding tissue. Allografts are one of the most successful interventions, involving transplantation of osteochondral sections from a recently deceased donor to the injured defect. While allografts show promising long-term clinical data, they suffer extreme source limitations.

This thesis aims to develop extracellular matrix (ECM) based scaffolds that balance cellularity, integration, structural stability, and tissue complexity. Motivated by the success of allografts, we decellularize and evaluate an animal-derived allograft by implanting it into a sheep knee for 6 months. In this study, presented in chapter 2, acellular allografts restored native function, structural composition, surface tribology, and promoted tissue integration. Unfortunately, despite high cellularity in integration regions, few cells migrate into the allograft. In chapter 3, to address the limitations of allograft cellularity, we engineered a new scaffold by pulverizing acellular ECM into microparticles and packing particles together in a hydrogel. *In vitro* analysis of our scaffold shows that when particles are tightly packed, the modulus increases rapidly from 50kPa to over 300kPa, recapitulating the acellular allograft moduli. In cellularity studies, when chondrocytes were introduced, they migrated into microparticles and expressed genes consistent with cartilage repair. In chapter 4, having overcome the limitations of the acellular allograft by engineering a scaffold which enabled cell migration, we aimed to further mimic native cartilage by creating tissue layers. To

achieve a layered scaffold, we developed a 3D-printable bioink that maintained the packed tissue particle design from chapter 3. We printed a two-layer scaffold using the bioink: a mid-deep cartilage zone printed under a superficial zone, together recapitulating the compressive modulus and tribological properties of native tissue. We also demonstrated proof-of-concept printing of custom shapes, resulting in a potentially powerful clinical intervention for articular cartilage repair.

Dedication

For my grandfather, Lionel O. Barthold

Your lifelong love of learning has always inspired me

Acknowledgements

If 2020 has taught me anything, it is to be thankful for all the opportunities I have been given, to celebrate the small things, and to give my deepest gratitude to all of the people who have challenged me, lifted me up, and supported me unconditionally. First, I want to thank my advisor, Corey Neu. As an incoming graduate student, my background was primarily in physics, with next to no classical biology training. Corey took a chance on me, helped me dive into a new field and body of literature, and I am forever grateful. Additionally, Corey truly cared about what I wanted out of my PhD and wanted to help me get there regardless of whether it negatively impacted research productivity. For example, Corey encouraged me to take a course at the business school, attend short courses offered by our TTO, and participate in pitch competitions. While none of these activities directly led to publications, I never felt anything but encouragement from him. Finally, Corey understood and encouraged the need for balance in my life, commonly asking about what fun activity we had planned for our weekends. Thank you so much Corey. To my committee members: Ginger, Sarah, Maureen, and Stephanie, thank you for being willing to make time in your busy schedules to give me feedback, asking difficult but important questions, providing suggestions, and showing your support for me personally and professionally.

Next, I want to thank my incredible lab group—I feel so fortunate to have found a group that looks out for one another, celebrates each other's successes, and truly works together. Thanks to all of you who welcomed me into the group, gave direction and advice during lab meetings, read and edited any of my work, and performed experiments to enhance my findings. A few people deserve special recognition. Kaitlin, thank you for spending countless hours in a non-ventilated room to

collect frustrating and challenging AFM measurements on my various materials, and maintaining both humor and an optimistic attitude throughout. Ellyse, you joined the lab shortly after I did, and I can confidently say I would not be where I am in my research or sanity without you. You so patiently taught me biological assays and answered the questions I was scared to ask anyone else. You have continued to be my trusty desk mate: making me laugh, troubleshooting science, answering questions, and never forgetting a birthday. Additionally, you maintain so many parts of this lab, and we all owe you a huge amount of gratitude for keeping everything running smoothly. Adrienne, you also joined the lab the summer after I did, and I am so glad you chose us. We now have logged more knee dissections and HA troubleshooting sessions than either of us wants to count, but both were enhanced by your intelligence, positive attitude, and mutual love of country music. I feel so fortunate to have had both of you as colleagues and friends throughout this journey. Brittany, I won the undergraduate jackpot when you joined the lab and agreed to work with me. I was so fortunate to have you to work with throughout the entirety of my PhD. You always were an intelligent, motivated, and resilient person, and by the end you were also a gifted independent researcher and trusted friend to me.

I am truly grateful that I started grad school with a cohort that included David and Rachel. David, from 8AM fluids to defending within 24 hours of each other, we have muddled through this doctoral adventure together. Your spirit, generosity, inquisitive mind, and overall excitement towards learning is uplifting and admirable. I love the traditions we developed to keep us smiling throughout the last 5.5 years – random afternoon coffee catch ups, our custom PhD milestone celebration ritual, and getting lost on backpacking trips. Thank you for being a dependable, supportive, and wonderful friend. Rachel, you and I both know that I simply would not have made it this far and be writing this dissertation if it were not for you. We became fast friends right from the beginning and I cannot imagine graduate school without you. Thank you for your patience and dedication to teaching me solids, thank you for being equally as excited about making our beautiful note sheets for exams as you were about the post exam hike (regardless of how dark it was getting) or mid study break bike ride. Thank you for not pretending grad school was a breeze

and for making me feel I was not the only one with impostor syndrome. Thank you for being my adventure buddy from day 1 and most of all thank you for your steadfast friendship and support.

Last, but certainly not least, thank you to my family. From a young age, you instilled in me the value of learning and pursuing an education. Yet, you managed to do this without micromanaging, never checking our report cards, and encouraging all the extracurriculars. You put your trust in me and taught me the importance of education by being role models, not managers. For the past five years, you have put up with my infrequent calls and visits – instead coming to see me and always showing me that you are proud of me no matter what. Eric, you have always been my number one fan. I am so thankful you moved to Colorado so that we could play outside and forget our stress. Thank you for being you and for always being there. Joe, you are both my rock and my sunshine. I am certain I would have failed to complete my PhD if it were not for your example, encouragement, humor, goofiness, excitement about adventure, and unconditional love. Simply put, life is so much more fun with you by my side. In the last few months, despite your own stress of managing two jobs and work for a future job, you have accepted and consoled me during breakdowns, and managed to always leave me laughing. I am forever grateful to all you do for me and am so beyond thankful that you waited in Boulder for me to finish my PhD, as I cannot imagine life without you by my side.

Funding Sources that made this research possible: DoD/CDMRP W81XWH-20-1-0268, NIH R01 AR063712, NSF CMMI CAREER 1349735, Lab Venture Challenge (OEDIT/State of Colorado), and the Research and Innovation Office at CU Boulder.

Contents

Chapter

Figures

Figure

Chapter 1

Introduction

1.1 Prevalence and Significance of Knee Osteoarthritis

Osteoarthritis (OA) is a degenerative condition in any joint region (hands, hip, knee, spine, and feet). The most common form of osteoarthritis is found in the knee joint and can be caused by a variety of events that lead to a breakdown of the joint cartilage. OA is associated with mechanical and biochemical degradation of tissue in the knee joint including the underlying subchondral bone, synovial fluid within the joint, and the articular cartilage lining the bone. Osteoarthritis is typically seen as degradation of the articular cartilage lining the bone which leads eventually to a very painful bone on bone joint articulation at the latest stages of the disease. However, other tissues surrounding the cartilage play a significant role in the degradation – thus many consider OA an entire joint failure or whole organ disease [1]. OA can be an extremely painful disease and is difficult to diagnose at early stages of degradation.

The onset of OA can be caused from a traumatic event or injury to the joint, uneven loading from unusual hip mechanics, or excessive wear and tear that is prevalent in aging and obese populations. Acute events such as joint trauma, commonly seen in conjunction with ACL or meniscal tears, can cause immediate damage to the articular surface, increasing the risk of developing OA. At the time of trauma, the ECM is damaged, cells lyse, and ECM fragments are released into the joint space [2]. The absence of blood and the high density of articular cartilage tissue hinders subsequent cellular migration, remodeling, and strengthening of the damaged zone [3]. The increase in cartilage damage leads to stress localization, inferior lubricating properties, and upregulation of

a host of catabolic cascades without the necessary cell population to process them, thereby leaving the joint more susceptible to further mechanical degradation throughout everyday movement, initiating long term cartilage loss and OA progression [3].

For the past few years, OA has been cited as the primary cause for disability, and affects 350 million individuals worldwide [4]. In the United States alone, 32.5 million adults suffer from osteoarthritis pain and a clinical osteoarthritis diagnosis [5]. The numbers of patients diagnosed with clinical OA each year are continuously increasing due to longer life expectancy as well as a growing obese population. Patients living with OA can have moderate to severe restrictions on their abilities to perform daily tasks as well as a decreased quality of life.

Not only does OA place a large burden on the daily life of the patient, OA also costs society a tremendous amount economically. Osteoarthritis is the second most common condition resulting in Social Security disability benefits (after heart disease), and has an estimated cost of over $100 billion to US society [6]. The United States Bone and Joint Initiative states that from 2013-2015, adults with arthritis reported 180.9 million lost workdays (34% of total lost work days for any medical condition). Furthermore, it is estimated that medical cost for OA per person from 2008 to 2014 averaged $11,052. Finally, total knee replacements cost $41.7 billion in 2013 alone [7]. Osteoarthritis is a widespread condition that has a tremendously negative impact on both patient and economy. As a result, in 2016 the FDA changed the status of OA and now classifies it as a serious disease: "a disease or condition associated with morbidity that has a substantial impact on day-to-day functioning..." (21 CFR 312.300). This change in classification will hopefully lead to a faster FDA path for devices and therapeutics which could, in turn, improve diagnosis and treatment options for patients suffering from OA.

1.2 Articular Cartilage Structure and Function

Articular cartilage is composed of a specific multi-layer macromolecular structure of interwoven collagens, proteoglycans, and water that vary throughout the depth of the cartilage (Figure 1.1). The zone closest to the surface of the articular cartilage is known as the superficial zone and

represents the top 10-20% of the tissue. The superficial zone is composed of mostly water, collagen, and chondrocytes, oriented parallel to the surface of the tissue, and packed closely together. The middle zone is the region below the superficial zone and accounts for 40-60% of the tissue depth. The middle zone is composed of collagen fibers, aggrecan, and water. Collagen fibers in the middle zone are less densely packed, have wider diameter fibers, and are more randomly oriented than the parallel tightly packed fibers found in the superficial zone [8]. Aggrecan content is at its maximum in the middle zone and interacts with the collagen fibers to create a network that maintains the homeostasis of the water content. The final 30% of the articular cartilage tissue is known as the deep zone where the collagen fibers are woven together in fiber bundles that lie perpendicular to the bone below and aid in anchoring the cartilage to the bone [9].

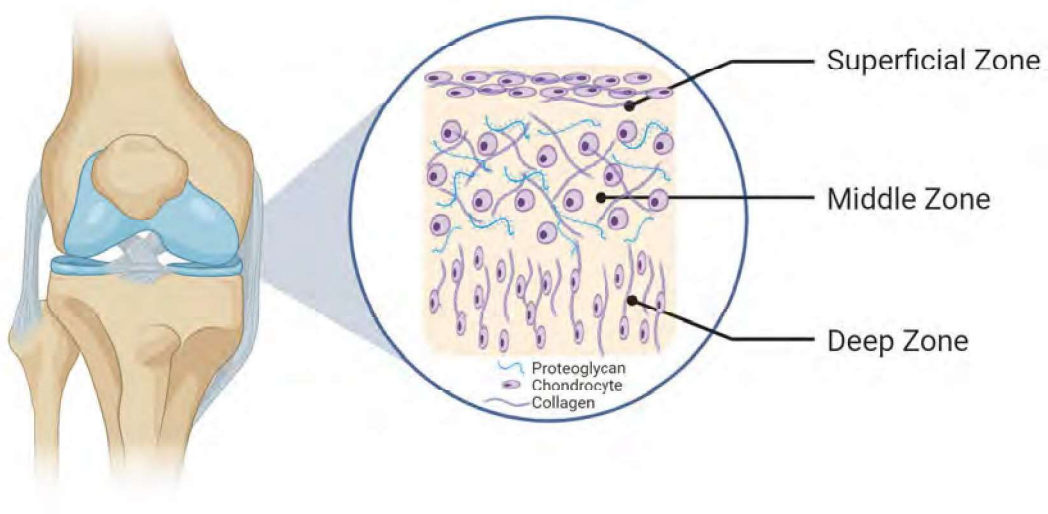

Figure 1.1: Articular cartilage is composed of three distinct layers. Each layer has unique molecular structure, fibril orientation, and cellular density. *Figure created with BioRender.com*

The specific composition of the tissue enables articular cartilage to provide joint lubrication and facilitate load transmission during normal movement. The superficial zone is exposed to the highest levels of stress, and therefore the parallel collagen fibers in the superficial zone allow it to resist shear forces that are inevitable in regular joint use. Additionally, the large amount of water, in addition to a unique superficial zone protein known as lubricin, lubricates the surface of

the superficial zone under compression [9]. In the middle zone, the aggrecan and collagen interact to play a critical role in enabling effective force distribution. Aggrecan is composed of many negatively charged groups that create a large osmotic pressure in the cartilage tissue to draw water into the matrix. The collagen stretches with this swelling until the tension in the collagen network balances the osmotic pressure, and the tissue maintains a state of equilibrium until the next loading event (Figure 1.2) [10]. Under typical loading events (e.g. walking), the tissue alternates between extension and compression. Extension of the joint enables the articular cartilage to absorb nutrients from synovial fluid while compression expels degradation products and waste [11].

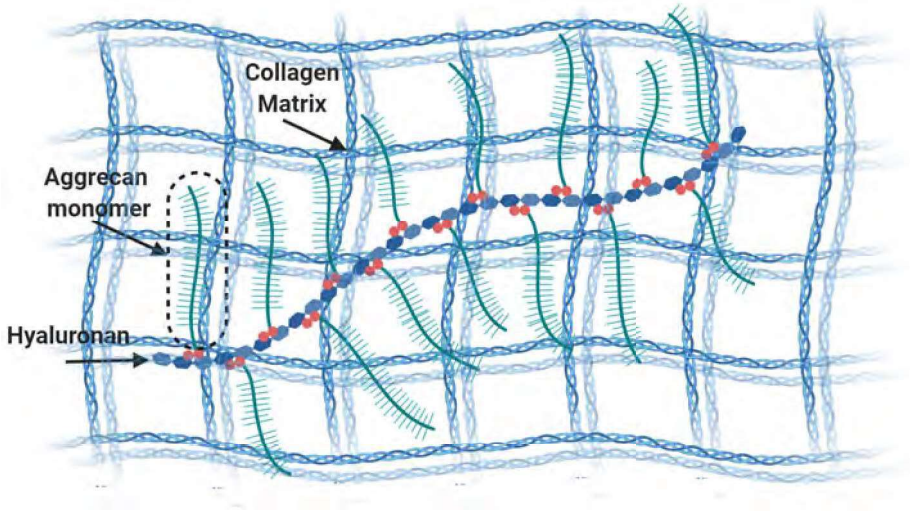

Figure 1.2: The unique structure of articular cartilage enables load dissipation, and homeostasis of the tissue. Negatively charged groups on the aggrecan monomer draw water into the matrix to swell the tissue. The surrounding collagen mesh network limits this swelling. The balance of these two components is critical for cartilage homeostasis and loading. *Figure created with BioRender.com*

Chondrocytes, the characteristic cell type of articular cartilage, attach to the tissue matrix via cell surface receptors (CD44) and maintain regional homeostasis of the extracellular matrix (ECM) through a cycle of continual degradation and synthesis. The orientation of chondrocytes in each layer of the tissue reflect the orientation of the collagen fibers (parallel to surface and tightly packed in the superficial zone, round in middle zone, and vertical/sparse in the deep zone). Within the articular cartilage ECM, chondrocytes are surrounded by a different, structurally distinct matrix,

known as the pericellular matrix (PCM). The PCM is approximately 2-4 µm thick and is composed of type VI collagen, fibronectin 1, perlecan, and biglycan [12]. Several studies show that the PCM communicates and filters biochemical or mechanical signals from the ECM to the chondrocyte, and is therefore seen as an key mediator in mechanotransduction [12]. The PCM also regulates cell behavior because it can sequester, transport, and activate growth factors [13].

Degradation of articular cartilage, as found in osteoarthritic joints, leads to a rapid breakdown of aggrecan, which in turn disrupts the ability of the tissue to maintain the osmotic pressure and swelling balance. The lack of homeostasis in the joint become a positive feedback cycle, and the structure breaks down rapidly, leading to an inability to handle typical loads. For patients, the breakdown of articular cartilage tissue leads to irreversible pain and loss of function in their joints.

1.3 Treatment of Osteoarthritis

Patients who suffer from osteoarthritis have few effective treatment options other than a total knee replacement. Typically, totally knee replacements only last about 15-20 years, and therefore many patients live with painful OA for many years before replacing the knee joint [14]. On average, patients live with symptomatic OA for 28.4 years before surgical intervention [15]. The best non-surgical options for pain reduction are physical therapy, steroidal or hyaluronic acid injections, and weight loss. Physical therapy reduces pain and increases function through the strengthening of supporting muscles that decrease the load on the joint, working on knee-hip alignment to redistribute loads, and managing swelling or scar tissue build up in the joint. Furthermore, load reducing braces and cushioning footwear can decrease pain [16]. For aging patients, physical therapy becomes increasingly important, as the ratio of muscle mass to fat mass changes with age [17].

Current pharmacologic solutions include non-opioid and opioid analgesics, non-steroidal anti-inflammatory drugs (NSAIDs), COX-2 specific NSAIDs, topical agents, and injections of corticosteroids or hyaluronic acid. Analgesics and NSAIDs are medications that limit pain by reducing inflammation, but these medications do not mitigate further degradation in the joint and the pain relief is temporary. The injection of different forms of corticosteroids or hyaluronic acid have long

been used to alleviate OA symptoms, but their pain reductions seem to also be temporary and play no role in preventing degradation [16].

One of the most successful pain management techniques for patients suffering from OA is weight loss [18]. For every 1lb of weight loss, there is a 4lb decrease in knee compressive forces per step [19]. In a recent clinical trial in obese populations, researchers found that losing greater than 15% body weight resulted in dramatically improved osteoarthritis pain scores, as well as improved the ability to complete daily tasks without pain [20].

1.4 Surgical Treatment Options

Current treatments for cartilage defects range from maintenance (physical therapy) to complete repair (total knee replacement), but repair for small defects in early stages of knee osteoarthritis remain largely non-effective. The 'gold standard' cartilage defect repair procedure is known as microfracture, where a surgeon drills into the bone marrow to stimulate cells to fill the defect space. This procedure creates a blood clot in the cartilage defect that eventually becomes cartilaginous. However, microfracture promotes fibro-cartilage formation, a very different type of cartilage than the smooth hyaline cartilage that is inherent in articular joint spaces. Therefore, microfracture is largely unsuccessful at reducing pain and maintaining long term healing in the joint space [21]. Furthermore, microfracture is only able to repair defects of $< 2cm^2$ [22].

Over the last few decades, other cell and tissue-based therapies emerged with the goal of providing a better healing outcome than is achieved with microfracture (Figure 1.3). For focal defects about $2 - 3cm^2$ in size, mosaicplasty and autologous chondrocyte implantation aim to provide a long-term solution. Mosaicplasty (autograft) is a transplant from a non-load bearing region of cartilage to the defect. Surgeons take a defined size biopsy punch of 2-3 cm from the very edge of the articular cartilage region and implant it into the region of degradation [23]. Using a very different approach, autologous chondrocyte implantation (ACI) is a two-surgery, cell-based approach to fill defects. In ACI, a small biopsy of cartilage is taken from the patient in an initial surgery. The cartilage cells (chondrocytes) are then extracted from the biopsy and expanded in-vitro

until cell numbers reach a critical number to implant back into the patient. In the second surgery, the expanded cells are injected into the defect space and secured with a periosteal flap. The goal is to allow the patient's own cells to regenerate new cartilage matrix in the defect space. More recently, an adaptation of ACI (MACI: Matrix assisted autologous chondrocyte implantation) has become more popular. The procedure is identical, except expanded cells are seeded into a 3D chondrogenic matrix before implantation back into the patient [24]. Unfortunately, neither procedure has shown significant advantages over microfracture in several comparative studies [25, 26, 27, 28] and both have significant drawbacks: Mosaicplasty leaves a new area of cartilage susceptible to inflammation and degradation, and ACI/MACI is very expensive and puts the patient at increased risk due to the inherent risks of multiple surgeries. In more advanced cases, when patients have a focal

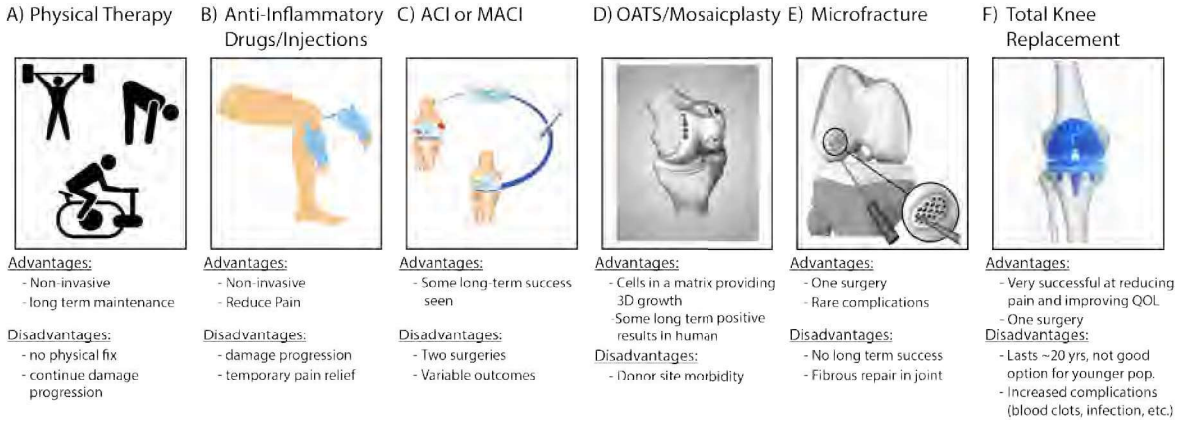

Figure 1.3: Osteoarthritis can be treated in a variety of ways, from noninvasive to extremely invasive procedures. Many patients with OA can manage pain through physical therapy (A) or infrequent anti-inflammatory injections (B). Surgical options include ACI (C), OATS, Mosaicplasty (D), Microfracture (E), or an entire knee replacement once a patient reaches late stages of OA.

defect of $4cm^2$ or multiple defect regions, the best option is an allograft: a transplant from the articular cartilage of a recently deceased patient to a living patient (Figure 1.3). The edges of the defect region are cleaned up, and the transplant plug is press fit into the region of need. Allograft procedures do show improvements over previously discussed procedures, however there is limited availability of healthy donor articular cartilage since aging has a profound effect on cartilage even

in patients without OA [29]. Therefore, young articular cartilage is ideal for allografts, and this is thankfully a very limited resource. Finally, once the degradation in the joint covers almost the entire surface area of articular cartilage, total joint replacement is the only option. Total knee replacements are an extremely invasive surgery, where the entire joint is removed and replaced with an artificial joint. Total knee replacements are successful at removing a patient's pain and improving quality of life, but these procedures are only recommended to patients over the age of 60 due to the increased complication rate of revision surgeries [30, 31].

1.5 Articular Cartilage Design Parameters

Cartilage is an avascular, low density cellular tissue, and therefore researchers originally thought it would be the easiest tissue to engineer [11]. Unfortunately, successfully replicating the structure/function relationship of articular cartilage is still an elusive challenge, despite many decades of innovation. The largest hurdles, or challenges, that ultimately lead to failure of tissue engineered scaffolds are (1) lack of integration with native tissue, (2) inability to match the mechanics and participate in the sophisticated load transfer of the joint, and (3) production of type I collagen heavy fibrocartilage, rather than the essential collagen II dominant hyaline cartilage. For efficient and effective restoration of a chondral defect, there exists a significant need to develop a scaffold which mimics mature articular cartilage chemically, structurally, biologically, and mechanically; previous engineering scaffolds meet only one or two critical elements [32]. From a mechanical standpoint, engineered scaffolds need to show compressive and shear moduli similar to native tissue to ensure they do not break down immediately after implantation. Additionally, it is critical that the material integrates with the surrounding tissue in a manner that enables layer specific load transmission. Structurally, in addition to physical integration with native tissue, engineered scaffolds must demonstrate macroscopic zonal architecture and microscopic radial structure of collagen fibers. Scaffolds also must have an interconnected pore structure to allow diffusion of nutrients and waste throughout the tissue layers. Biologically and chemically, the scaffold must enable or incorporate distribution and regulation of native growth factors (TGF-β, FGF, IGF, BMP-2), have

a biodegradation rate that matches the production of ECM, provide cellular attachment sites with signaling and regulation mimicking the unique pericellular matrix, and demonstrate a biomimetic cell distribution throughout the thickness [32, 33]. The first scaffold that can integrate with native tissue (from superficial zone all the way through to subchondral bone), show biomimetic cellularity, and structurally support the unique mechanics of articular cartilage will likely show improved regeneration of hyaline articular cartilage over current surgical or engineered scaffolds.

1.6 Aims and Objectives

The overall objective of my dissertation work is to investigate the tradeoffs of articular cartilage design principles on several length scales both *in vitro* and *in vivo* to develop a platform that balances and optimizes the necessary biological and mechanical properties for articular cartilage. This work is centered around the concept that acellular native articular cartilage provides the best combination of mechanics and complex architecture for critical defect repair of articular cartilage. However, I aim to define limits and develop extracellular matrix-based scaffolds that balance migration, cellularity, integration, structural stability, and tissue complexity.

Aim 1: Evaluate a repair efficacy of an acellular allograft implanted in the load-bearing region of a sheep condyle for 6 months.

- Define the structure, mechanics, and function of an acellular allograft implanted in a sheep knee for 6 months.
- Quantify recellularization and extracellular matrix deposition throughout the integration region and implant.

Aim 2: Develop a decellularized cartilage scaffold that enables cellular migration, supports biomimetic mechanics, and maintains hyaline cartilage specific composition.

- Develop a decellularized microparticulated tissue scaffold in a chondrogenic hydrogel.
- Define the effect of particle packing density on scaffold mechanics and cellular behavior.

Aim 3: Optimize microparticulated tissue to create a natural, ECM based bioink that recapitulates the zonal macrostructure of articular cartilage using 3D printing.

- Adapt and optimize the microparticulate scaffold design for use as a 3D-printed bio-ink.
- Develop layered constructs that mimic the depth dependent structure and function of native cartilage and enable cell migration and viability.

Chapter 2

Acellular Cartilage-Bone Allografts Engineered for Long-Term Mechanical Function and Integrative Repair

2.1 Abstract

Articular cartilage repair after damage is challenging due to the avascular nature and dense matrix of the tissue, and clinical interventions to promote regeneration remain elusive. The most effective long-term treatment to delay a full joint replacement is an osteochondral allograft, where tissue is sourced from a recently deceased donor and implanted into the injury site. However, this treatment option suffers from severe source limitations and short storage time between donor death and implantation. As a solution, decellularized osteochondral tissue provides the same tissue structure and composition without source or storage limitations, as it is acellular and allows the use of allogenic or xenogenic tissue. However, the long-term efficacy of acellular allografts is unknown. Here, we show that acellular osteochondral implants restore functional and integrative cartilage repair in defect regions after 6 months in mature sheep. Compared to untreated tissue defects, *in vivo* structural, compositional, and tribological analysis show acellular allografts restore surface roughness and lubrication, mimic native cartilage modulus under compression and relaxation, conserve the cartilage compositional ratios of collagen:glycosaminoglycan and collagen:phosphate, and integrate laterally with both bone and cartilage. Our results demonstrate the efficacy of acellular allografts as an effective cartilage repair solution with high translational potential for the treatment of severe osteochondral damage of the articulating joints.

2.2 Introduction

Articular cartilage is a vital mechanically loaded avascular tissue within the knee joint. Injury or damage to the articular cartilage does not spontaneously heal and can lead to a painful condition known as osteoarthritis (OA). The loss of cartilage due to disease or overuse leads to an inability for the remaining tissue to compress or lubricate joints properly when exposed to mechanical loading. In the United States, over 32 million people suffer from osteoarthritis of the knee [34] and the majority of those affected experience a lower quality of life and loss of function due to the associated knee pain. While there are medical treatments and surgical approaches to ameliorate the pain and loss of function, the only option to completely treat the condition and restore function is a total knee replacement. The most robust knee replacements typically only last 15-20 years [14], which is problematic since over 50% of patients requiring treatment for osteoarthritis of the knee are under the age of 65 [35].

A variety of alternative procedures are available to delay the need for a total knee replacement. Unfortunately, in most patients these procedures do not significantly repair cartilage defects and fail to adequately improve pain or joint functionality. Osteochondral allograft procedures, in which a surgeon transplants healthy cartilage from the knee of a recently deceased young donor into a cartilage defect, lead to decreased pain and improved function for approximately 10 years in 80% of patients [36]. Unfortunately, the quantity of osteochondral allografts available is severely limited by reliance on healthy donor cartilage, the need for immediate harvest and implant into recipient for optimal success [37], and the resulting lack of advanced notice available for planning the procedure.

Considering the increase in patients with OA [7], there exists a substantial need for cartilage defect therapies that delay a total joint replacement, can be delivered in one surgery, have a long shelf life, and functionally repair the cartilage damage. Acellular osteochondral implants, where bone and cartilage tissue are taken together from a donor knee and processed to strip away all cellular material, preserve the complex architecture and molecular composition of an osteochondral allograft. Thus, decellularization and associated processing represent a straightforward and

relatively simple method of acellular allograft preparation, while providing the ideal natural tissue scaffold for regeneration. Though an acellular osteochondral implant maintains the structural and compositional properties of native cartilage, and is perhaps the most ideal scaffold that could be envisioned, the tightknit extracellular matrix proteins of articular cartilage make it unclear whether implants will integrate into the surrounding tissue to provide long-term function and repair. This study was designed to directly test the long-term efficacy of allograft tissue, decellularized with minimal processing to retain structure and composition, and implanted into a critical size defect. Here we aim to define the acellular allograft repair by investigating the structure, composition, function, and integration of the implant in a common large animal, sheep (ovine), model after 6 months *in vivo*.

We have previously evaluated acellular allografts in short-term studies and demonstrated limited integration and penetration of chondrocytes into the implant [38]. However, these studies were of inadequate duration and location as the implantation and analysis was conducted in non-load bearing regions at only 3 months post-surgery. Further *in vivo* investigation is needed to determine the success of a decellularized osteochondral plug in the load bearing region of the femoral condyle. Understanding the long-term behavior and repair of a scaffold in a large animal model is paramount for predicting clinical success in humans. In this work, we evaluated the functionality of six implants after 6 months in a critical sized defect model in mature sheep. We prepare acellular allografts with minimal processing, just to remove cellular components, while maintaining important cartilage specific structural layers, mechanics, and heterogenous composition throughout the depth of the tissue (Figure 2.1). We define the functional, structural, and mechanical characteristics of the osteochondral repair, integration zone between implant and native tissue, and the surrounding tissue using a myriad of analysis techniques. We successfully show that acellular allografts result in a functional and integrative osteochondral repair with immense potential for clinical translation.

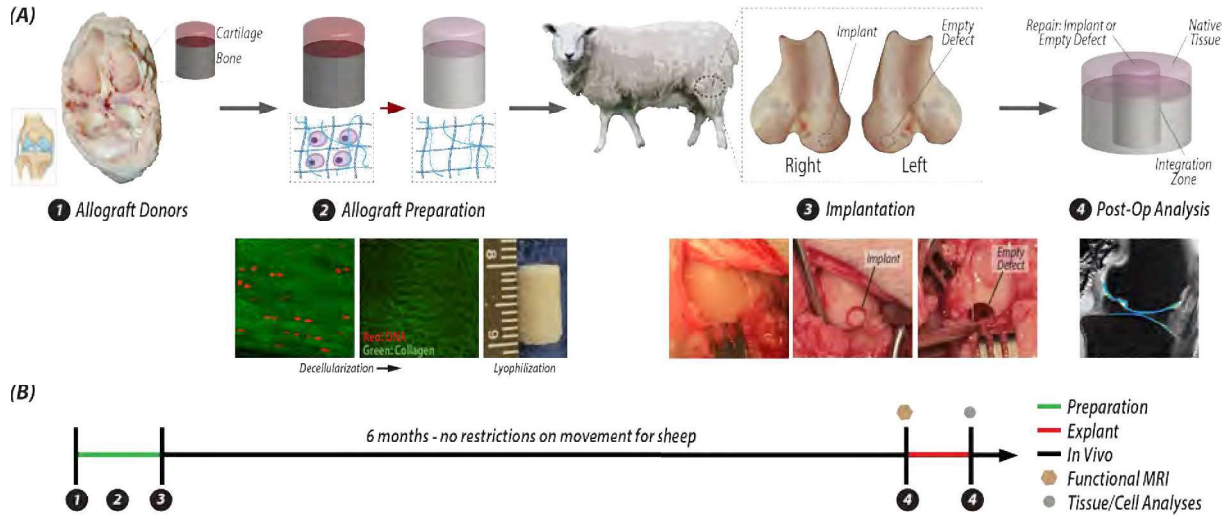

Figure 2.1: Tissue engineering strategy for integrative osteochondral repair, sheep surgery, and experimental timeline. (A) Osteochondral allografts were extracted from donor sheep, and then were decellularized, lyophilized, and stored for surgery. During the surgery, the joints of recipient sheep were opened and a defect was made in each femoral condyle. On the left side, the defect was left empty and on the right limb, the defect was filled with an acellular osteochondral allograft. After 6 months, the repair tissue with surrounding native tissue is excised from both joints and anylized. (B) Timeline illustration of the steps in (A) and illustrating the sequential analysis process: whole joint MRI followed by tissue- and cell-level analyses.

2.3 Results

2.3.1 Implant architecture and structure recapitulate native tissue

To evaluate the structure and architecture of implant and defect repair, we analyzed fixed tissue slices with histological staining and previously frozen tissue sections using Raman spectroscopy to define compositional elements of the repair. After 6 months *in vivo*, hematoxylin and eosin staining show that implants maintain a distinct tidemark, with key division between cartilage and bone regions (Figure 2.2). When implanted tightly next to native tissue, implants also maintain surface continuity from implant to native tissue. The implants closely recapitulate the thickness and typical distinct zonal layers of articular cartilage. Each cartilage zone possesses key structural differences which are essential to recapitulate articular cartilage function. In contrast, defect repair fails to maintain a smooth surface with native cartilage, instead displaying a dip in the surface even in the most successful empty joint repair (Figure 2.2). While the implants maintain surface continuity with the native tissue, there is only minimal glycosaminoglycan (GAG) expression in the cartilage layer of all repairs: the implants and most of the defects (Figure 2.2).

In terms of composition, the implant and defect repair manifest key differences. We compared the amplitude of common peaks identified from Raman spectra [39, 40, 41, 42] for collagen, chondroitin sulfate, phosphate, and non-collagenous proteins on the surface of three regions in each joint: native cartilage, integration zone, and tissue (i.e., implant or defect) repair (Figure 2.2). We found consistency across all native tissue, despite whether the joint had an implant or a defect. Native tissue displays a collagen to chondroitin sulfate (CS) ratio of 2, a collagen to phosphate ratio of 14, and a collagen to non-collagenous proteins of about 1.3. The implants contain a very similar composition to the native tissue: a collagen to CS ratio of 1.6, a collagen to phosphate ratio of 15, and a collagen to non-collagenous proteins ratio of 2.1. Alternatively, the composition of the defect repair is different, especially in phosphate content, an indicator of mineralization: we measure a collagen to CS ratio of 1.1, a collagen to phosphate ratio of 2.9, and a collagen to non-collagenous ratio of 2.8 (Figure 2.2). The change in collagen to phosphate ratio from 14-15 in

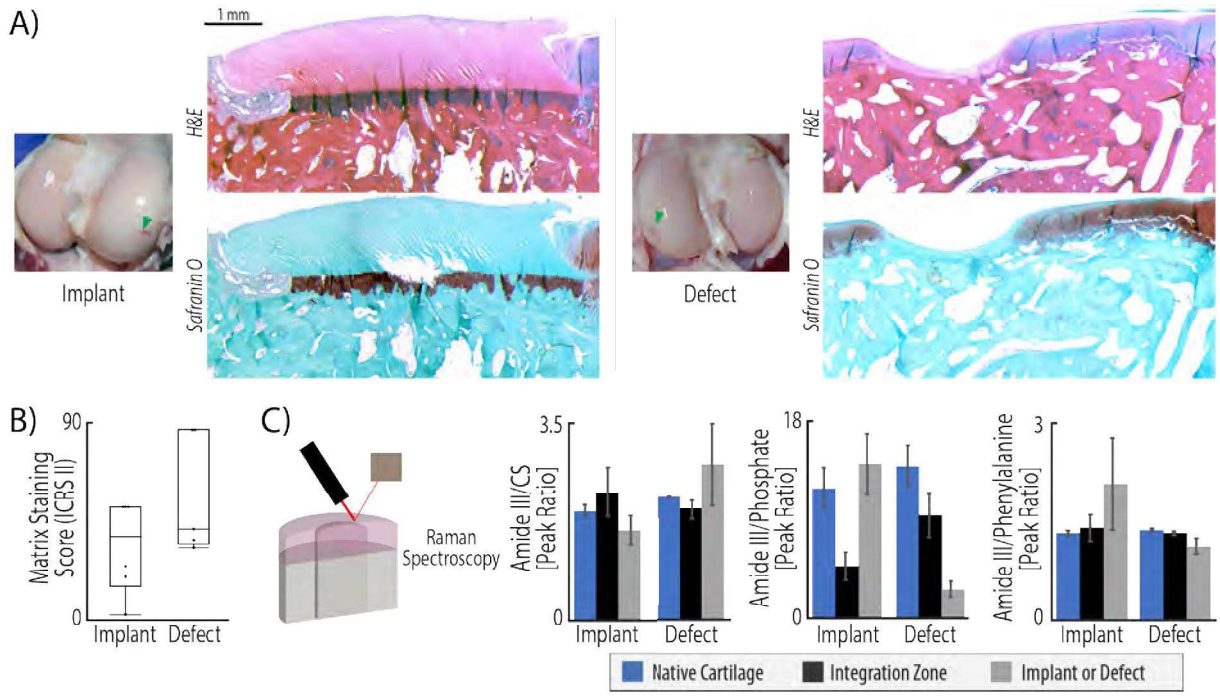

Figure 2.2: Structure and composition of implants closely matched native tissue. (A) H&E staining illustrates that the implant fills the injury void and maintains both cartilage structure and surface continuity with native tissue. In contrast, defect repair produces a much thinner layer of repair and lacks surface continuity. Safranin-O/fast green staining demonstrated that acellular allografts fail to maintain many glycosaminoglycans (GAGs), which is a known consequence of decellularization (GAGs stain red). (B) ICRS II scoring of metachromasia, or matrix staining, was evaluated in safranin-O and fast green tissue stained slices. Full metachromasia (a score of 100) would be native tissue distribution of glycosaminoglycans (GAGs). Both repair types display matrix staining scores around 50, illustrating some GAG staining in the repair, but far from native levels. (C) Raman spectroscopy quantifies compositional differences between the two types of repair. The collagen to chondroitin sulfate (Amide III/CS) ratio indicates higher levels of relative collagen in the defect repair and integration zones, while native and implant tissue maintain similar ratios of collagen to chondroitin sulfate. The increase of collagen in the defect repair suggest that these regions are repaired with fibrotic tissue. Additionally, defect repair and integration regions are highly mineralized compared to native tissue and implant repair (ratio of 3 vs. a ratio of 15), indicated by the Amide III/Phosphate ratio. While not statistically significant ($p < 0.05$) due to the high levels of variance in samples of each group, the trends indicate that implant tissue structure and composition matches native tissue. (n=6, statistics run with a two-way ANOVA test to determine cofactor significance, followed by a Tukey's honest significant difference test to determine p-values between implant types or tissue zones).

the implant and native tissue to 2.9 in defect repair is dramatic and indicates that defect repair is highly mineralized. High quantities of phosphate lead chondrocytes towards apoptosis, the first step in endochondral ossification and bone formation [43]. The integration zone between implants and native tissue mimics the mineralized composition of tissue found in the defect. This parallel composition of the defect and integration zone makes sense, as the gaps between implants and native tissue fill with the same blood and bone marrow components that make up the defect repair.

2.3.2 Implants restore key mechanical and tribological properties of cartilage

To determine whether the mechanical properties in the repair match native tissue, we quantified elastic and relaxation moduli using indentation and measured surface tribological properties with atomic force microscopy. The implant does not demonstrate differences from native tissue under compression, demonstrating a linear elastic modulus under compression of 393 kPa and a relaxation modulus of 120 kPa, compared to native tissue moduli of 321 kPa linear elastic and 148 kPa relaxation, respectively ($p< 0.05$) (Figure 2.3). Defect repair shows a linear elastic modulus of 414 kPa under compression, and while not significant ($p< 0.05$), the equilibrium modulus does not reflect the typical drop expected in the viscoelastic articular cartilage and is nearly the same as the linear elastic modulus at 316 kPa (Figure 2.3). The bulk mechanical profile of the defect repair supports the Raman compositional results positing that the defect repair is fibrotic, high in mineral content, and thus displays limited tissue relaxation.

The surface of native articular cartilage plays a vital role in the function of the tissue under loading and movement. Here, we use atomic force microscopy (AFM) and show that the implant restores surface roughness and friction to values nearing native tissue (Figure 2.3). We measure a surface roughness on the implant of 300nm which is close to the 321nm roughness measurement on native tissue, and matches previously reported roughness values of the cartilage surface [44, 38]. In the defect repair, we measure a significantly higher ($p< 0.001$) surface roughness of 500nm (Figure 2.3). Importantly, we measure a frictional coefficient on the implant surface of 0.43, not significantly different from the native tissue frictional coefficient on both types of joints, 0.28 in the defect joint

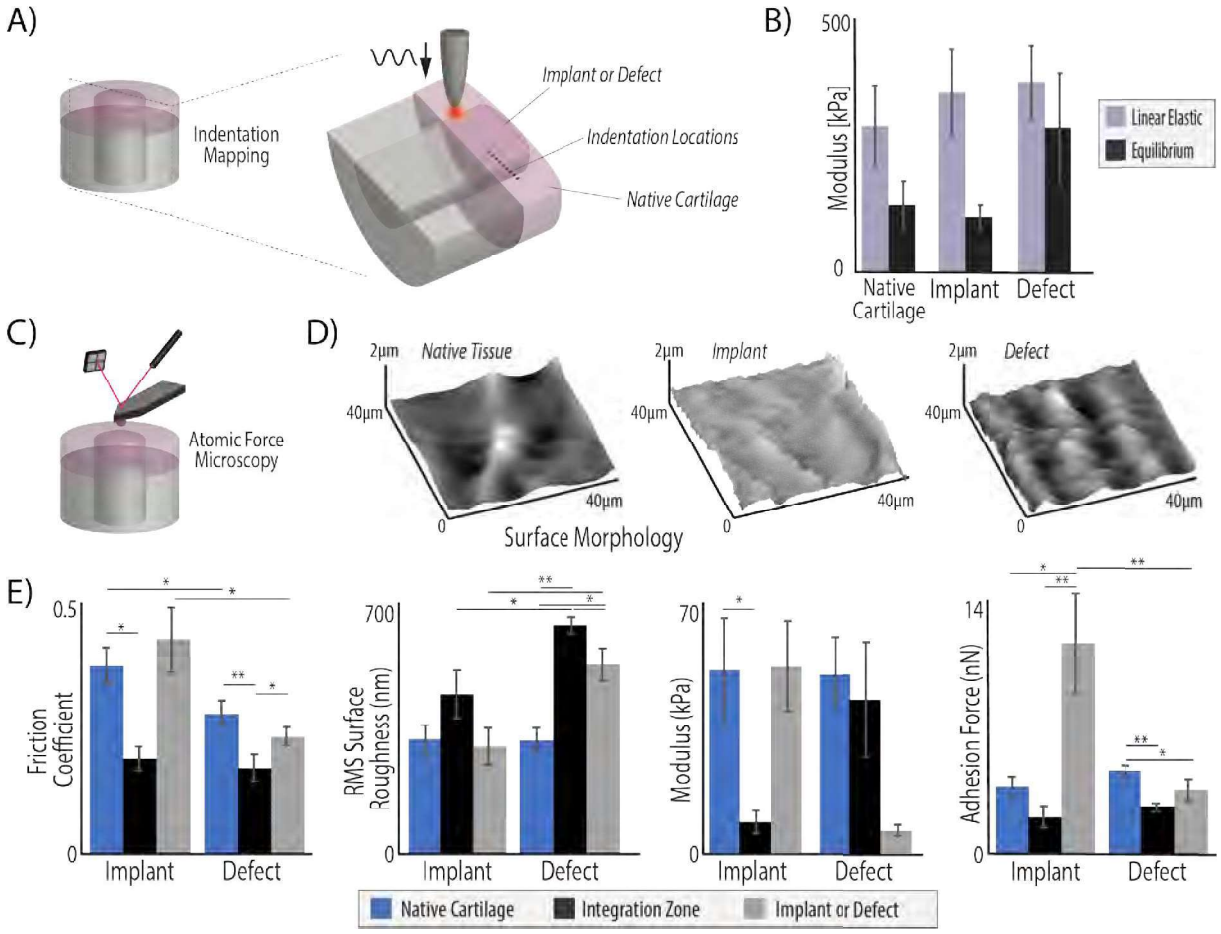

Figure 2.3: Acellular allografts restore native cartilage mechanical and surface properties. Acellular osteochondral allografts, but not untreated defects, achieved mechanical and tribological surface properties of surrounding native tissue regions. (A) Bulk tissue analysis was performed using indentation (100 µm tip) in the middle zone of cartilage on all explanted tissues at nine, evenly spaced (200 µm apart) locations, centered around the integration zone. (B) The linear elastic moduli under indent compression was consistent among the different implants and native tissue, but the defect tissue fails to demonstrate much relaxation, where the implant behaved identically to native tissue (equilibrium moduli= approx. 100 kPa). The measurements from all four points in each tissue region were averaged, resulting in a representative value for the whole tissue region but leading to increased standard deviations. (C) Atomic force microscopy (AFM) was performed with a 2 µm spherical probe to (D) map the surface of each analysis region and (E) quantify frictional coefficients, surface roughness, micro moduli, and adhesion force. The implant tissue restored native values of friction, surface roughness, and micro moduli. In contrast, the surface roughness and modulus of defect repair and integration regions were significantly different than native tissue. (*$p < 0.05$, **$p < 0.001$, n=6, statistics run with a two-way ANOVA test to determine cofactor significance, followed by a Tukey's honest significant difference test to determine p-values between implant types or tissue zones).

and 0.38 in the implant joints ($p > 0.05$). The micro level elastic modulus under compression indicates similarities between native tissue and the implant with a much softer measurement in the defect tissue (50-51 kPa on native tissue surface, 52 kPa on implant surface, 6.5 kPa on defect surface) (Figure 2.3). All the tribological properties we measure of the integration zone are very similar to the defect repair, confirming Raman and histological findings showing that any distinct space between implant and native tissue will fill with the fibrotic, mineralized material found in the defect.

2.3.3 Bone regions of acellular allograft functionally integrate with native tissue

To investigate the integration and quality of repair in the bone region of the different repairs, we analyzed microCT images to quantify bone volume fraction, trabecular thickness, and trabecular spacing throughout the repair and integration regions. We observe integration of the bone regions with native tissue in the implant and defect joints. However, the bone beneath the implant displays thicker trabeculae, smaller trabecular space, and increased bone volume fraction compared to defect joints (Figure 2.4). Furthermore, the bone material properties of the implant are not significantly different than the native tissue. On the contrary, in defect joints, both the bone volume fraction and trabecular thickness are significantly lower in defect repair than native tissue (Figure 2.4). The increase of these parameters in implant tissue indicate that the bone is experiencing loading, which in turn provides signals for the bone to remodel and strengthen trabeculae. The bone profiles we measure here provide one potential mechanism, and support, to the MRI conclusions that the implant experiences loading and successfully dissipates the force. We also observe in the histology that the cartilage regions of the defect repair are recessed from the surface. As a result, the tissue in the defect experiences less loading and therefore the bone has thin trabeculae spaced far apart with a low bone volume fraction.

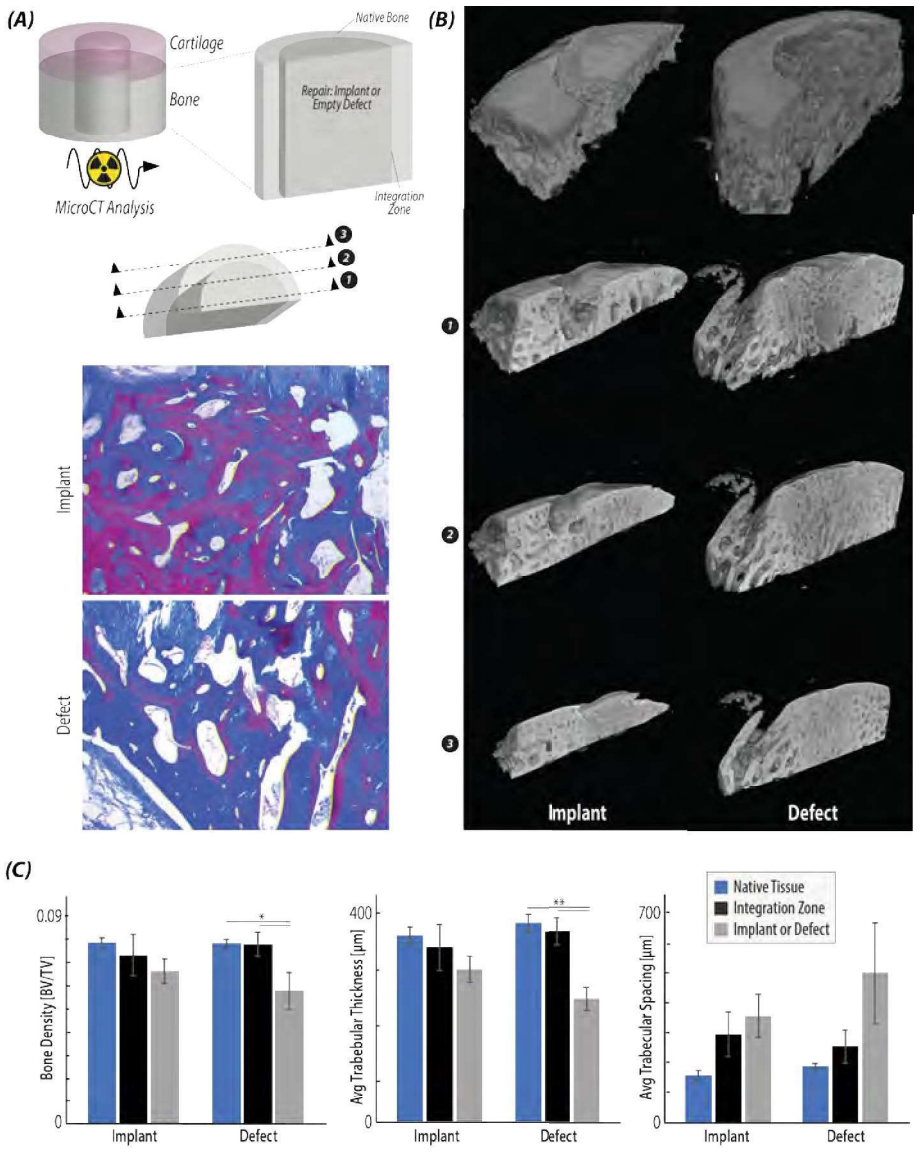

Figure 2.4: Acellular allografts demonstrate bony integration with native tissue. (A) Radiographic (μCT) analysis was used to visualize and quantify bone regions of the native tissue, integration zone, and repair tissue (i.e., implant or defect). Masson's Trichrome histological stain was used to visualize 2D regions of the bone in each type of repair (implant/defect) (B) Reconstructed μCT scans of each type of repair show that the bone regions of the implant repair maintain surface continuity and a subchondral bone layer, while the defect tissue does not contain the thin upper layer of subchondral bone. Reconstructed slices from the bisected plane towards the outside of the implant/defect confirms the histological images in (A), as the trabeculae are thicker in the implant repair than the defect. (C) Quantification of the bone volume/tissue volume, the average trabecular thickness, and the average trabecular spacing in each of the regions of interest confirms that the defect repair contains a significantly decreased bone tissue volume and trabecular thickness, while the implant repair is not significantly different from native tissue. (*$p < 0.05$, **$p < 0.001$, n=6, statistics run with a two-way ANOVA test to determine co-factor significance, followed by a Tukey's honest significant difference test to determine p-values between implant types or tissue zones)

2.3.4 Implants lack cellularity but display interfacial cellularity and integration

To evaluate lateral cartilage integration of repair and native tissue, we analyzed histologically stained tissue slices to visualize integration and quantify cell number in the native tissue, integration zone, and repair (implant or defect). Here we demonstrate that the cartilage portion of the implant laterally integrates with native tissue but fails to promote cellularity into and throughout the implant. Masson Trichome staining of the repair regions (implant or defect) centered around the critical integration zone (Figure 2.5) illustrates that the integration region varies widely depending on the size of the surgical gap between implant and native tissue. With a small gap, no new tissue fills the integration zone, but the continuity of the surface greatly improves. With a larger space between implant and defect, highly cellular, fibrotic tissue nearly identical to the tissue in the defect repair fills the space. We quantify the cellularity in each region (i.e. native, integration zone, and repair) and confirm that cellular density in the integration regions is nearly identical to cell density in the empty defect repair (Figure 2.5). While the tissue in the integration regions is highly cellular and fibrotic in composition, the fibrotic repair tissue succeeds in laterally integrating the implant with the native cartilage. Previous research has shown that high cartilage specific cellularity in the integration regions is critical to create lasting integrative repair [45, 46], and to this end many researchers functionalize or coat the defect edges to promote cellularity [47, 48]. Unfortunately, despite the high levels of cells in the integration zones, the implants do not contain many cells (Figure 2.5), illustrating an inability for cells to migrate into the implants even with a high cell number in the surrounding tissue. Lack of cellularity in the implant is likely due to a myriad of factors, including high matrix density inhibiting cellular migration and that the cell type in integration regions is not cartilage specific.

2.4 Discussion

A significant hurdle for patients suffering from osteoarthritis is the lack of effective therapies which would decrease pain and improve function for several years prior to a joint replacement.

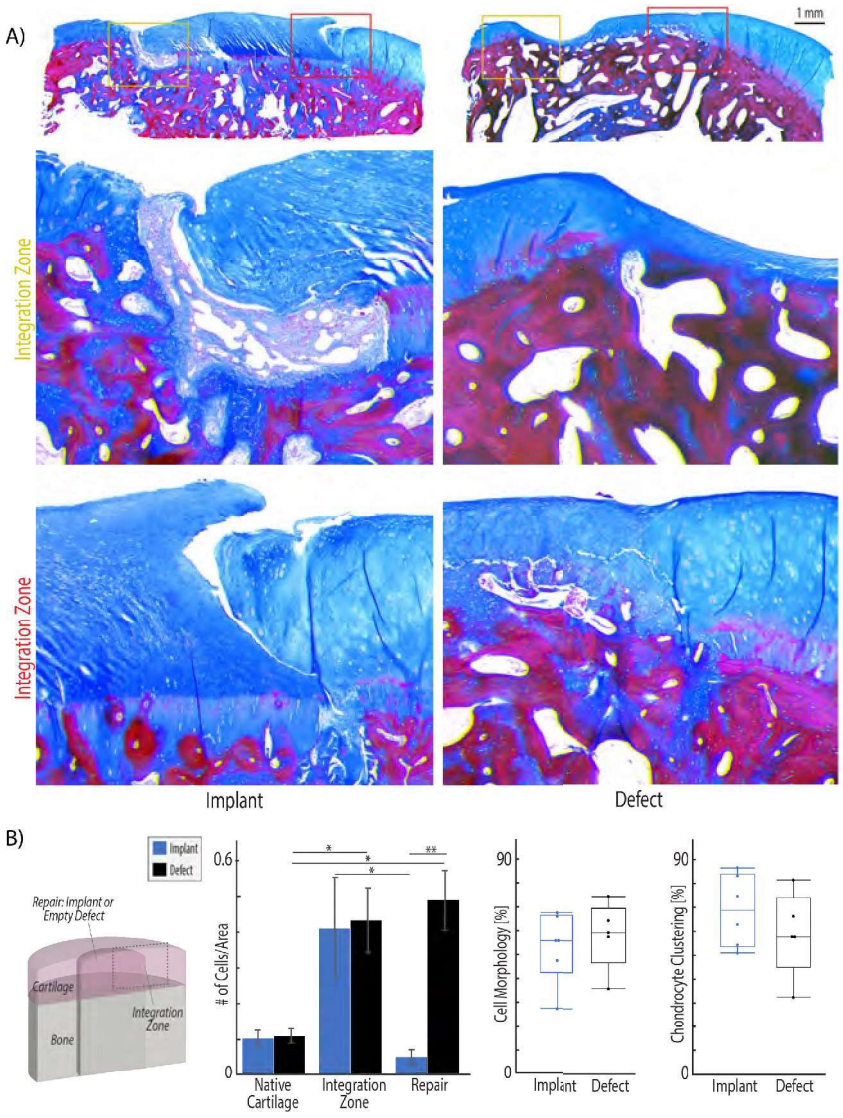

Figure 2.5: Acellular allografts promote high cellularity in the integration zone with native tissue. (A) After 6 months *in vivo*, Masson's trichome staining shows that integration regions of implants are either filled with tissue which is densely packed with cells and appears fibrotic (top image) or no new tissue forms when the gap between implant and native is small (bottom image). The integration region of defect repair tissue illustrates a transition from native cartilage with sparse, evenly distributed chondrocytes to a fibrotic tissue with visible collagen fibers and densely packed cells. (B) Masson's Trichrome images were analyzed using ImageJ thresholding and particle counting to quantify cell density in each region. The integration regions and defect repair tissue demonstrate significantly higher cellularity than native cartilage tissue. Additionally, while the integration regions are highly cellular, the cells do not migrate into the implant. Finally, ICRS II scoring was used to evaluate cell morphology. Unhealthy chondrocyte clustering is increased in the defect samples and can be observed near the integration zone in the histology examples in (A). Additional ICRS II tissue metrics are reported in supplementary figure A.3. (*$p < 0.05$, **$p < 0.001$, n=6 animals, statistics run with a two-way ANOVA test to determine cofactor significance, followed by a Tukey's honest significant difference test to determine p-values between implant types or tissue zones).

Existing clinical interventions either require multiple surgeries, rely on a limited source of donor tissue, or have not been shown to be effective. The state-of-the-art cartilage repair strategies largely do not succeed at promoting long-term tissue regeneration in critical sized defects. Microfracture, the most traditional repair strategy involves a procedure where the surgeon stimulates the bone marrow beneath a defect to fill the void with a blood clot. The advantages of microfracture include the ability to complete the straightforward procedure in one surgery, but microfracture fails to promote hyaline cartilage repair, repair defects larger than $1 - 2.5cm^2$ [49, 50], and largely shows poor healing even after just one year [51]. Autologous Chondrocyte Implantation (ACI) either with or without a matrix (MACI) involves extracting chondrocytes from a patient biopsy in an initial surgery, growing up the cells to amplify cell number, and implanting with a second surgery into the knee defect of the patient. While long term clinical success has been documented with ACI [52], ACI/MACI is severely limited by the need for two surgeries, the number of chondrocytes that can be extracted from the first surgery, the likely differentiation of chondrocytes during expansion, and morbidity of the donor site [50].

Two of the most successful clinical repair techniques are osteochondral autologous transplantation and osteochondral allograft transplantation. Autologous transplantation involves taking cartilage tissue from a non-load bearing region of a patient's knee and moving it to the defect region. While long term follow-up studies show success [53], this procedure is limited by the defect size that can be repaired, as tissue is sourced from a different part of the knee and can lead to donor site morbidity and associated complications. Osteochondral allografts, or transplant of osteochondral (bone and cartilage) tissue from healthy cartilage of a recently deceased donor, is the most successful therapy to date to delay a full knee replacement for patients with knee osteoarthritis, showing an 82% survival rate after 10 years [36]. While clinically successful, osteochondral allografts are extremely limited as they rely on donor tissue. In this work, we have analyzed a promising replacement clinical therapy, which utilizes the advantages of autografts and allografts, while eliminating the source limitations: an acellular allograft. Decellularized tissue has been shown to provide superior regenerative potential in many clinical settings outside of orthopedics [54, 55, 56], and involves

minimal manipulation to produce an acellular construct that matches a tissue's exact architecture. We show that an acellular osteochondral implant provides excellent regenerative and cartilage specific functional properties and has the additional distinct advantage that implants can be stored for a long time and be sourced from xenogenic (animal derived) tissue.

Long-term function of defect repair strategies in a relevant, non-human model is a critical aspect to any clinical intervention or engineered tissue construct prior to human clinical trials. Large animal models (sheep, goat, dog, and horse) are useful in analyzing the effectiveness of a treatment and closing the gap between *in vitro* experiments and human clinical studies [57, 58]. Sheep joints specifically demonstrate joint size, cartilage thickness, and limited intrinsic healing ability amenable to human joints [59]. As a result, many researchers utilize a sheep model [57] to show tibiofemoral defect treatment efficacy and limitations of microfracture with additional treatments [60, 61, 62], modified autologous plug transfer procedures [63, 64, 65, 66, 67], variations of allografts [38, 68, 69], and tissue engineered scaffolds [70, 71]. While all studies in load bearing regions of a sheep elucidate the potential clinical success of a technique or scaffold, many referenced above are only 1-3 months long, and thus do not indicate the long-term success or degradation. Additionally, while powerful tools, sheep models are limited to answering specific questions. Unlike humans and dogs, it is difficult to manage post-operative non-load bearing or therapy sessions in sheep. Therefore, sheep are best used to evaluate repairs for which post-operative management is minimal, and animals can bear weight immediately [59].

Several important recent findings posit that integration with native tissue is critical to the long-term success of any engineered articular cartilage implant. Furthermore, many researchers have shown that it is essential for an implant to promote cellularity in order to successfully integrate with native tissue [33, 72]. In articular cartilage, promoting cellularity is a distinct challenge as the dense extracellular matrix limits cell movement, the tissue is non-vascular, and even native tissue displays a low cell density compared to most tissues. While our work demonstrates acellular allografts as a promising strategy for cartilage defect repair, excellent integration with bone, and some lateral cartilage integration, we also show that even after 6 months *in vivo*, implants fails to

promote cellularity within the implant cartilage despite high levels of cellularity in the integration zone. We believe that targeted future work focusing on these limitations could advance the clinical effectiveness of acellular osteochondral implants. Coating the implants or surgical site prior to implantation with cartilage specific growth factors such as IGF 1 has been shown to stimulate cartilage specific cell migration to the border regions [73, 48]. While we observed high cellularity in the integration region of the defect repair (Figure 2.5), the cells were likely fibroblasts and failed to migrate into the acellular cartilage implant. Combining cartilage specific growth factor treatment with an acellular allograft would likely lead to improved clinical effectiveness. Furthermore, it is evident from the results presented here that surgical technique and careful implantation also affects the success of the implant. In animals where the implant was press-fit closely to the native tissue and the surface of the implant and native tissue were closely aligned, we observed superior surface continuity and functionality (Figure 2.2 and Figure 2.5). Prioritizing specific and precise implantation techniques would result in a decrease in the volume of the fibrotic integration region as well as superior surface continuity between the implant and native cartilage. Finally, recent work posits that while the dense cartilage extracellular matrix limits cell migration into an acellular allograft, breaking down the tissue into particles facilitates cell migration while maintaining cartilage specific structure and mechanics [74]. Future work investigating an implant where the cartilage portion of the osteochondral implant is pulverized could improve lateral integration, cellularity, and clinical effectiveness, especially if combined with precise surgical technique and a growth factor coating.

The work presented here shows that after 6 months in a sheep knee, implants match the structural composition of surrounding native cartilage, are able to provide bulk mechanical properties under compression, enable the critical capability of load transfer throughout the joint (see Luyao Cai Thesis), and restore surface roughness and friction. Importantly, here we show that acellular osteochondral implants are a viable and promising strategy to postpone a knee replacement in osteoarthritic joints by restoring function and decreasing pain for months to years. Additionally, the analysis suite used to evaluate repair from the whole joint (Luyao Cai Thesis) to the cellular level provides a model for evaluating new cartilage repair strategies. Using these analysis tools, we have

demonstrated the clinical effectiveness of a surgical intervention that requires only one surgery, does not rely on a limited tissue source, can immediately provide articular cartilage specific structure and function, and maintains cartilage specific function 6 months later in a relevant animal model. For the more than 50% percent of patients with osteoarthritis in their knee who are younger than 65 [14], acellular osteochondral implants provide a potential solution to decrease pain and increase function until the age where a total joint replacement is recommended.

2.5 Methods

2.5.1 Decellularization of Osteochondral Allograft Implants

Ovine osteochondral implants were harvested from the load bearing region of the distal femur of (donor) stifle joints using the Osteochondral Allograft Transfer System (6mm diameter; OATS, Arthrex, Naples, FL). Implants were decellularized in 2% Sodium Dodecyl Sulfate (SDS, Sigma Aldrich) at 37°C under constant agitation, washed in phosphate-buffered saline (PBS) and then incubated with 3.3 mg/ml DNase, 50 mg/ml RNase, 1% P/S, 1% fungizone at 37 °C under agitation for 24 hours. To deactivate the DNase after treatment, implants were bathed in 0.02% EDTA, with a final PBS wash. Acellular allografts were flash frozen in liquid nitrogen and lyophilized for 12 hours prior to surgical implantation.

2.5.2 Surgical Procedures for Defect Repair Using Decellularized Allografts

Cartilage defect repair using acellular allografts was performed on six ewes aged 2.25 $\pm$ 0.43 years, who all fell under a similar weight category (74.8 $\pm$ 8.4 kg). Using an end mill system, osteochondral defects were placed via drilled holes in the load bearing region of both medial condyles (6mm diameter and 10mm depth). An acellular allograft was press fit into the defect region on the right stifle joint, and the identical defect on the contralateral left joint was left empty as an untreated control. The joints were closed in layers, and the animal was allowed to move freely with no weight bearing limitations post-surgery. After six months, ewes were sacrificed, and stifle joints

were frozen at -80°C until subsequent analysis. Repair tissue was harvested by exposing the stifle joint space and removing tissue with a scalpel. Implants and surrounding native tissue (10 mm diameter, 10 mm depth) were extracted from each joint and bisected, with one half stored at -80°C and the other half fixed for 48 hours in 4% paraformaldehyde (PFA).

2.5.3 Structural Analysis Using Histology

Matrix deposition, glycosaminoglycan content, and overall repair structural continuity and quality were evaluated using histology. One half of the extracted tissue from each joint was fixed for 48 hours in 4% paraformaldehyde, decalcified for 3 weeks in EDTA, dehydrated progressively with EtOH, embedded in paraffin, sliced into 5 m sections using a microtome, and mounted on microscope slides. Sections were stained individually with Hematoxylin and Eosin (H&E) and Safranin-O/Fast Green (Histology Core, CU Denver Cancer Center). The International Cartilage Repair Society II (ICRS II) scoring paradigm was used to evaluate relative tissue quality in each repair (i.e. implant or defect) [75]. Scoring was performed by three independent and blinded observers.

2.5.4 Structural Analysis Using Raman Spectroscopy

The composition of tissue regions was quantitatively evaluated using Raman spectroscopy with a 785nm laser and spectra collected for wavenumbers 400-1600 cm^{-1}. Raman spectroscopy data was collected on an upright inVia microscope (Renishaw, Wotton-under-Edge, UK). The regions measured previously in atomic force microscopy were first identified using brightfield microscopy at 5× magnification, assisted by India ink markings on the edge of each analysis location. Samples were hydrated and a 63× immersion objective was focused with a 785 nm laser to illuminate a 1.064 µm diameter spot on the surface. In each region, spectral maps consisting of sixteen measurements covering a 40 µm x 40 µm area were collected. At each point in the spectral map, cosmic rays were removed from the collected spectra, a linear baseline was subtracted and intensity normalized, and spectra were smoothed [42]. The sixteen spectral acquisitions that composed each

spectral map were averaged, key peaks of interest were identified, and peak amplitude was calculated using custom R code following a previously established Raman spectra analysis approach [76]. Relative peak amplitudes for peaks of interest (amide III- 1280 cm^{-1}, v_2 phosphate- 441 cm^{-1}, chondroitin sulfate- 1068 cm^{-1}, and phenylalanine- 1003 cm^{-1} [39, 40, 41] were compared to calculate relative compositional differences in each region.

2.5.5 Characterization of Bulk Mechanical Properties via Indentation

To assess the ex vivo bulk mechanical properties of the native cartilage, integration zone, and tissue (i.e., implant or defect) repair, indentation was performed at nine points spanning 1.6 mm (200 m spacing between points) centered at the integration zone (Figure 2.3). In preparation for indentation a flat, thin section of tissue was sliced; the resulting test surface contained a cross-section of repair tissue, integration region, and native cartilage. Indentations (Hysitron TI 950 TriboIndenter, xZ-500 extended displacement stage) were performed on submerged samples using a 100 m radius spherical probe. For each indent, the probe was first lifted off the sample surface, then indented to a depth of 20 m at a rate of 240 m/s. the indent was held for 45 seconds to determine an equilibrium modulus, equal to compressive modulus E_c assuming a nonlinear poroelastic model [77]. A virtual contact point for each indent was determined following established methods [78]. Hertzian contact modulus and equilibrium modulus were calculated at each point. To calculate the reported regional bulk mechanical properties, the moduli at each of the four points measured within each region are averaged.

2.5.6 Surface Property Characterization by Atomic Force Microscopy

Articular cartilage surface roughness, frictional coefficient, adhesion, compressive modulus, and topographical structures were measured using atomic force microscopy (AFM, Keysight Technologies Inc., Santa Rosa, CA, USA). All measurements were taken on the articular surface of the implant in the three key regions of interest: native cartilage, integration zone, and tissue (i.e., implant or defect) repair. A cantilever with known geometry was used (2 µm borosilicate sphere,

NovaScan), and the cantilever stiffness was pre-calibrated to 0.36 N/m by the thermal fluctuation method [79]. Lateral calibration was determined using an improved wedge calibration method [80] and a TGF11 silicon calibration grating (Mikromasch). Each sample was affixed to a high grid-50 dish (Ibidi, USA) using a viscous cyanoacrylate and hydrated for all AFM testing. At each location, the macroscopic region of interest on the articular cartilage surface was approached and a brief scan (4×4) was performed to ensure the height change was in an acceptable range (7 µm). After locating a measurable 40x40 m area, sixteen independent locations of the scan area (4×4) were measured in force-volume mode, indented at 5 m/s with a setpoint force of approximately 12 nN. To estimate the compressive modulus, force-displacement approach curves were fit to the Hertzian linear elastic model for a defined round tip geometry [81]. Adhesion force was measured as the pull-off force upon tip separation from the surface during probe retraction. Both adhesion and compressive modulus were extracted from force-distance curves using PicoView 1.14 AFM analysis software. Immediately following and within the same scan area, a high resolution contact scan (1028×1028 px, or 40nm/px) was performed at 20 m/s with a constant applied normal force of 20 nN to generate detailed topography, raw deflection, and lateral voltage trace/retrace signals of surface features. Areas where the controller overloaded the sample or did not interact with the surface were excluded. Topographical images were analyzed to calculate root-mean-square (RMS) surface roughness using Gwyddion 2.56 SPM analysis software [82]. The averaged lateral voltage signal over each area was converted to friction force by multiplying by the lateral calibration constant and divided by the normal force to yield the coefficient of friction.

2.5.7 Quantitative Imaging of Osteochondral Bone Repair and Remodeling

Trabecular bone volume fraction, trabecular thickness, and trabecular spacing were measured using micro-computed tomography (Xradia Versa XRM-520, Zeiss, Dublin, CA, USA). The explants were scanned with a 0.4× objective, voxel size of 13.4 m3, energy settings of 50 kV, 3.0 W, 3 s exposure, 801 projections, and using the LE3 or LE 4 filters. Automated centering and beam hardening corrections were applied using Scout-and-Scan Control System Reconstructor software

(v 14.0.14829.38124). To analyze the bone structure, collected micro tomography images were imported into Dragonfly software (ORS v 4.1) and the Otsu algorithm [83] was implemented to separate ranges of the histogram corresponding to bone and background noise. Distinct volumes to analyze were designated in three key regions: native cartilage, integration zone, and tissue (i.e., implant or defect) repair. In each region, a sphere fitting-method in each trabeculae or the space between trabecula was used to calculate trabecular bone volume fraction, trabecular bone thickness, and trabecular bone spacing in Dragonfly software (ORS).

2.5.8 Cell Quantification using Histological Images

Cellularity of all regions of interest and cell migration into the repair tissue was quantified in each of the three key regions using paraffin embedded tissue slices (preparation detailed above) stained with Masson Trichrome (Newcomer Supply) following the manufacturer recommended staining protocol after tissue hydration with decreasing concentrations of EtOH. Each region (native, integration zone, and tissue repair) was isolated in a high resolution image and standard ImageJ thresholding [84] was used to identify cells (blue/black spots) and quantify cell number/tissue area using Image J particle counting.

2.5.9 Statistical Analysis

To test our hypotheses that treatment (osteochondral implant or empty defect) influenced articular cartilage architecture and repair (stiffness, surface roughness, adhesion, protein signature, bone composition) *in vivo*, mixed model analyses of variance (ANOVAs) were performed on generalized linear models with treatment, animal, and implant location (left stifle joint or right stifle joint) as the predictors, and the resulting measurement variable as the response. In all data sets, if treatment, animal, or implant location was found to be a significant predictor then the p-value significances between each group was calculated using Tukey's Honest Significant Difference Test. The same statistical approach was used for data collected in each region of interest. To compare between regions with the same treatment, the ANOVA was performed on a generalized linear model with

region, animal, and repair type as predictors. Statistical significance in all experiments was defined as $p < 0.05$. All statistical testing was performed using R software and the lmer package.

Chapter 3

Recellularization and Integration of Dense Extracellular Matrix by Percolation of Tissue Microparticles

3.1 Abstract

Cells embedded in the extracellular matrix of tissues play a critical role in maintaining homeostasis while promoting integration and regeneration following damage or disease. Emerging engineered biomaterials utilize decellularized extracellular matrix as a tissue-specific support structure; however, many dense, structured biomaterials unfortunately demonstrate limited formability, fail to promote cell migration, and result in limited tissue repair. Here, we developed a reinforced composite material of densely packed acellular extracellular matrix microparticles in a hydrogel, termed tissue clay, that can be molded and crosslinked to mimic native tissue architecture. We utilized hyaluronic acid-based hydrogels, amorphously packed with acellular articular cartilage tissue particulated to 125-250 microns in diameter and defined a percolation threshold of 0.57 (v/v) beyond which the compressive modulus exceeded 300kPa. Remarkably, primary chondrocytes recellularized particles within 48 hours, a process driven by chemotaxis, exhibited distributed cellularity in large engineered composites, and expressed genes consistent with native cartilage repair. We additionally demonstrated broad utility of tissue clays through recellularization and persistence of muscle, skin, and cartilage composites in a subcutaneous *in vivo* mouse model. Our findings suggest optimal strategies and material architectures to balance concurrent demands for large-scale mechanical properties while also supporting recellularization and integration of dense musculoskeletal and connective tissues.

3.2 Introduction

The extracellular matrix (ECM) is a dynamic environment that dictates and is regulated by activity of resident cells within tissue [56]. The ECM supports macroscale structure and protection for cells under physiological loading, while also providing microscale cellular contact for proliferation, differentiation, and receptor signaling [85]. Following injury to a tissue, the ECM signals resident cells to upregulate growth factor production and chemical signaling which promotes migration of inflammatory cells to the damaged site to begin a natural regenerative cascade of ECM repair [86]. The specific structure and composition of both healthy and engineered ECM determines its migratory and self-regenerative capabilities.

A critical paradox of regenerative materials, especially for dense tissues, is the need to provide tissue-specific mechanical and biochemical properties while enabling cell migration to promote normal tissue function and repair. From a structural and compositional standpoint, acellular ECM of native tissue is an ideal material for regeneration because it preserves the complex tissue architecture, molecular composition, and structural rigidity. However, the density of native ECM in musculoskeletal tissues can present a barrier to healing because cell migration arrests when the ECM pore size is less than approximately 10% of the nuclear area [87, 88] (Figure 3.1). Moreover, even in dense *in vitro* collagen gels, migration of mesenchymal lineage cells arrest once the collagen density reaches a critical threshold [89, 90] which is 30-40 times lower than the collagen density in adult connective tissues [88, 91]. Recent work confirms the finding that nuclear stiffness and size are key factors responsible for migration arrest, as mesenchymal cells that were treated to soften the nuclear architecture showed increased migration into dense hydrogels and devitalized connective tissue matrices [91]. These findings indicate that the regenerative potential in utilizing large implants of dense acellular matrices is limited in part by pore-size constraints [92]. In contrast, hydrogel-based approaches to tissue repair can provide higher porosity, as 1% HA/PEGDA gels maintain a 10-16 μm pore diameter [93], and modifiable biochemical contact sites but often fail to match the mechanical properties of dense connective tissues [56, 94]. The devitalization of a

decellularized tissue into small microparticle (i.e., morselized or powderized) fragments has been proposed as a hybrid method to increase the likelihood of cell migration into acellular tissue ECM [92]. Key to this observation is that cells are capable of limited migration into dense matrix [38], and the repacking of cellularized microparticles provides a means to attain a formable, high-density engineered material, comprised of individually cellularized microparticles. While initial studies using microparticulated tissue have shown some evidence of the chemotactic role that the ECM may play [95, 92], it is unknown whether microparticulated tissues could address the need for mechanical and biochemical properties while enabling cell migration.

In this work, we address the paradox of engineering materials of acellular ECM with high mechanical properties and cell migration by creating a tissue clay, defined as a reinforced composite material of densely packed acellular ECM microparticles in a hydrogel. Our objective was to develop a general approach for producing tissue clays, which have the benefit of forming and molding to mimic native tissue architecture, packing to high-density to mimic tissue mechanical properties, and enabling cellular migration and recellularization in large defects. Here, we specifically use articular cartilage tissue as a challenging model system: structural architecture is essential to the functionality of cartilage, evidenced by routine loading of multiple times body weight [96]. Additionally, the density of native cartilage ECM inhibits natural chondrocyte migration and repair of defects [97] (Figure 3.1). Due to the dense ECM structure and mechanical function, articular cartilage presents an extreme test case for our tissue repair method, which we use to test our hypothesis that a decellularized microparticulate ECM hydrogel can enable cellular migration while maintaining native mechanical properties.

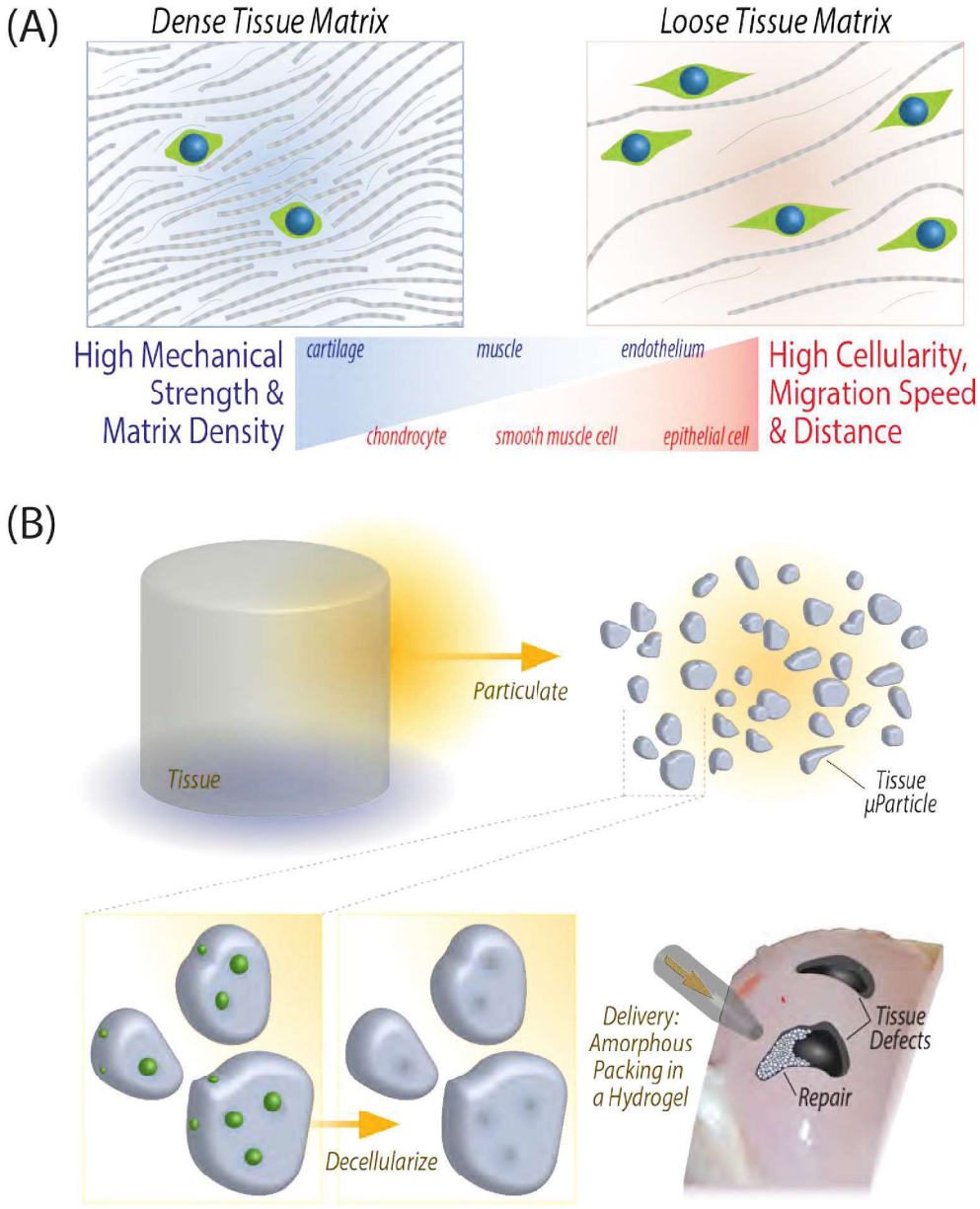

Figure 3.1: Design of an engineered extracellular matrix based scaffold, tissue clay, that maintains high mechanical strength while promoting cell migration and tissue repair.(A) Mechanically robust, dense musculoskeletal tissue withstands high mechanical loads, but the dense ECM also inhibits cell migrate through the tissue for repair after injury. Pore size constraints and nuclear size directly determine the rate of migration to an injury site. (B) Fabrication of tissue clay requires pulverization of articular cartilage, decellularization, and amorphous packing in a chondrogenic hydrogel to enable molding in a wide range of defect shapes or sizes.

3.3 Results

3.3.1 Tissue clay – a reinforced composite hydrogel of densely packed acellular ECM particles – exhibits structural and mechanical properties approaching that of native tissue.

We created tissue clay as a combination of a hydrogel material encapsulating acellular ECM particles. Hyaluronic acid (HA) was selected as a promising hydrogel material for cartilage regeneration [98] as it is biocompatible and has been shown as a scaffold material that can facilitate nutrient diffusion. Furthermore, hyaluronic acid is an important component of connective tissues and facilitates lubrication, cell differentiation, and cell growth [99]. When hyaluronic acid is functionalized with thiol groups and combined with polyethylene glycol diacrylate (PEGDA) monomers, the acrylate groups covalently link with thiols through Michael addition at physiological temperatures to create a stable, crosslinked, 3D hydrogel [93]. As a result, this hydrogel platform can fill a wide range of defect shapes and forms into a stable hydrogel once applied to the injury site. We hypothesized that HA-PEGDA hydrogels would serve as the ideal hydrogel base to encapsulate acellular tissue microparticles.

Tissue clay is a biomaterial tailored to mimic native articular cartilage in protein composition and in mechanical properties using the HA/PEGDA hydrogel in combination with acellular cartilage ECM microparticles. To fabricate cartilage tissue clay, we decellularized and pulverized native porcine articular cartilage into microparticles smaller than 250 µm in diameter, and then packed the microparticles within the hydrogel at various concentrations (Figure 3.2). The microparticle concentration in HA/PEGDA hydrogels first increased from a volume fraction of 0 to 0.5, leading to a 5-fold increase in the compressive modulus (10 kPa to 50 kPa). To achieve a compressive modulus similar to native tissue, we employed additional centrifugation during hydrogel polymerization, resulting in a packed hydrogel with a volume fraction of 0.6. The increase in density of amorphously packed microparticles from a volume fraction of 0.5 to 0.6 led to a non-linear additional 5-fold increase in the compressive modulus, rapidly reaching approximately 300 kPa (Figure 3.2).

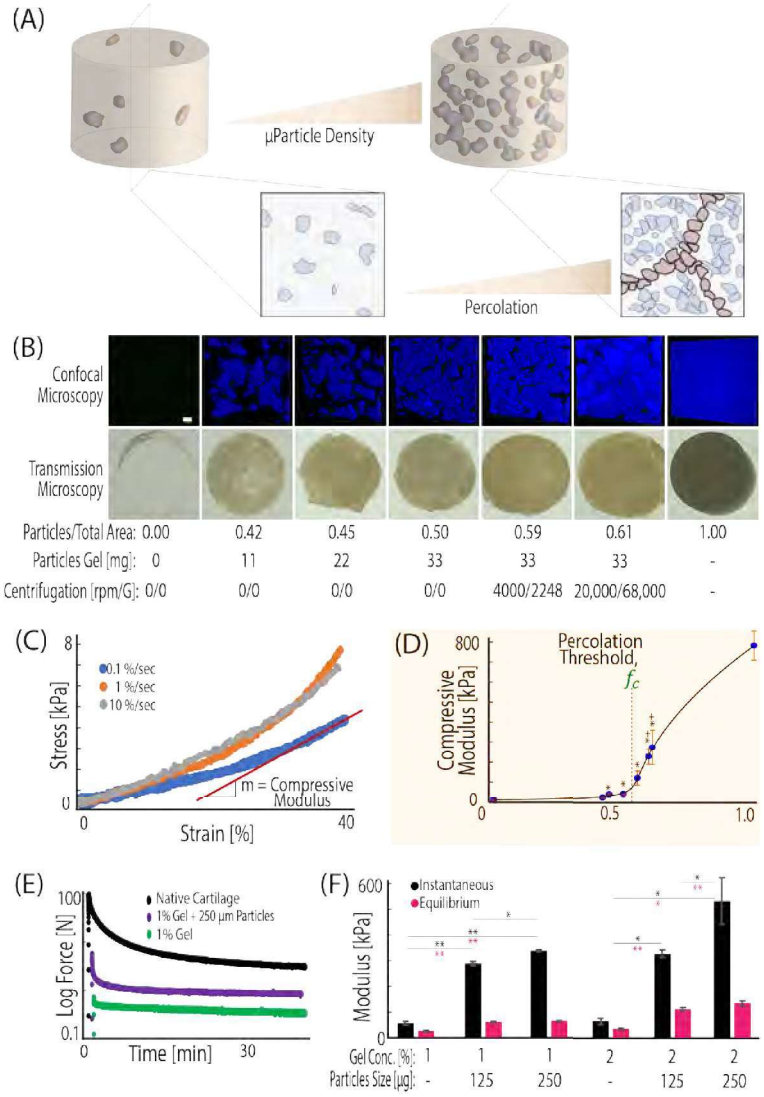

Figure 3.2: ECM microparticles amorphously packed in a hydrogel beyond a percolation threshold result in a composite material with mechanical properties that mimic native tissue. (A) Packing microparticles to high density in hydrogels increases cell-ECM contact and the volume ratio of microparticle to gel. As the volume ratio increases, the amount of void space between particles decreases until microparticles contact each other and form a new network. (B) The increase in microparticle volume ratio is visualized by taking 405 nm confocal microscopy z-stacks of DAPI stained tissue clay constructs. (C) Hydrogels were mechanically tested at 0.1%/sec to a deformation magnitude of 40%, and compressive modulus was calculated from the linear portion of the stress vs. strain curve. (D) The General Effective Medium (GEM) percolation model fit to the compressive modulus vs. density curve defines the percolation threshold at 0.57 volume ratio: the mathematical point where microparticles are predicted to interact and form a new network to propagate loading. (E, F) Tissue clay can be composed of a variety of hyaluronic acid concentrations and microparticle sizes, but for work presented here we utilized 1% HA hydrogels and 250 μm sized particles due to a balance of material consistency and strong mechanics. (*$p<0.05$, **$p<0.001$, $^{+}p<0.05$ as compared with hydrogel before centrifugation).

We hypothesized that the dramatic increase in compressive modulus between 0.5 and 0.6 volume fraction was attributed to packing the microparticles beyond a percolation threshold. Percolation is defined as the point at which the mechanics of the composite system becomes dictated by the network of interconnected stiff constituent pieces, rather than the soft surrounding hydrogel matrix [100] (Figure 3.2). To test our hypothesis, we employed percolation theory that applies across disciplines and explains common natural phenomena involving packing of multiphase materials [101]. Originally developed to model the mechanical behavior of identical objects suspended in a medium [102], percolation theory encounters a common difficulty in biological applications, due to the lack of shape uniformity among materials. A recent adaptation of previous models, the General Effective Medium theory (GEM), bridges percolation and homogenization theories to model continuum mechanics of random multiphase materials [100].

We applied the GEM percolation model to explain the mechanical basis for the large increase in compressive moduli between tissue clay with volume fractions of 0.5 and 0.6. The model considers the individual moduli of both the hydrogel and the cartilage and applies scaling factors to each component (Supplemental Figure A.1). As the concentration of microparticles in the hydrogel increases, the microparticles must pack more tightly together. The percolation model supported our hypothesis and demonstrated that increased amorphous packing of microparticles led to a new network of direct microparticle contact (Figure 3.2) and resulted in a tissue clay that approaches the compressive modulus of native cartilage. According to this model, the percolation threshold for cartilage tissue clay lies at a volume fraction of 0.57, and compression past this point led to rapid increases in compressive moduli (Figure 3.2).

3.3.2 Chondrocytes recellularize tissue particles and maintain a chondrogenic expression.

We next investigated the fate of chondrocytes when introduced to tissue clay with embedded cartilage ECM microparticles compressed beyond the percolation threshold. Surprisingly, when we introduced chondrocytes into the hydrogel portion of the composite, the cells migrated into and

recellularized the cartilage microparticles (Figure 3.3). Time-course imaging determined that cells migrate into the particles within the first two days *in vitro* (Figure 3.3), although in some cases we observed recellularization as early as 12 hours after cellular encapsulation in the hydrogel (Figure 3.3). Gene expression analysis of the embedded chondrocytes' RNA indicate that cells in tissue clay begin to upregulate key genes such as SOX9 (a pivotal transcription factor in chondrocytes critical for cell specification and differentiation), COL2A1 (the predominant collagen type in hyaline cartilage), and PRG4 (an important molecule involved in boundary lubrication), and significantly downregulate key fibrocartilaginous genes such as COL1A2, as compared to chondrocytes plated on tissue culture plastic (Figure 3.3). These data suggest not only that chondrocytes can migrate within the decellularized microparticles, but also that this method of artificial tissue production creates a favorable environment to facilitate a chondrogenic lineage and phenotype.

3.3.3 Chondrocyte migration into tissue particles is attributed to chemotaxis

Considering chondrocytes show limited migration *in vivo* in healthy tissue, and that dense cartilage ECM usually restricts cell mobility [103, 90] (Figure 3.1), the reorganization and migration of chondrocytes into the microparticles was unexpected. We hypothesized that chondrocyte migration into the void regions of acellular cartilage microparticles could be attributed to growth factor reservoirs preserved through decellularization. While sodium dodecyl sulfate (SDS) is typically considered a relatively harsh chemical detergent that could disrupt or wash away growth factors during decellularization [104, 105], we found no significant reduction of one primary growth factor, TGF-β1, in decellularized particles as compared to native tissue (Figure 3.4). Additionally, using a standard transwell migration assay, we investigated whether decellularized cartilage microparticles induce nearby cell migration with chondrocytes that are not encapsulated in our hydrogel system (Figure 3.4) and found the migration gradient of the microparticles is significantly stronger ($p<0.05$) than that of standard chondrocyte media (DMEM-F12 with 10% FBS) and non-supplemented DMEM (Figure 3.4). Growth factor reservoirs within acellular ECM microparticles influence the migratory behavior of primary chondrocytes, partially explaining the chondrocyte

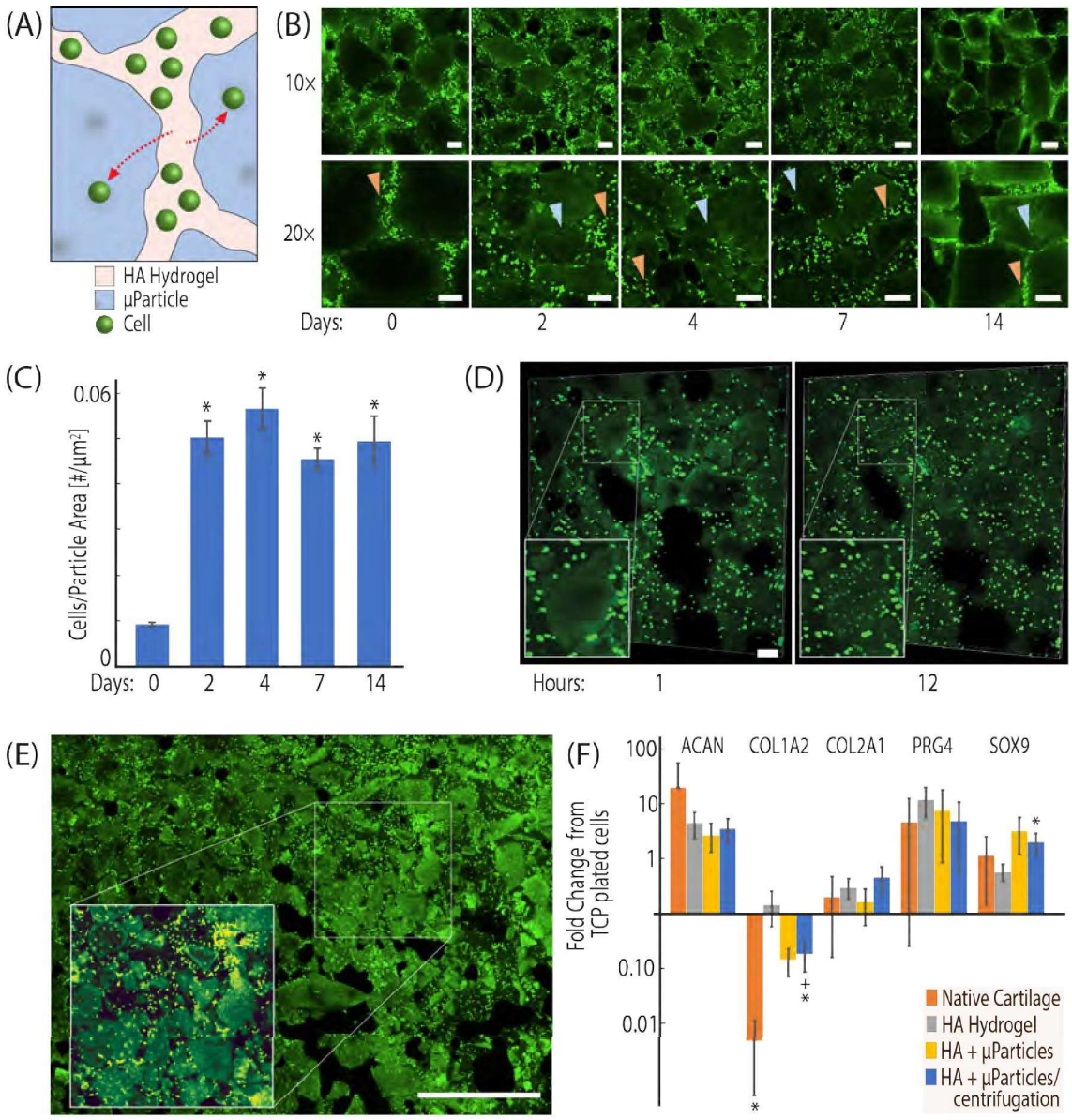

Figure 3.3: Chondrocytes introduced to the hydrogel region of the composite recellularize microparticles and maintain chondrogenic expression. (A, B) Chondrocytes are extracted from bovine knee joints, stained with a fluorescent proliferation dye (CFSE), and encapsulated in the hydrogel portion of tissue clay. The number of cells migrating into particles was measured by quantification of CFSE stained cells present within image-thresholded microparticles at 0,2,4,7, and 14 days post seeding. (C) Chondrocyte migration into the microparticles occurs within the first 2 days of culture. (D) Cells were observed migrating into the microparticles within the first 24 hours. (E) Image montaging supports that the migration was observed broadly throughout the tissue clay construct. (F) Quantitative RT-PCR of primary chondrocytes seeded in empty constructs, constructs at percolation, and constructs past percolation shows increased chondrogenic expression in tissue clay (HPRT1 used as housekeeping gene, fold change from TCP plated cells). Scale bar = 100 µm (B, D), 1 mm (E). (*$p<0.05$, RT-qPCR data compared to hydrogel control and $^{+}p<0.05$, compared to native tissue).

migration into microparticles that we observed within the first two days of culture.

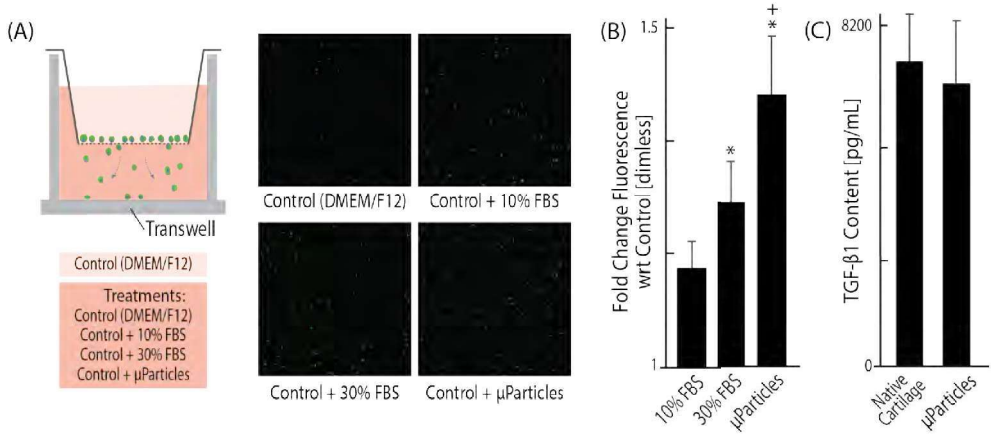

Figure 3.4: Growth factors are conserved in an acellular extracellular matrix and create a chemotactic gradient which promotes chondrocyte migration into tissue particles. (A, B) Using an established transwell migration assay with four different chemotactic gradients, typically non-migratory chondrocytes demonstrate a significantly greater attraction to the acellular ECM particles than to typical chondrocyte DMEM-F12 media, even with 10% FBS . (C) TGF-β is shown to be highly conserved in the microparticles, despite the processes of decellularization, which likely contributes to the chemotactic influence of the microparticles. ($p < 0.05$, *compared to DMEM, $^{+}$compared to 10% FBS).

Tissue clay overcomes the common imbalance of engineered materials that are optimized for either strong mechanics or cellularity as tissue clay retains mechanical properties of dense native tissue while also enabling cellular migration. Recently published research shows a few key factors [90] dictate cellular migration, including chemotactic signaling and material porosity. Migration in our system is likely affected by both factors in tandem, but the chemotactic effect of remaining growth factors plays a distinct role (Figure 3.4). Additionally, we know that the porosity of the HA/PEGDA hydrogel is dictated by the percentage of thiolated groups on the HA molecules, as well as by the ratio of thiol groups to diacrylate groups. We chose to use a 1% cross linked hydrogel, rather than a 2% hydrogel, to maintain larger pores (15 µm pore diameter) [93] for facilitating migration within the hydrogel domains of the tissue clay [106]. Furthermore, chondrocyte migration into tissue ECM has been previously observed at the edges of large acellular ECM implants, but only extending into the tissue about 25-100 µm from the edge [38, 107, 108]. Thus, pulverizing

the cartilage ECM until the microparticle diameter is <250 µm and embedding in a hydrogel with 15 µm pores facilitates chondrocyte migration towards matrix-bound TGF-β1. Finally, acellular particles contain some zones of 10-15 µm empty pores in regions of previously formed chondrons (Figure A.8). In follow up studies, tissue particles should be extensively characterized to confirm porosity changes that enable the cells to migrate towards a chemotactic signal in the matrix.

3.3.4 Tissue Clay is a broadly applicable platform design for regenerative hydrogels that promotes *in vivo* cellular infiltration without sacrificing mechanical properties

Toward broader applications, our tissue clay materials provide a universal and commercially available support material, and by testing different porcine tissue types and packing densities, we demonstrate that our hydrogels support cartilage, muscle, and skin regeneration and are viable in a subcutaneous mouse model (Figure 3.5). Furthermore, the tissue clay is mechanically tunable because the packing density of particles directly influences compressive modulus. We created hydrogels of three unique tissue types by encapsulating size-sorted, decellularized microparticles from the three distinct tissues into the HA/PEGDA hydrogel (Figure 3.5).

Given that our method involves decellularizing tissue to produce microparticles, we first used Raman spectroscopy, and compared our results to known native tissue protein signatures published in literature, to determine whether unique protein macrostructures were maintained through the process of decellularization in each respective tissue. In all tissue types, the spectra collected from tissue particles were distinct from the surrounding HA/PEGDA hydrogel. Additionally, key peaks and relative peak height ratios in our acellular tissue particles compare well with spectra reported previously in native cartilage, muscle, and skin [39, 41, 109], and the elevated signal intensity, particularly at higher wavenumbers, indicates that collagen and GAG structures native to each tissue type were retained within our decellularized tissue. These results further suggest that the chemistry and structures needed to maintain the biochemical and mechanical characteristics of each tissue persist despite decellularization.

We investigated the translational potential of the tissue clay platform via a subcutaneous mouse model. We implanted hydrogels composed of decellularized and microparticulated skin, muscle, or cartilage into male B6 mice (Figure 3.5). In the control HA/PEGDA hydrogel, the biomaterial induced a common adverse immune reaction of fibrotic encapsulation: formation of a fibrotic cell capsule directly surrounding the biomaterial to prevent further interplay between biomaterial and host [110]. By contrast, in the tissue clay implants, we observed extensive host cell infiltration into the introduced composite material, limited fibrotic encapsulation in articular cartilage hydrogels, and localization of the cells both around and inside of the tissue particles (Figure 3.5). Explants at three months exhibited increased cell infiltration into the tissue clay and increased levels of ECM deposition compared to explants at one month (Figure 3.5). The particles provide attachment sites, growth factors, and biochemical signals to promote production of extracellular matrix and host integration with the hydrogel. While further work is needed to classify whether cell integration *in vivo* was a macrophage response or a remodeling response, the hydrogels showed increased infiltration over the three months, a time scale longer than a typical initial immune response, suggesting cell homing and matrix deposition, rather than degradation (Figure 3.5). All mice survived until sacrifice, with no systemic adverse reactions or pain associated with the implants, confirming the safety of the tissue clay materials.

3.4 Discussion

A significant challenge for the design of biomaterials involves providing tissue-specific mechanical and biochemical properties while enabling cell migration to promote normal tissue function and repair. In this work, we meet the dual challenge of structure and cellularity by engineering a native tissue-based hydrogel with particulated ECM to facilitate cellular migration. The unique properties of tissue clay are achieved by packing acellular ECM microparticles past the percolation threshold, thereby increasing the compressive modulus and ensuring cell-microparticle interaction, while not inhibiting cellular mobility. We thus developed a material that makes cellular encapsulation simple and provides attachment sites to promote the tissue-specific signaling pathways

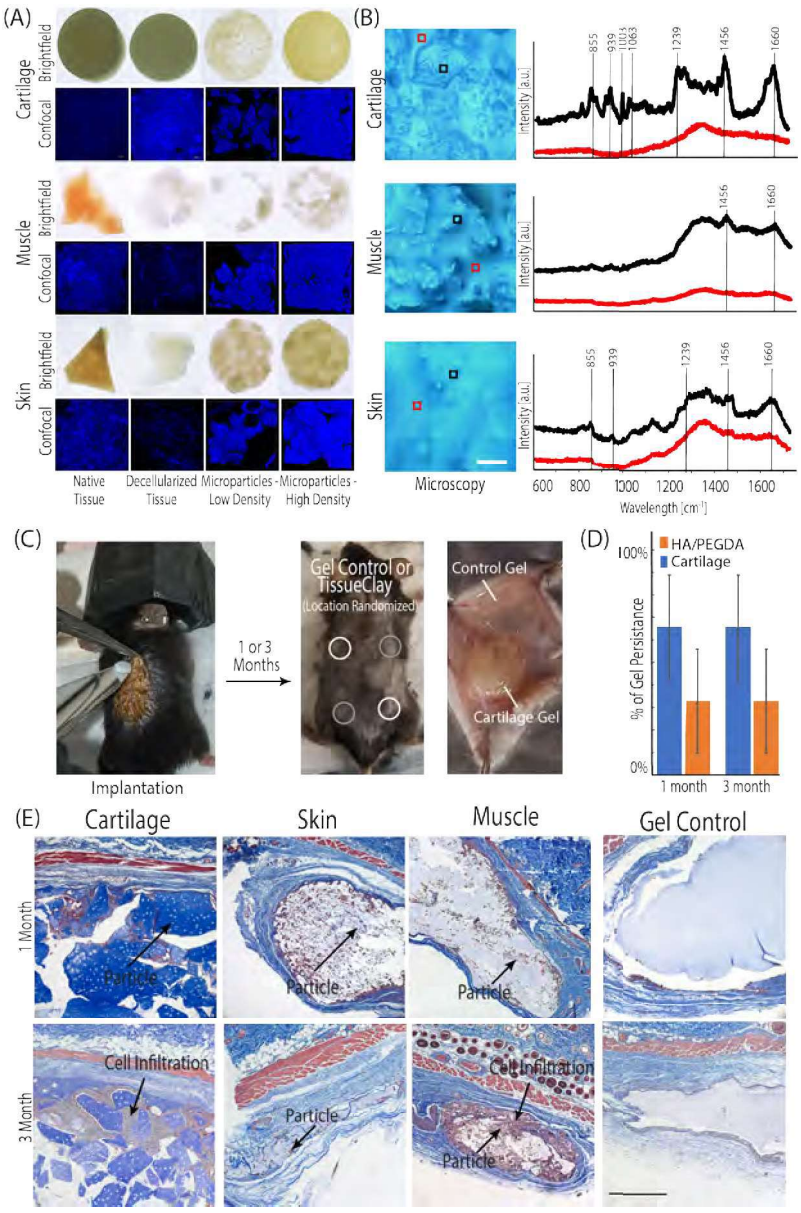

Figure 3.5: The tissue clay fabrication technique is versatile and mechanically tunable for a variety of tissues. (A, C) Tissue clay formed from acellular cartilage, skin, and muscle microparticles) were implanted subcutaneously into 8-week old male B6 mice. (B) Prior to implantation, the Raman spectra (representative spectra displayed in B) for all decellularized tissues (illustrated in black) and surrounding HA/PEGDA hydrogel (illustrated in red) confirmed unique structure signatures in each acellular tissue particle and displayed peaks typical of the respective native tissue, when compared to literature. Each spectra displayed in panel (B) is an average of 9 individual spectra collected in a 30 μm^2 grid. During the implantation procedure, each mouse received four hydrogels: two HA/PEGDA controls and two tissue clay implants. (D) After 1 or 3 months, constructs were explanted and analyzed for native cell infiltration and new ECM deposition. (E) Cell infiltration and new ECM deposition (dark purple nuclei, blue collagen) is observed between and inside of dECM particles towards the edges of the constructs, increasing towards the center of the implant by 3-months (E). Scale bars: B=100 µm, E=500 µm).

necessary for growth and regeneration. Cellular migration is especially restricted in dense articular cartilage tissue after injury because the pore size of the ECM (only a few nanometers) is far smaller than the nuclear diameters of chondrocytes and stem cells (5 µm) that could migrate from the bone marrow into the tissue after damage [111, 112]. Utilizing this extreme example, we demonstrate that chondrocytes introduced to tissue clay localized both around and within the microparticles and led to an upregulation of key chondrogenic markers by the encapsulated cells. In previous studies using osteochondral implants as a regenerative biomaterial, the tissue matrix was too dense for cells to migrate into the ECM [113, 114]. The work presented here shows that pulverizing ECM and reconstituting the particles in a chondrogenic hydrogel allows for cellular migration while maintaining mechanical properties of the osteochondral implant. These findings are encouraging for regeneration of articular cartilage in future functional *in vivo* studies with the tissue clay.

Acellular extracellular matrix as a regenerative material provides tissue specific cell receptors, growth factors, and protein compositions. Recently, several researchers have used digested particles from acellular tissues—e.g. from dermis, bladder, heart, and adipose—to form disassociated tissue-based liquid hydrogels. These hydrogels show significant cellular infiltration *in vivo*, but are structurally inadequate [115, 116]. While these studies support the notion that acellular matrix promotes cellularity, they do not explore the tradeoff with structural stability. Our simple technique of micronizing and decellularizing cartilage extracellular matrix, then recombining the tissue particles with a chondrogenic support matrix, can additionally be optimized for other tissues and applications by varying the packing density and tissue source of particles. Tissue clay utilizes the structure and composition of native extracellular matrices and thus mimics the mechanics of a native environment. At the same time, embedded tissue microparticles facilitate cell signaling, inducing native cells to generate their own tissue specific proteins and basement membrane.

We anticipate that our method will aid in overcoming a major difficulty of many previous tissue engineered solutions: that of integrating the implant with the native surrounding tissue [72]. *In vivo* subcutaneous mouse implants of all tissue constructs found that the material promotes cell

infiltration. In articular cartilage tissue clay, we additionally observed increased staining for collagen fibers between the microparticles suggesting that the material also promotes matrix production; a promising platform for cell communication and integration. The studies presented here are limited in showing tissue-specific functional behavior. We have shown that our platform provides tissue specific protein structure and tunability to improve mechanics, which together promote cell infiltration, cellular homing, and new ECM deposition. Our platform method enables future work to investigate the *in vivo* functional response in cartilage, skin, and muscle defect models.

3.5 Methods

3.5.1 Preparation of Tissue Microparticles

All tissue was sourced from market weight porcine animals within 48 hours of slaughter. Articular cartilage was harvested by exposing the knee joint space and removing tissue with a scalpel, taking care not to include calcified tissue [117]. Skin was obtained from the hairless stomach region, which we separated from underlying subcutaneous tissue and cut into small pieces prior to storage. Muscle was harvested directly from the thigh of the animal, using a scalpel to cut tissue into small portions. All tissues were frozen at -80°C until further processing. For microparticulation, tissues were pulverized using a liquid nitrogen magnetic freezer mill [95], and were sorted via a micro sieve stack to isolate cartilage microparticles <250 µm in diameter, and skin and muscle microparticles <750 µm in diameter (Electron Microscopy Sciences, Hatfield PA). Microparticles were decellularized in 2% SDS for 8 (cartilage), 30 (skin), or 24 (muscle) hours at 37°C, and in 0.1% DNase for 3 hours to remove cellular and genetic material [118]. Microparticles were rinsed in PBS for 2 hours under agitation, flash frozen in liquid nitrogen, and lyophilized.

3.5.2 Formation of Composite Hydrogels

Tissue microparticles were encapsulated in hyaluronic acid (HA) hydrogels at high density, facilitating amorphous packing. Lyophilized HA that had previously been thiolated to 25%,

which dissolved easily when introduced to sterile DPBS (Hyclone), and formed hydrogels using a Poly(ethylene) glycol diacrylate (PEGDA) cross linker (Alfa Aesar) with a ratio of 1:0.8 thiols to PEGDA. Two aqueous solutions (with a final ratio of HA 10 mg/ml and PEGDA 8.6 mg/ml) were combined and then either plated or mixed with microparticles (at varying ratios, maximum ratio was 220mg microparticles/mL HA/PEGDA hydrogel) prior to plating. Both solutions were plated in custom, standardized molds made from PDMS with glass slides on the top and bottom. The control HA/PEGDA hydrogel and microparticle composite hydrogels were incubated at 37°C for 30 min to facilitate Michael addition crosslinking of the diacrylate groups on the PEGDA with the thiol groups on the HA molecules to form a stable 3D structure. In some sample groups, to increase packing density, a PDMS mold was used with the HA/PEGDA plus microparticles solution and was placed in a centrifuge at 4000 rpm for 20 minutes during polymerization. This helped to compact and evenly distribute microparticles throughout the depth of the hydrogel, confirmed with confocal microscopy (Figure A.6).

3.5.3 Confocal Imaging and Calculation of Tissue Microparticle Density

Composite hydrogels were washed twice with PBS, followed by staining for 10 minutes with a standard DAPI stain at a concentration of 5µl stain/ 1 ml DPBS. Hydrogels were imaged on an inverted Nikon A1 confocal microscope with a standard 405 nm laser and 10× objective. Using ImageJ software, confocal images were thresholded [119] to identify microparticles within the image regions of interest. The thresholding mask was transformed into an outline, where the area within the microparticles was divided by the total image area to define microparticle density within the region of interest (Figure A.5). We imaged each composite hydrogel at 3 unique locations, and averaged the microparticle:hydrogel area fraction among the three locations.

3.5.4 Mechanical Testing and Calculation of Percolation Threshold

Mechanical properties of composite hydrogels were assessed using unconfined compression testing on a Bose ElectroForce 5500 system. We compressed the hydrogel to a strain of 40% of

the initial height (0.1% per second) to ensure quasi-static loading following initial (0.1 N pre-load) contact (Figure 3.2). The percolation threshold was determined using a General Effective Medium model [100], which includes the compressive modulus of both the tissue microparticle and hydrogel constituents, and a custom MATLAB power law analysis.

3.5.5 Cell Isolation

All primary cells were sourced from juvenile bovine knee joints within 12 hours of slaughter. Chondrocytes were harvested by exposing the knee joint space and removing articular cartilage (superficial and middle zones) with a scalpel [117]. To extract primary chondrocytes, cartilage was rinsed in sterile PBS, diced into $<1\ mm^2$ pieces, and digested with 0.2% collagenase-P (Roche Pharmaceuticals) added to serum-free and chemically-defined medium, specifically Dulbecco's Modified Eagle Medium: nutrient mixture F12 (DMEM-F12) supplemented with 0.1% bovine serum albumin, 100 units/mL penicillin, 100 ug/mL streptomycin, and 50 ug/mL ascorbate-2-phosphate.

3.5.6 Recellularization of Primary Chondrocytes into Microparticles

For all migration studies, freshly extracted chondrocytes were stained with carboxyfluorescein succinimidyl ester (CFSE) (Invitrogen) prior to hydrogel encapsulation. The chondrocyte cell pellet was resuspended in a 5µM CFSE solution, incubated for 20 minutes at 37°C, and quenched using serum-supplemented (10% FBS) defined medium for 5 minutes at 37°C. Fluorescently labeled chondrocytes were suspended in HA/PEGDA hydrogel solution ($1X10^6$ cells/ml), and then mixed with lyophilized microparticles to form cell-laden composite hydrogels, or directly formed without microparticles for control hydrogels). After crosslinking, hydrogels were suspended in chondrogenic medium (DMEM-F12 supplemented with 10% FBS, 0.1% bovine serum albumin, 100 units/mL penicillin, 100 ug/mL streptomycin, and 50 ug/mL ascorbate-2-phosphate) for 14 days, with media replacement every other day. Hydrogels with encapsulated chondrocytes were imaged using a 488 nm laser on an inverted Nikon confocal microscope to define chondrocyte movement throughout the 2-week culture period (on days 0, 2, 4, 7, and 14). Recellularization within the microparticles was

quantified using a custom thresholding and counting technique (Figure 3.3), and staining protocols were optimized and confirmed (Supplementary Figures A.3 and A.4). Each hydrogel was imaged at three independent locations, and the number of cells/particle area was averaged among the three locations.

3.5.7 Gene Expression of Chondrocyte-laden Hydrogels

To quantify gene expression of cell-laden composite hydrogels, freshly isolated chondrocytes were resuspended in HA/PEGDA solution at a cell density of $1X10^6$ cells/ml prior to hydrogel formation and culture, as described previously. After 14 days, tissue clay and control hydrogels were homogenized for 2 minutes (TissueRuptor) in QIAzol lysis Reagant (Qiagen) and chloroform was added to precipitate and remove proteins. RNA was isolated from cultured cells using the E.Z.N.A Total RNA kit (Omega Tek). Total extracted RNA was reverse transcribed into complimentary DNA (cDNA) (Bio-Rad) using a thermocycler. Quantitative Real-Time PCR (CFX96 Touch, Bio-Rad) was performed on the cDNA using Advanced SYBR Green Supermix and the CFX96 Touch thermocycler (Bio-Rad,). For all samples, HPRT1 was utilized as the housekeeping gene. Known genes for chondrocyte differentiation (SOX9, Col1A2, Col2A1, ACAN, and PRG4) were quantified in all groups: HA/PEGDA hydrogel, HA/PEGDA hydrogel with microparticles, HA/PEGDA hydrogel with microparticles and polymerized under centrifugation, and chondrocytes plated on tissue culture plastic. All measurements were normalized to the housekeeping gene, and fold changes were measured from gene expression of tissue culture plastic plated cells. All primers were designed to be specific for all known isotopes and separated by at least on intron or span an exon-exon junction, if splicing information was available.

3.5.8 Transwell Migration Assay

To quantify cell migration in response to chemical stimuli, CFSE stained cells were plated on the apical surface of Corning Fluoroblok 24-well plate inserts immediately following staining (40,000 cells in 200 µl of standard chondrocyte medium). In parallel, a known chemoattractant,

experimental sample, or controls were added to the basal chamber (600 µl): DMEM-F12 with 10% FBS (standard chondrocyte medium), DMEM-F12 with 30% FBS (enhanced serum medium), DMEM-F12 with 10mg/mL homogenized acellular ECM microparticles (experimental sample), or serum-free DMEM-F12 (negative control) (Figure 3.4). All Fluoroblok wells were incubated for 12 hours at 37°C, 5% CO2. After 12 hours, inserts were transferred to a new clear bottom plate where fluorescence was immediately measured using a bottom reading fluorescence plate reader (BioTek, Agilent) at 485/535 nm (Ex/Em). All results are presented as a fold change from the negative control (serum-free DMEM-F12). Supporting images were taken of the same Fluoroblok inserts on an inverted Nikon confocal microscope, 10× objective as previously described.

3.5.9 TGF-β Quantification to Evaluate Effect of Decellularization on Growth Factor Concentration

TGF-β levels were measured in microparticles before and after decellularization using the Quantkine ELISA kit (Bio-Techne, R&D Systems), following manufacturer instructions. Tissue particles were homogenized in serum-free DMEM F-12 and supernatant collected prior to testing.

3.5.10 Raman Spectroscopy to Evaluate Composite Hydrogel Structure

Raman Spectroscopy was performed using an upright InVia microscope (Reinshaw, Wotton-under-Edge, UK). Regions of interest on each sample were identified using brightfield microscopy at 5× magnification. Hydrogels were submerged in PBS to eliminate drying, and a 63× immersion objective was used in tandem with a 785 nm laser to excite a 1.064 µm diameter spot on the sample surface. The charge-coupled device (CCD) camera collected reflected spectra for wavelengths between 620 nm and 1711 nm. On each sample (acellular cartilage, acellular muscle, acellular skin, and HA-PEGDA hydrogel), three unique spectral maps were collected, each containing nine points covering 30 µm x 30 µm area. In each spectral map, cosmic rays were identified and removed, a linear baseline was subtracted and intensity normalized, and spectra were smoothed to remove noise

[42]. The nine spectral acquisitions that composed each spectral map were averaged and peaks were identified using an automated peak pick function in Reinshaw WiRE software. The Raman peaks identified in cartilage include C-C stretching (817 cm^{-1}), hydroxyproline (855 cm^{-1}), C-C collagen backbone (939 cm^{-1}), phenylalanine (1003 cm^{-1}), amide III (1239 cm^{-1}), CH2CH3 confirmation collagen assignment (1456 cm^{-1}), and amide I (1660 cm^{-1}), as well as GAG (1060 cm^{-1}). Muscle and skin exhibit several typical collagen peaks (855, 1003, 1456, and 1660 cm^{-1}) (Figure 3.5). We used these data to compare to known signatures expected in native cartilage, muscle, and skin tissue [39, 41, 109].

3.5.11 *In Vivo* Implantation and Evaluation via Subcutaneous Mouse Surgery

All animals used in this study were 8-week-old C57BL/6J male mice (000664) from Jackson Laboratories, and acclimated to surroundings for at least one week prior to the experiment. Protocols were performed in accordance with NIH guidelines for animal handling [120] and approved by the Institutional Animal Care and Use Committee by the University of Colorado at Boulder. Animals were housed in a temperature-controlled environment with 12-hour light cycles and received water and food ad libitum. Prior to implantation, endotoxin levels were measured in hydrogels using a gel clot endotoxin detection kit, following instructions from the manufacturer (Genscript). On the day of experiment, mice were anesthetized with isoflurane inhalant and the pedal response was used to test for sensation. Mice were then placed on a warming pad, ophthalmic ointment was applied to the corneas, and nails were trimmed. The surgical site on the mouse was shaved and cleaned with alcohol and betadine solution. Finally, a slow release analgesic (meloxicam) injection was delivered subcutaneously in the peritoneum. Two 8 mm incisions were made in each mouse, one between the shoulders and one between the hips. To the left and right of each incision, a 0.5 cm^2 pocket was formed to disrupt the fascia. One hydrogel (microparticle or control), 6 mm diameter and 2 mm thickness, was implanted per pocket, with randomization, and incisions were closed using wound clips. Wound clips were removed once the incision had healed completely. For the first 14 days post-surgery, mice were checked daily for health and signs of infection or pain (swelling,

redness of wound, weight loss, isolation, and/or loss of appetite). At 1- or 3-months post-surgery, the animals were euthanized (Figure A.7). Hydrogels and surrounding tissue were then explanted for analysis.

3.5.12 Histology of Explanted Hydrogels

Explants harvested from mice after euthanization were fixed in 4% PFA for 48 hours, dehydrated with a sequence of increasing concentration of ethanol (from 70% to 100%), embedded in paraffin, and sectioned using a microtome. Slices were mounted onto microscopy slides and stained with Masson's Trichome Kit (Newcomer Supply) to analyze structure, cell location, and new ECM deposition.

3.5.13 Statistics

To test our hypotheses that hydrogel treatment (microparticle density) is able to increase compressive modulus, chondrogenic gene expression, cellular migration, and hydrogel persistence *in vivo*, we performed a separate two-way analysis of variance (ANOVA) for each response variable with treatment and either animal, day, or implant location as fixed main effects. In the chemotaxis (Transwell migration) assay, we used a mixed-model ANOVA with fluorescence as the response variable, with treatment and time as fixed main effects, and animal as a random effect. Post-hoc analyses were performed Tukey's Honest Significant Difference Test with statistical significance defined as $p<0.05$. All statistical testing was performed using R software.

Chapter 4

Particulate ECM Bioink Crosslinks to Create Layered and Lubricated 3D-Printed Articular Cartilage Scaffolds

4.1 Abstract

Articular cartilage is a layered tissue with a complex heterogenous structure and lubricated surface which provides critical load bearing and lubrication in the knee joint and is challenging to reproduce with engineering. 3D printing techniques have enabled engineering of complex scaffolds for cartilage regeneration, but constructs fail to replicate the mechanics, unique layers, or lubrication and rely on toxic exogenous compounds to crosslink. To address the need for mechanically robust and layered scaffolds, we have developed an extracellular matrix (ECM) tissue particle based bioink which extrudes easily, polymerizes via disulfide bonding into a mechanically robust construct, and restores lubrication to the surface. Our cartilage ECM particle bioink, pECM bioink, utilizes thiol functionalized hyaluronan, a naturally occurring glycosaminoglycan, packed with 40-100 µm decellularized tissue particles. We experimentally determined that functionalized hyaluronan forms disulfide bonds with open sulfhydryl groups on the acellular tissue particles to create a solid 3D network. Here, we show that two unique inks can be extruded in series to 3D print a layered articular cartilage scaffold that has a compressive modulus of >50 kPa and restores critical cartilage surface lubrication; we achieve a frictional coefficient of 0.07, adhesion of 0.09 nN and surface roughness of 123 nm, similar to values measured on native cartilage. We demonstrate that our printing process enables the addition of 400 µm pores throughout the construct which increase the viability of introduced cells by 10% and improves cell distribution throughout the construct. We show that

delivery of these 3D printed scaffolds to a critical defect is straightforward, is customizable to any defect shape, and scaffold integration with the surrounding tissue is achieved after 7 days of culture. This study develops a novel method and material chemistry to create a layered cartilage scaffold that recapitulates both compressive modulus and critical lubrication properties of native cartilage.

4.2 Introduction

One of the most elusive tissues for the field of tissue engineering, articular cartilage is an essential load bearing tissue in the knee and demonstrates an inability to repair or regenerate following injury [11]. Despite the avascular and low cell density of articular cartilage, researchers have failed to design robust and integrative cartilage repair solutions. Healthy articular cartilage is composed of three heterogenous distinct tissue layers, each with a unique ratio of the two major extracellular membrane proteins, collagen and aggrecan, and different cell densities. The composition of each cartilage layer and the interplay between layers enables articular cartilage to provide excellent joint lubrication and facilitate load transmission during normal movement. Unfortunately, successfully replicating articular cartilage with a tissue engineered construct to repair defects following injury is an elusive challenge, despite many decades of innovation. In order to enable efficient and effective restoration of a chondral defect, there exists a significant need to engineer a cartilage replacement scaffold that mimics that tissue's structural properties as well as presenting natural biochemical cues for promoting cell growth and integration [29].

An ideal bio scaffold functions as a substrate for external cell attachment and proliferation, enables sufficient diffusion of nutrients and waste products through the scaffold, mimics native structural heterogeneities, and mechanically responds to normal loading on the specified tissue [121]. Therefore, a decellularized tissue extracellular matrix (ECM) is an ideal scaffold for tissue repair because it provides the same structural support of the native tissue as well as presenting familiar biological cues to enable cell invasion and integration from the surrounding tissue [56]. In practice, the application of an intact decellularized tissue for articular cartilage defect repair is limited by shape constraints and high native tissue density. Results from chapter 3 show that the

ECM from decellularized donor tissue can be broken down into small particles, and then fabricated into a composite material by densely packing particles in a hyaluronic acid/PEGDA hydrogel to create a regenerative model for cartilage repair [74, 92]. The dense packing of particles closely recapitulates mechanical properties of large decellularized tissue but also significantly improves cellular infiltration into the scaffold. While hydrogels packed with cartilage ECM are a promising advancement in scaffold technology, it is critical to produce a scaffold that also mimics the distinct layered structure of articular cartilage.

Advanced manufacturing techniques, such as 3D printing, provide several advantages for tissue engineering and bio scaffold fabrication. A wide variety of applications utilize extrusion-based printing, leveraging the tunability of the extrusion size and printable materials, the capacity to create constructs with unique layers, and the ability to print custom shapes and sizes. Articular cartilage constructs must recapitulate three key regions of tissue: the bottom third of the construct (deep zone) needs to anchor the scaffold to the underlying subchondral bone, the middle zone needs to absorb and distribute compressive loads on the tissue, and the surface (superficial zone) is essential for lubricating the surface under shear motion and therefore requires a smooth surface with a low coefficient of friction [122, 123, 96]. Multiple recent studies have involved extrusion based printing of conventional synthetic polymers to create articular cartilage scaffolds, as these polymers provide enhanced engineering control [124, 125]. Unfortunately, synthetic polymers generally fail to fully mimic the structure or function of most natural tissues, including articular cartilage. Alternatively, natural polymers, often composed of proteins occurring in abundance in articular cartilage such as hyaluronan, alginate, and collagen, are also used for articular cartilage 3D printing applications [126, 127, 128]. Unfortunately, most natural polymer-based hydrogels rely on crosslinking with relatively toxic photo initiators and UV light to enable the production of a stable scaffold and do not recapitulate the complex interplay between the proteins and polysaccharides found in most native tissue. To increase the polymer complexity of natural hydrogels, researchers developed extracellular matrix-based bioinks by digesting decellularized tissue into liquid (monomeric) form [129]. In these procedures, proteases digest the tissue and break down the rigid ECM structure,

which liquifies the tissue. Unfortunately, the tissue digestion is so complete it destroys the protein organization that provides the tissue with its unique structure, ECM architecture, protein interactions, and cellular attachment sites: essential components to creating an ideal regenerative tissue environment.

Here, we develop a fabrication approach and new 3D printable bioink (pECM bioink)to create mechanically robust cartilage, with distinct structural and lubrication layers, sourced from only tissue-based and natural extracellular matrix components. The method developed here leverages the sulfhydryl groups on cysteines of decellularized articular cartilage to crosslink with thiol-functionalized hyaluronic acid, creating stable disulfide bonds between the two bioink components. Unlike the bioinks formed from complete tissue digestion, acellular microparticles are produced via mechanical pulverization, producing ECM microparticles that preserve the micro mechanical and biological properties of the original tissue. The pulverized particles can be densely packed in a hydrogel solution and printed via extrusion. Using viscous clay printing techniques as motivation, we set out to print ECM particle bioink. We demonstrate that printing with ECM particle bioink enabled the fabrication of layered tissue and the ability to print macro pores in the scaffold. Additionally, we illustrate the simplicity in printing and implanting custom scaffolds into an articular cartilage defect. The two-component 3D printable bioink developed here provides both the structural complexity and diverse molecular composition necessary for cartilage, while also replicating the critical mechanical environment and layered structural architecture found in native cartilage.

4.3 Results

4.3.1 ECM particle bioink utilizes only natural extracellular matrix components and polymerizes under physiological conditions

We set out to engineer an articular cartilage bioink that would be printable, could polymerize without the use of harsh exogenous chemicals, and would allow the reproduction of native mechanical, structural, and biophysical properties. We thiolated hyaluronan (HA) to functionalize

the HA monomer and found that the resulting two-part bioink when combined with microparticles polymerized in less than an hour without the use of any chemical or light treatments (Figure 4.1). We then investigated the chemical interactions leading to the polymerization of the bioink and found that the thiol (-SH) groups on the cysteines within the ECM of acellular cartilage tissue particles form disulfide bonds with the thiol groups on functionalized HA at a pH of 7. We quantified the number of open thiol groups on our manufactured ECM particles using an Ellman's assay calibrated with a cysteine standard curve (Figure 4.1). The ECM microparticles were found to contain 0.003 mM/mg of open thiol groups that could potentially react directly with the thiolated HA in our bioink formulation (Figure 4.1). We repeated the Ellman's assay on 20% thiolated HA, the second component in our bioink, and found that the HA had a sulfhydryl concentration of 0.01 mM/mg. While the thiolated HA has a larger sulfhydryl concentration than the microparticles, the HA fragments are very small compared to the particles, and thus more easily interact with particles to crosslink, rather than crosslinking to themselves. Since free sufhydryl groups are known to react to form disulfide bonds at a neutral pH, we hypothesize that our bioink largely polymerizes due to free sulfhydryl groups on the microparticles reacting with sulfhydryl groups on the HA.

A previous formulation of our bioink utilized the synthetic polymer polyethylene glycol diacrylate (PEGDA) to produce HA based hydrogels [74, 106]. In this formulation, the diacrylate groups present in PEGDA crosslink with the open thiols on the functionalized hyaluronan via the well-defined Michael Addition reaction [106]. To evaluate the crosslinking rate and test the role of disulfide bond formation in the HA-particle scaffolds, we measured the compressive modulus during polymerization (at 30 minutes and 2 hours) of several scaffold formulations: thiol functionalized HA, thiol functionalized HA with PEGDA, and both groups with the addition of acellular cartilage microparticles (Figure 4.1). We know from observation in preliminary studies that HA/PEGDA polymerization occurs within 30 minutes while thiolated HA alone can take up to 12 hours; these metrics served as our baselines for comparison. At the two-hour timepoint, bioink composed of thiol functionalized HA alone had not polymerized. However, mixing the thiolated HA with either ECM microparticles, PEGDA, or both, led to varying degrees of polymerization by just 30 min, with the

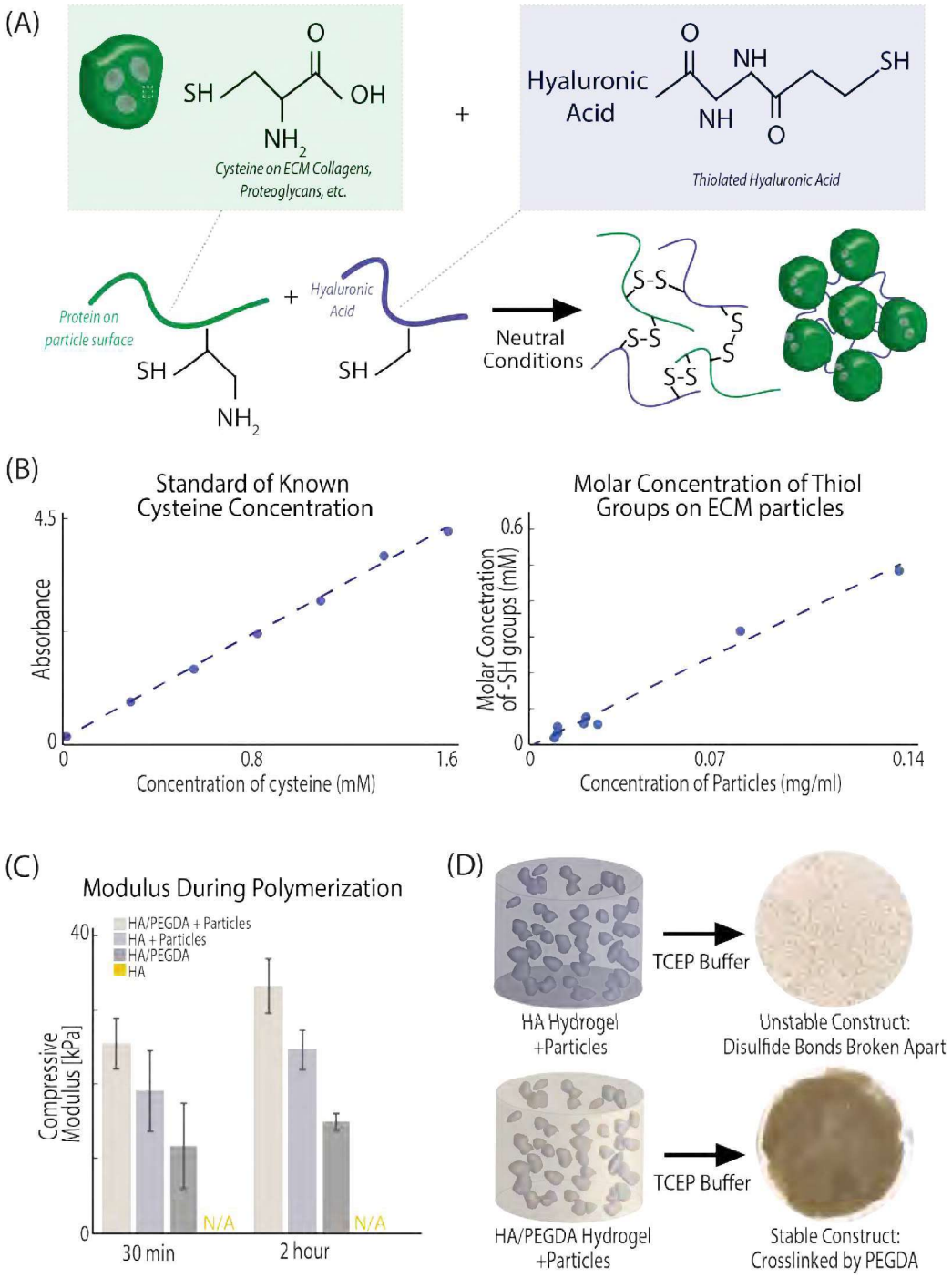

Figure 4.1: Design of native tissue bioinks that crosslink ECM particles to hyaluronan via disulfide bonding. (A) Scaffolds crosslink by disulfide bond formation between thiolated hyaluronic acid polymers and open sulfahydryl groups on the tissue particles to form a stable 3D network. (B) By comparing to known quantities of cysteine, we measure that particles contain 0.003 mM/mg of sulfhydryl groups to interact with thiolated hyaluronan. (C) The addition of either particles, PEGDA, or both lead to initial cross linking and polymerization by 30 minutes, with further polymerization by 2 hours. In control thiolated hyaluronan only constructs, constructs are still liquid at 2 hours. (D) TCEP buffer is a reducing agent which breaks apart disulfide bonds. Incubation in TCEP buffer confirms that HA + Particle gels crosslink via disulfide bonding.

modulus increasing in all groups by 2 hours (Figure 4.1). These findings indicated that the microparticles do support polymerization of the bioink, and thiolated HA alone crosslinks much more slowly. To test whether disulfide bonding specifically is responsible for the stabilization interactions between thiolated HA and acellular tissue particles, we treated each type of fully polymerized particle construct with tris(2-carboxyethyl)phosphine (TCEP), a reducing agent known to break disulfide bonds. After 24 hours under constant agitation, the HA-particle constructs had completely dissociated (broken apart), while the HA/PEGDA constructs maintained their structure (Figure 4.1). The dissociation of HA-particle scaffolds in the presence of TCEP confirmed that disulfide bonding is the major crosslinking mechanism taking place in HA-ECM particle bioink scaffolds.

4.3.2 Printing layered tissue structures

Recent work in our lab established new methods to form ECM particle-based scaffolds *in vitro*, creating a composite of decellularized microparticles in a hydrogel resin (Figure 4.2). These methods produce the scaffold presented in chapter 3 which replicates comparable mechanical properties to native cartilage tissue when particle packing exceeds the percolation threshold: the point at which the connectivity of networks of interacting particles dissipates the mechanical force. We set out to adapt this ECM particle-based scaffold method to produce an ideal bioink which could be easily extruded and printed at or near the percolation threshold. Transitioning this microparticulate ECM technology to a printable ink has numerous advantages including enabling layered printing and facilitating complex/custom shapes that would be difficult to mold on-demand. Here, we developed a cartilage tissue ECM particle bioink that can extrude consistently out of a 22-gauge nozzle to create layered constructs designed to fit custom needs (i.e. any shape, height, infill density that is designed can be printed). The resulting material that we printed with is highly viscous, holding its shape like traditional ceramic clays. The viscosity of the ECM particle bioink allows the construct to hold its shape as each layer is printed, and to fully polymerize at 37°C after printing.

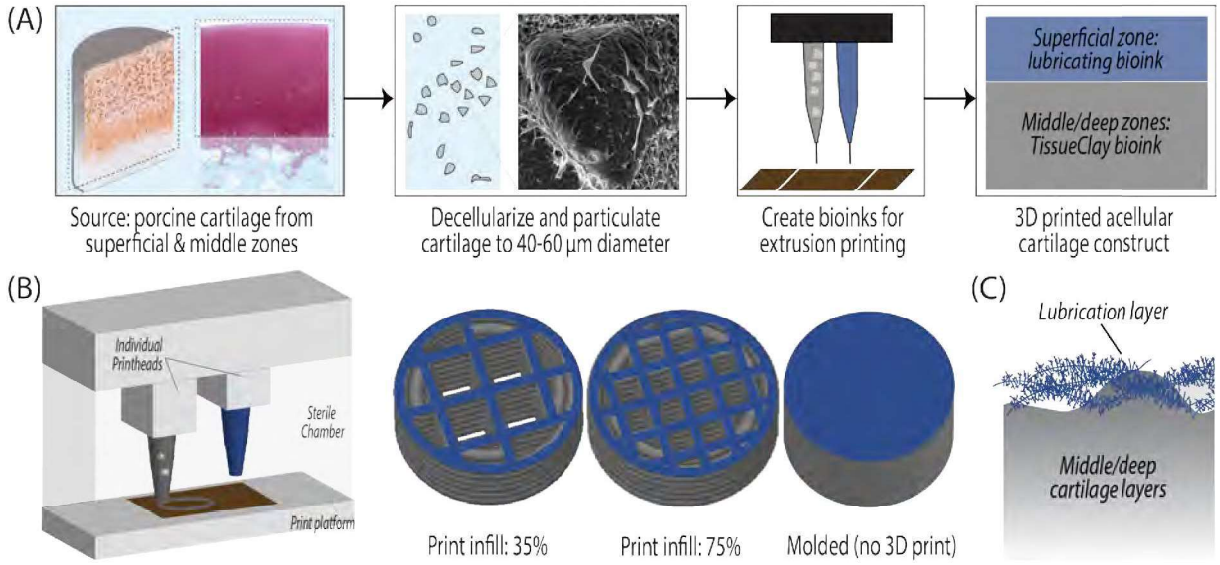

Figure 4.2: Development of a tissue ECM particle bioink (pECM) enables layered printing to create cartilage mimics with mechanically-robust structure and lubrication. (A) Cartilage tissue is decellularized and particulated to 40-100 µm, the particles are encapsulated in hyaluronan and printed to create a mechanically robust cartilage scaffold. A top lubrication layer composed of only hyaluronan is printed via a second nozzle to replicate lubrication surface characteristics of cartilage. (B) Scaffolds are printed at two different densities with a 22-gauge printhead tip to evaluate the role of differentially sized macropores on nutrient diffusion, cell viability, and mechanics. As a comparison, a third experimental group is made by molding the scaffold, rather than printing. (C) The lubrication layer printed as the superficial layer of the cartilage tissue construct is made up of crosslinked hyaluronan, a polysaccharide which plays a key role in lubrication of native articular cartilage.

4.3.3 Cartilage ECM bioink scaffolds printed with small pores retain comparable mechanical properties to solid bioink constructs

Compressive properties are critical for an engineered cartilage tissue scaffolds, as articular cartilage experiences over 1.5 times the body's weight just during walking [130]. Also critical to engineered cartilage scaffolds, nutrient transport and cell migration both depend on porosity of tissues and scaffolds, with larger pores generally facilitating greater movement. We printed our ECM particle bioink with two different infill densities to modulate the macro pore size in the construct and compared the printed designs to a construct with no pores manufactured via traditional gel molding rather than printing (Figure 4.2). We found that printing the ECM particle bioink with a high infill density (75%), but the addition of 400 µm pores, maintained the same compressive modulus as the molded gel, at 45 kPa (Figure 4.3) – just below the percolation threshold defined in chapter 3. However, increasing the pore size to print a macro porous gridded structure using a 35% infill design decreased the compressive modulus significantly to 26 kPa (Figure 4.3). While native cartilage tissue displays a compressive modulus during loading of closer to 500 kPa- 1 MPa [131, 132], we know that when particles are compressed past a percolation point, the modulus quickly increases to nearly 300 kPa (chapter 3). Therefore, under high levels of compression, the 3D printed scaffolds do not maintain a homogenous modulus of 45 kPa. Additionally, with small amounts of tissue growth between the acellular tissue particles, the modulus of the scaffold will likely increase rapidly.

4.3.4 The printing of a hyaluronic acid superficial layer provided a smooth, low-friction superficial lubrication layer

The surface of native articular cartilage is critical for lubrication [44, 46, 133], which in the knee facilitates movement of the femoral cartilage across the tibial cartilage and menisci under loading. In native articular cartilage, the uppermost superficial layer is largely responsible for creating and maintaining this lubrication. HA is an essential component in both synovial fluid

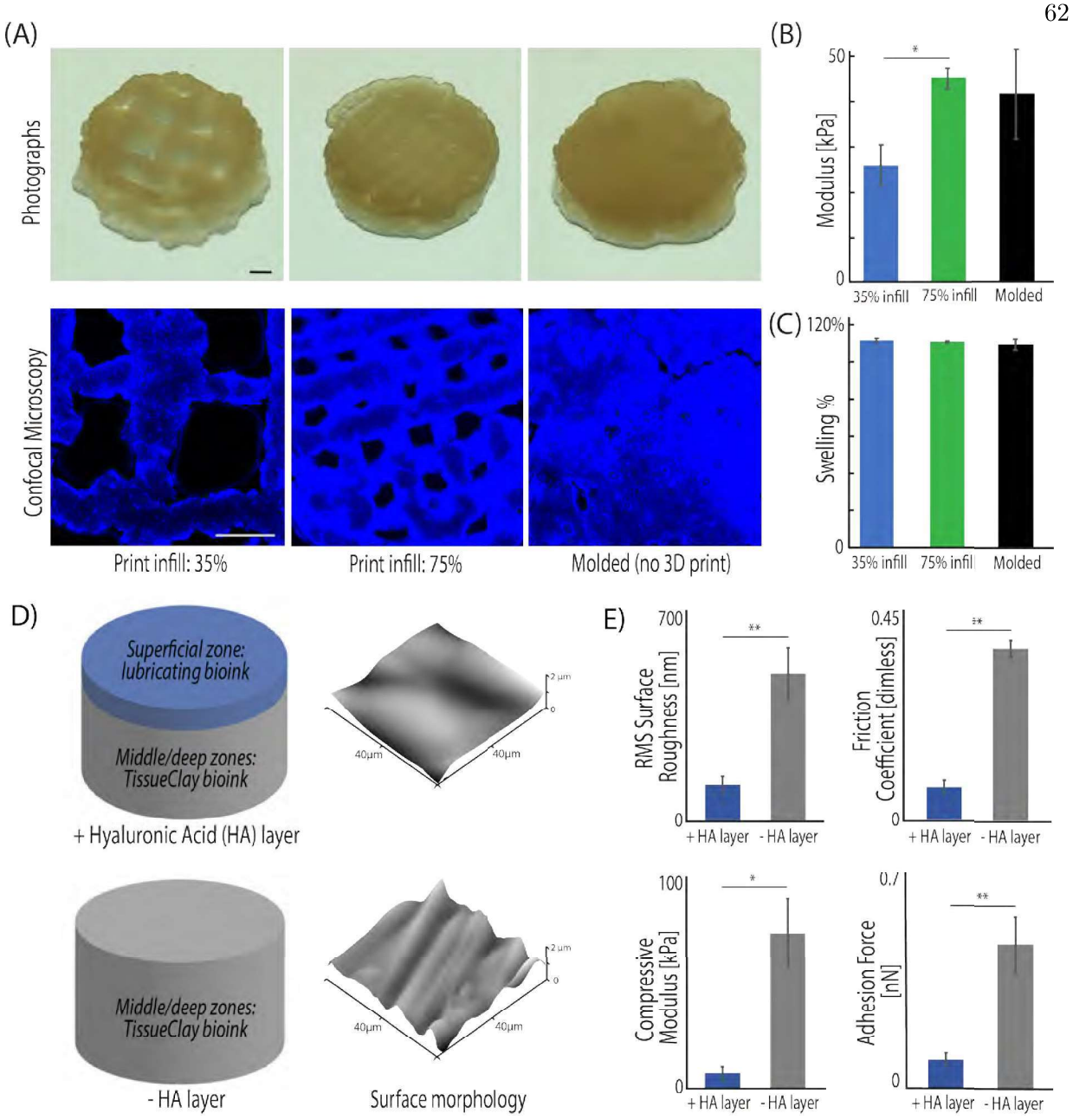

Figure 4.3: pECM bioink prints via extrusion to create mechanically robust middle and deep zones with a smooth and low friction superficial zone. (A) Incorporating microtissue particles into a hyaluronan ink enables printing of a wide variety of structures. Here, we create scaffolds with a range of macropores: 1 mm, 400 μm, no pores. (B) The addition of small macropores had no effect on the overall compressive modulus of the scaffold, measured under unconfined compression with a 10mm flat platen. (C) The incorporation of pores did not change the swelling levels of the constructs, confirming that the swelling depends heavily on the chemical crosslinking of the ink rather than the shape of the construct. (D) Printing a superficial zone of HA decreased the surface roughness, friction, and adhesion significantly (surface measured on the AFM with a 2μm spherical probe). * denotes $p<0.05$, ** denotes $p<0.001$, two-way ANOVA followed by Tukey's honest significant difference test. Scale bar is 1mm.

and articular cartilage and plays a key role in surface lubrication [134, 135, 136]. In this work, we printed a surface layer composed only of thiol functionalized HA to serve as a smooth lubricating layer on top of the ECM particle bioink construct (Figure 4.2). Using atomic force microscopy (AFM), we compared the surface of the construct made with only an ECM particle bioink layer to the surface of the constructs printed with an added HA superficial layer (Figure 4.3). The addition of a superficial layer on the surface of the 3D printed constructs significantly decreased surface roughness, friction, and adhesion. The surface roughness decreased by 400nm, the frictional coefficient decreased by 0.3 (from 0.37 to 0.07) and the adhesion on the surface decreased by 0.4 nN (Figure 4.3). Importantly, we restore native tribological properties as the coefficient of friction in previous AFM experiments of native bovine tissue are measured as 0.1 nN [137] and 0.2 nN [44]. The addition of the HA reduced the surface roughness to 250 nm which mimics the roughness of native articular cartilage (measured previously as 250-300 nm [44]). With these data, we show that adding a thin HA layer on the surface of the 3D printed construct creates a superficial zone lubrication layer, as it significantly reduced key parameters such as friction, roughness, and adhesion and achieves values measured in native tissue.

4.3.5 Pores enable cell and nutrient distribution throughout the scaffold, leading to improved cell viability in printed constructs over molded scaffolds

We investigated the cell viability in the scaffolds with ranging porosity (35% infill, 75% infill, molded) using primary chondrocytes, sourced directly from juvenile bovine cartilage. We polymerized all constructs for 1 hour and hydrated in standard chondrocyte media for 4 hours prior to cell seeding (Figure 4.4). When we seeded 10 million cells on the surface of each construct, we found that after seven days the cell viability and cell distribution from the topmost layers to the bottom layers of the construct were increased with increasing pore size. After 7 days in culture, we measured a statistically significant increase in cell death with decreasing pore size: 20% cell death in 35% infill constructs, 30% cell death in the 75% infill constructs, and 40% cell death in the molded gels with no printed pores (Figure 4.4). In a static culture setup, distributing nutrients effectively

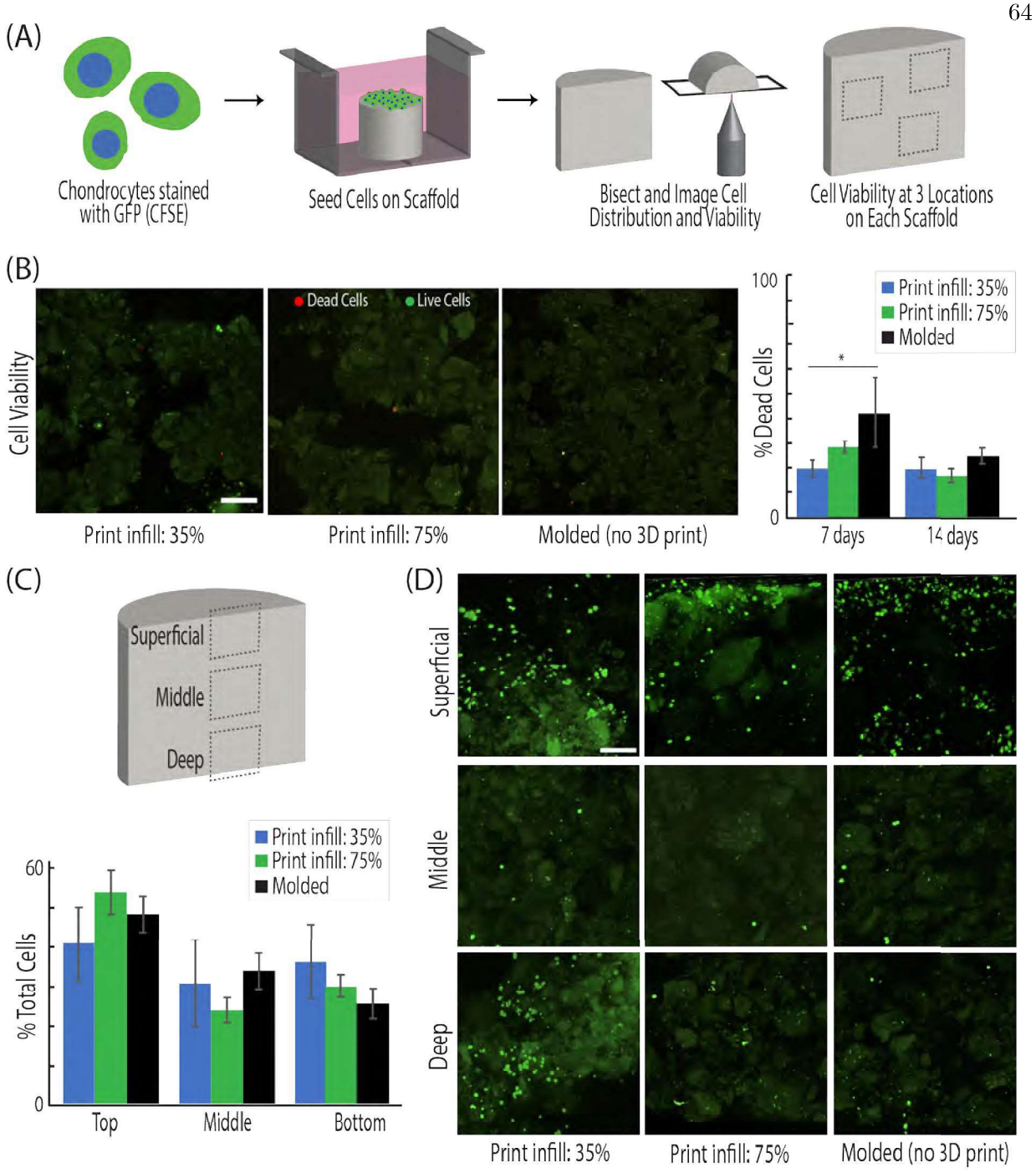

Figure 4.4: Increasing porosity in constructs led to improved cell distribution and viability. (A, B) Chondrocytes are extracted from bovine knee joints, stained with a fluorescent proliferation dye (CFSE), and seeded on top of all constructs. The percentage of dead cells was measured by quantification of CFSE (live) or ethidium homodimer (dead) stained cells present 7- and 14-days post seeding. (C, D) Chondrocyte distribution throughout the scaffold was measured by quantification of CFSE stained cells at three tissue depths: superficial, middle, and deep after 7 days of culture. (* denotes $p<0.05$, two-way ANOVA followed by Tukey's honest significant difference test).

throughout the center of scaffolds is typically challenging, and lack of nutrient distribution leads to increased cell death [138, 139]. By printing pores in the middle of the construct, we increased the surface area which was in direct contact with nutrient enhanced media.

We also hypothesized that cell distribution throughout the scaffold would increase with the addition of macropores. To quantify cell distribution, we imaged constructs in three regions: superficial zone (top) where the cells were introduced post-printing, middle, and deep zone (bottom) (Figure 4.4). We intentionally seeded the cells on one side of the construct, rather than printing cells in the bioink to mimic the clinical process of microfracture, where bone marrow cells are introduced to the defect region from only one side. Surprisingly, all experimental scaffold groups showed cell distribution throughout the construct after 7 days of culture. However, the only group that showed a consistent decreasing trend from the superficial layer to the bottom layer (50% cells in top, 30% cells in middle, and 20% at the bottom) was the molded construct with no macropores (Figure 4.4). The group with a 75% infill, and therefore pores on the order of 300-400 µm (Figure 4.3), also displayed a trend of decreasing cell percentage from the surface to the other two layers, but displayed the smallest percentage of cells in the middle, rather than the deep zone of the construct. In contrast, 35% pores displayed similar cell content in all layers (30-40% of cells in each layer) (Figure 4.4).

4.3.6 ECM particle bioink adheres to native articular cartilage surface *in situ*

Integration between a tissue engineered replacement and native articular cartilage is challenging and thus one of the most important considerations for a successful repair solution [45, 47, 73, 140, 141, 72]. We printed a custom scaffold to fit the exact dimensions of a defect made in a viable articular cartilage explant (Figure 4.5). Immediately after printing (using 75% infill), we placed the 3D printed construct into the viable plug to polymerize, aiming to line up the surface of the explant and the construct (Figure 4.5). After polymerization, we seeded primary chondrocytes and cultured the explants for 7 days. After 7 days, we bisected the repaired explant and observed adhesion between the 3D printed construct and the native tissue, as the repair was not dislodged

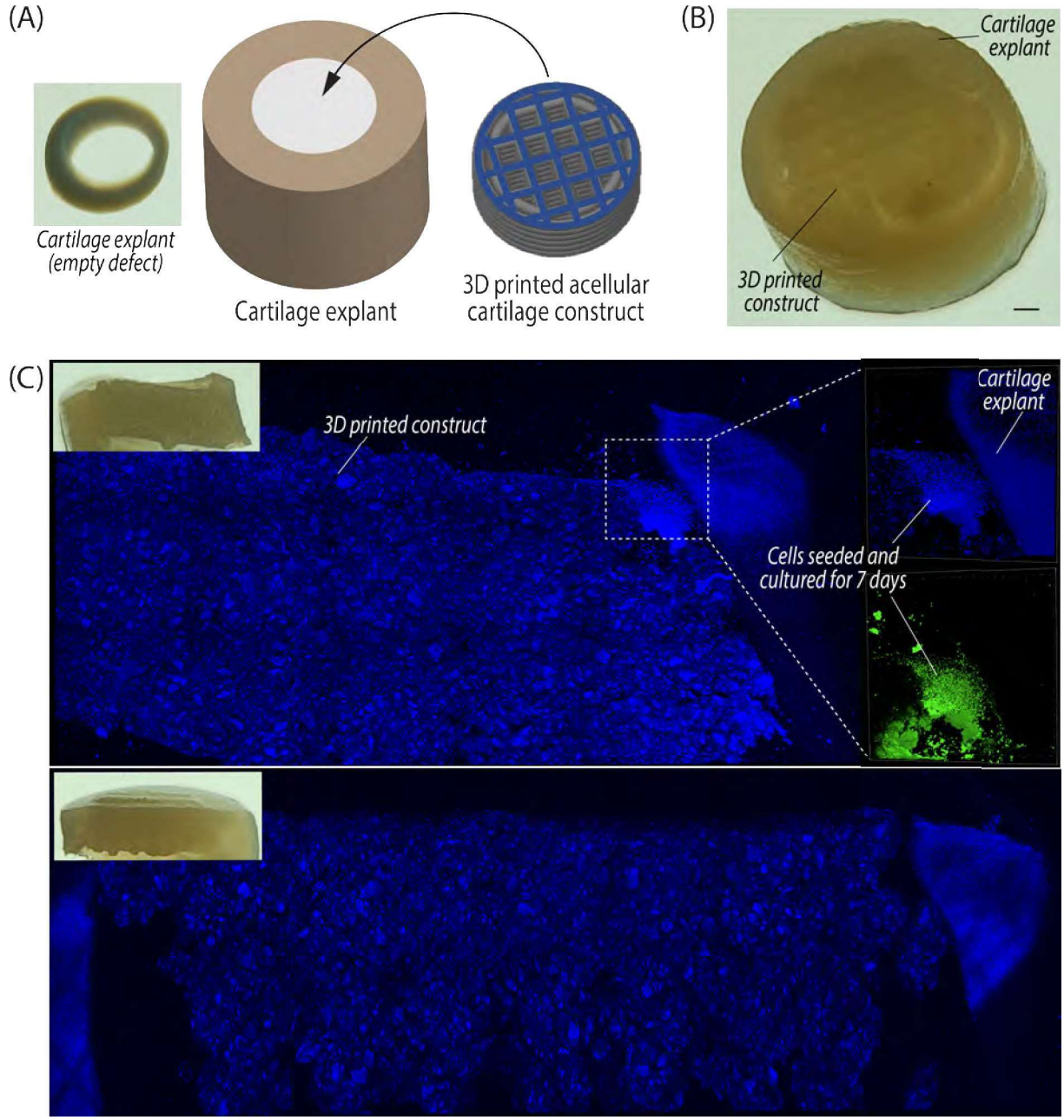

Figure 4.5: pECM bioink can be designed and printed to fill a tissue defect and after 7 days the printed construct integrates and adheres to the surrounding native tissue. (A, B) Custom tissue defects are measured and inputted into CAD software to create a construct custom designed to fit the defect. Extrusion printing is used to create the custom construct and immediately introduced to the defect for polymerization. (C) After 7 days, constructs were bisected and imaged for direct observation of scaffold integrity and integration with native tissue. Scaffolds adhere to the native tissue, even with the forces exerted during bisecting. Additionally, CFSE stained cells (green) which were introduced after polymerization collect where the native tissue and scaffold meet.

during cutting and manipulation. Imaging across the constructs illustrated the direct interaction between tissues and the cell distribution possible in a viable cartilage sample (Figure 4.5).

4.3.7 Printing enables on-demand defect specific design of scaffolds for surgical implementation

To further investigate the clinical repair potential of ECM particle bioink, we repaired a site of damage on the articular cartilage of a bovine knee joint. Using the standard clinical Arthrex tools, we demonstrated that we could debride the injury site, measure the dimensions of the defect, input dimensions in real time to a 3D model (Figure 4.6), and print the pattern using articular cartilage ECM particle bioink with a hyaluronan superficial layer (Figure 4.6). The process is straightforward, customizable, and relatively quick – a potentially powerful clinical scaffolding technique. With a straightforward and rapid ability to manufacture a repair for a custom defect, surgeons could define the joint surface and defect shape, print the exact repair scaffold needed, and implant into a patient. Additionally, if the surgeon could use pre-op visits and advanced medical imaging (i.e. MRI) to define the extent of injury and approximate defect shape/size, implants could alternatively be printed just prior to surgery, decreasing surgical time where the wound is open.

4.4 Discussion

In this work, we developed an acellular ECM particle bioink and used it to 3D print a layered articular cartilage scaffold. The printed scaffold mimics both compressive and lubricative properties of native tissue and facilitates cell homing and cell viability of introduced chondrocytes. We developed stable and natural polymer-based 3D constructs by leveraging disulfide bonding to crosslink acellular tissue particles with thiol functionalized hyaluronan. To form our novel composite 3D construct, no added photo initiators or potentially toxic UV light is required. Furthermore, we demonstrated that printing ECM particle bioink enables completely unique inks to be printed in layers, replicating non-homogenous tissues such as articular cartilage. We confirmed that printing a superficial layer of hyaluronan on the surface of constructs creates a smooth and low friction

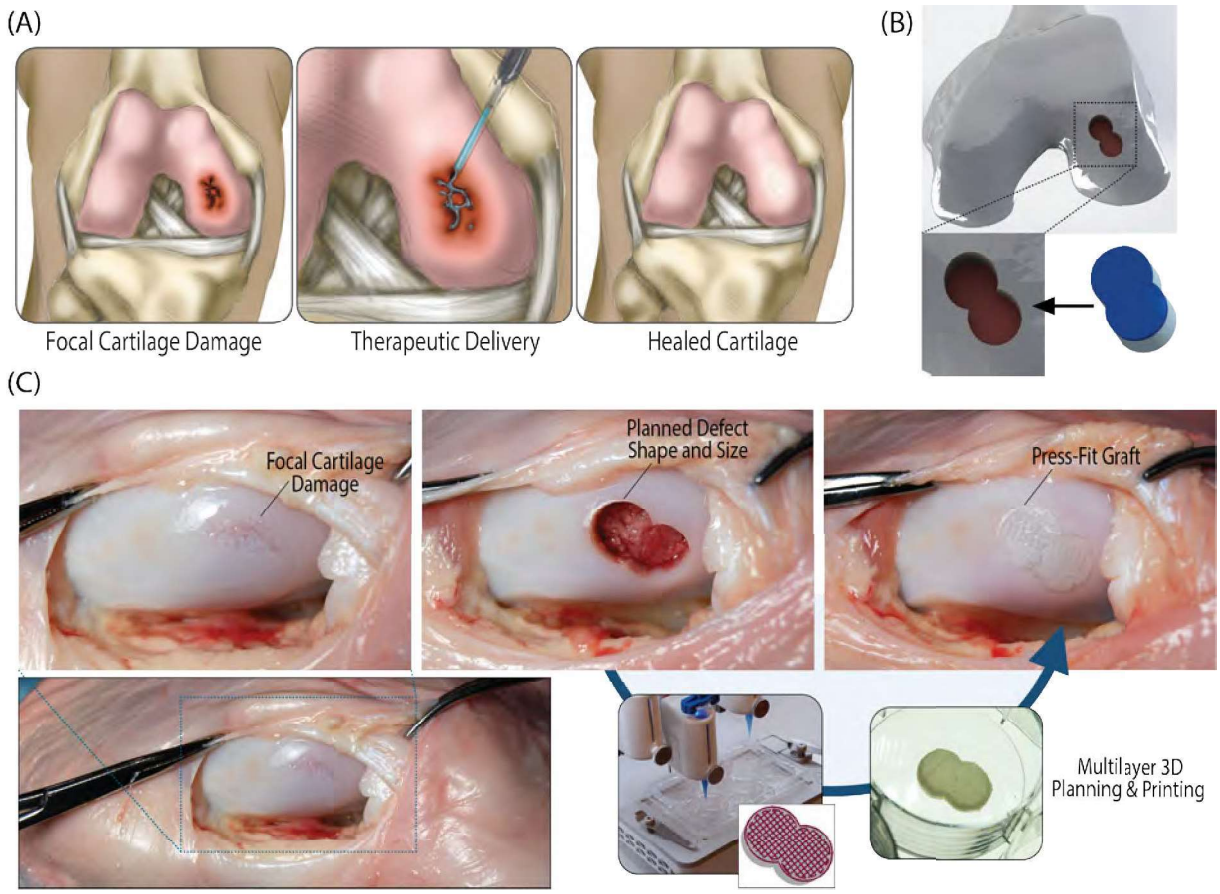

Figure 4.6: The printing of ECM particle bioink is straightforward, tunable for a wide variety of shapes and sizes, and shows potential for clinical on-demand applications. (A) For clinical applications, it is essential to develop a material that can be applied to patient specific defects, which can vary in terms of size and extent of focal cartilage damage within a complex joint. (B, C) With the ECM particle bioink, we demonstrate that a custom defect shape can be measured, applied to a 3D CAD model, and printed via extrusion to create a multilayered construct suitable for implantation. Here, planning of a two-layer cartilage construct, using tissue particles for enhanced tissue structure in addition to an engineered lubrication layer, is printed and applied immediately to repair a joint defect.

surface, while the bulk of the construct maintains much higher compressive mechanical properties.

The most common technique to treat articular cartilage defects is known as microfracture, a procedure where the surgeon drills into the patient's bone marrow to create a blood clot that fills the defect. This technique presents various drawbacks such as limited surface area and depth that can be treated and limited healing success. Microfracture promotes tissue formation that is highly fibrous and is unlike the unique hyaline cartilage naturally present in the joint. We anticipate that our results will directly lead to development of an acellular repair strategy that can be applied to articular cartilage damage. Additionally, the cell-cell communication between layers of tissue (i.e. cartilage to bone or the specific layers in cartilage) in regeneration models is not well understood because most regeneration models focus on a single tissue type or tissue layer. The ECM particle bioink and method developed here to create a functional layered tissue can be used as a tool to tease apart cellular communication in several tissue repair systems, such as cartilage-bone crosstalk, muscle to skin communication during regeneration, or differential cell expression in superficial versus deep zones of cartilage.

The work presented here is an important first step in the optimization of 3D printing with a tissue particulate bioink. However, there are several limitations. Importantly, articular cartilage is made up of three distinct tissue zones (superficial, middle, and deep) which lie on top of subchondral bone. An ideal 3D printed bio scaffold would print all three layers, rather than the two distinct layers shown here, with a small region of subchondral bone beneath to anchor the scaffold. The technological and material advancements of this study will enable complex zonal cartilage printing as we are now poised to print tissue particulate bioink sourced from each distinct layer. Additionally, all experiments were performed *in vitro*, and it will be critical to know the efficacy of the 3D printed ECM particle bioink constructs under consistent loading in a future *in vivo* model.

The development of extracellular matrix-based bioinks for use in conjunction with modular 3D fabrication techniques will enable printing of naturally crosslinked acellular tissue scaffolds for regeneration of many complex tissues damaged by trauma. The work in this study is focused around articular cartilage, but the fabrication techniques developed hold promise for use across a variety

of trauma applications, such as deep wounds, that affect multiple tissue layers (i.e. the epidermis, dermis, adipose, and muscle all injured in a deep wound). ECM particle bioinks represent a novel concept and natural extension of recent particulate tissue clay technology which could drastically improve clinical patient outcomes and *in vitro* tissue models for studying disease progression or treatment efficacy.

4.5 Methods

4.5.1 Decellularization of particles

Porcine tissue was sourced from a local butcher within 48 hours of slaughter. The articular cartilage was collected from the knee by exposing the joint space and removing tissue with a scalpel, taking care not to include calcified tissue beneath the cartilage. All cartilage tissue was pooled together from several animals to create a single batch and pulverized in a liquid nitrogen freezer mill. Microparticles were decellularized first in 2% SDS for 8 hours under agitation at 37°C, and then in 0.1% DNase for 3 hours to remove cellular and genetic material. Microparticles were rinsed in PBS overnight, flash frozen in liquid nitrogen, lyophilized, and stored frozen at -80°C.

4.5.2 Size selecting 40-100 µm cartilage particles for bioink

Lyophilized acellular cartilage tissue particles were pulverized further in stainless steel grinding jars on the TissueLyser II (Qiagen). Following pulverization, particles were size sorted using a vibrational sieve (Endecott) into three distinct sizes: <40 µm, 40-100 µm, and 100-250 µm. For all studies reported here, 40-100 µm particles were used.

4.5.3 Thiolating hyaluronic acid

Glucoronate carboxyl groups on hyaluronan (HA) were replaced with thiol groups following previously established protocols [106]. Briefly, hyaluronan (MW 100 kDa, Lifecore Biomedical) was dissolved at 10 mg/ml in degassed milliQ water. Dithiobis propanoic dihydrazide (DTP)(Frontier

Scientific) was added to the solution, the pH was lowered to between 4.5 and 4.75, and then (1-ethyl-3-(3-dimethylaminopropyl) carbodiimide (EDC) (ThermoFisher) was added to begin the reaction. The pH was maintained between 4.5 and 5 for 50 minutes. After 50 minutes, the reaction was stopped by raising the pH above 7. Next, dithiotreitol (DTT)(Fisher Scientific) was added, the pH was raised above 8.5, and the solution was stirred for 24 hours at room temperature. After 24 hours, the pH of the solution was lowered, the liquid transferred to dialysis tubing (10 kDa membrane cutoff, Spectrum Labs) and the solution was dialyzed in an HCl solution supplemented with 100 mM sodium chloride for 8 solution changes, then in an HCl solution without supplements for 4 solution changes. Dialysis was completed in a sealed chamber with continuous nitrogen gas bubbling into the HCl solution. With each batch of HA thiolation, the substitution rate was confirmed to be 15-20% using a standard Ellman's assay following manufacturer's protocol (Ellman's solution, ThermoFisher).

4.5.4 Fabrication of ECM bioinks

Lyophilized HA that had previously been thiolated to 20% (see above), dissolved easily when introduced to sterile DPBS (Hyclone), to create an aqueous solution of 20 mg/ml of HA which was neutralized and loaded into a syringe, taking care to remove any bubbles that formed in syringe loading. In a separate syringe, acellular size sorted tissue particles were mixed with DPBS at a ratio of 0.4 g/ml. Once ready to print syringes were attached to each other using a custom luer lock connector with cross hairs across the opening to facilitate mixing. Solutions were syringed back and forth 30 times until mixing was complete and the material ran smoothly through the luer lock mixing connector. The final mixture had an HA concentration of 10 mg/ml and particle concentration of 0.2 g/ml. Freshly mixed ink was loaded into printing cartridges and print was started within 5-10 minutes of mixing. For the lubricating HA only ink, aqueous 20 mg/ml HA solution was mixed and incubated at 37°C for 4 hours to facilitate initial crosslinking prior to loading in the print cartridge for extrusion.

4.5.5 3D printing of pECM bioink

pECM bioink, freshly prepared, was printed using direct ink writing on a sterile multi-nozzle extrusion printer (BioX, Cell Ink Life Sciences). 3D print designs were created in open source CAD software (OnShape), following guidelines for typical critical size cartilage defects defined by Arthrex (8 mm diameter, 2 mm height) and transferred to the 3D printer for segmenting. ECM particle bioink was extruded using a pneumatic print cartridge and a 22-gauge nozzle. Ink was extruded with 70-90 kPa pressure (adjusted in real time to ensure print consistency between layers) at a rate of 2 mm/s. The ink was set to pre-flow and post-flow for 30ms before and after print steps. Ink was printed with 35% infill or a 75% infill using a grid pattern for the two different experimental groups. For the top lubrication layer, the ink was printed with 3-10 kPa of pressure and a speed of 20 mm/s with no pre or post flow. Nozzles were calibrated prior to printing to ensure alignment of the multiple printheads and unique inks.

4.5.6 Mechanical Testing

Compressive moduli of 3D printed scaffolds were measured using unconfined compression testing on a Bose ElectroForce 5500 system. After contacting the surface of the construct with a 0.1N pre-load, the constructs were compressed to a strain of 40% of the initial height (0.1% per second). Compressive modulus was calculated by measuring the slope of the linear portion of the stress strain curve, between 30% and 40% strain.

4.5.7 Swelling Studies of 3D printed construct

After polymerization, the constructs were incubated for 48 hours in PBS at 37°C. Moisture was removed from constructs with a kimwipe, and constructs were weighed. All constructs were lyophilized for 24 hours and weighed again. Wet weight was divided by the dry weight and multiplied by 100 to calculate the swelling percentage.

4.5.8 TCEP Buffer assay to break apart disulfide bonds

0.05M tris(2-carboxyethyl)phosphine (TCEP) buffer was made by dissolving TCEP in MilliQ water and adjusting the pH to 7. TCEP buffer was added to two groups of polymerized, and hydrated hydrogels: HA/PEGDA with tissue particle gels and HA with tissue particle gels. The gels were submerged in TCEP buffer for 24 hours with constant agitation.

4.5.9 Ellman's assay to test for open thiol groups on particles

Ellman's Reagent (5,5'-dithio-bis-[2-nitrobenzoic acid]) (ThermoFisher) was used to estimate sulfhydryl groups on both the thiol functionalized hyaluronan and acellular cartilage tissue particles by comparing to the standard curve of the known sulfhydryl-containing compound cysteine. The solution reacts with any free sulfhydryl group to produce a colored species that can be measured using UV-vis absorbance on a plate reader. Briefly, Ellman's reagent solution was prepared by dissolving 4mg of Ellman's reagent into 1 mL of reaction buffer (1M sodium phosphate, 1mM EDTA, pH 8.0). For each unknown sample, 250 µl of sample is combined with 2.5 mL reaction buffer and 50 µl Ellman's reagent solution. The mixtures were vortexed thoroughly and incubated at room temperature for 15 minutes. A plate reader set to read UV-vis at 412 nm was used to measure absorbance of each sample. Unknown samples were compared to a standard curve of cysteine hydrochloride monohydrate (ThermoFisher) dilutions to determine quantity of -SH groups.

4.5.10 Chondrocyte digestion, CFSE stain, and seeding

Primary chondrocytes were sourced from juvenile bovine knee joints within 12 hours of slaughter (Research 87). Chondrocytes were harvested by exposing the joint space and removing articular cartilage with a scalpel. Cartilage was minced into <1mm pieces using a sterile razor blade, rinsed in sterile PBS three times, and digested in a solution of 0.2% collagenase-P (Roche Pharmaceuticals) added to Dulbecco's Modified Eagle Medium: a nutrient mixture F12 (DMEM-F12, Gibco) supplemented with 3% fetal bovine serum, 0.1% bovine serum albumin, 100 units/mL penicillin, 100

ug/mL streptomycin, and 50 ug/mL ascorbate-2-phosphate. To enable later cell visualization in the 3D printed constructs, freshly extracted chondrocytes were stained with carboxyfluorescein succinimidyl ester (CFSE) (Invitrogen) prior to seeding. The chondrocyte cell pellet was resuspended in a 5µM CFSE solution, incubated for 20 minutes at 37°C, and quenched using serum-supplemented (10% FBS) defined chondrocyte medium for 5 minutes at 37°C. After quenching was complete, 10 million cells were seeded on top of polymerized 3D printed constructs in 40 µl of media. After 15 minutes, 5 mL of chondrogenic medium (DMEM-F12 supplemented with 10% FBS, 0.1% bovine serum albumin, 100 units/mL penicillin, 100 ug/mL streptomycin, and 50 ug/mL ascorbate-2-phosphate) was added and maintained for 14 days, with media replacement every other day.

4.5.11 Cell viability and live/dead staining

Chondrocyte-seeded constructs were stained and imaged at 7 and 14 days on a Nikon inverted confocal microscope to quantify relative levels of cell death throughout the construct. Constructs were submerged in a sterile 4 µM EthD-1 solution (ThermoFisher), incubated for 30 minutes at room temperature, and then rinsed in sterile, tissue grade D-PBS (Hyclone). Constructs were bisected using a sterile razor blade, and three unique locations on the cross section of each construct were imaged using a 20x objective. CFSE stained live cells were detected with a 485 nm laser, while EthD-1 stained dead cells were detected with a 560 nm laser.

4.5.12 Fluorescence staining for bioink structure

3D printed constructs from the three experimental conditions (35% infill, 75% infill, and molded) were stained for 10 minutes with DAPI stain (ThermoFisher) at a concentration of 5µl DAPI/ 1 ml DPBS. Constructs were imaged on an inverted Nikon A1 confocal microscope with a standard 405 nm laser and 10× objective. A montage of the entire 8 mm construct was taken using large image acquisition, with a 70 µm z-stack at each location (the images presented in Figure 4.3 are the maximum intensity z projection to ensure all construct architecture is visible).

4.5.13 Donut assay with viable cartilage plug

10 mm diameter bovine cartilage explants were extracted from juvenile bovine knee joints within 12 hours of slaughter (Research 87) using sterilized cork bores (ThermoFisher). Explants were rinsed 3 times in sterile PBS and an inner defect of 8 mm in diameter was made using a smaller size cork bore, recently sharpened to decrease cell death. Cartilage explants were rinsed and submerged in chondrogenic medium (DMEM-F12 supplemented with 10% FBS, 0.1% bovine serum albumin, 100 units/mL penicillin, 100 ug/mL streptomycin, and 50 ug/mL ascorbate-2-phosphate) while 3D printed constructs were printed. For each cartilage ring, we printed a 75% infill density construct (as detailed above). Immediately after printing, the constructs were placed in the cartilage rings, left to polymerize for 30 min at 37 °C, and submerged in chondrogenic medium. Several hours later, CFSE stained chondrocytes were seeded on top of constructs (detailed above) and explants were cultured for 7 days prior to bisecting and confocal imaging.

4.5.14 Custom defect 3D print in knee joint

A juvenile bovine knee joint was opened to expose the femoral condyle. After a defect was created that mimicked typical wear and tear cartilage defects, Arthrex allograft tools were used to make two circular defects, overlapping to cover the area of cartilage damage. The custom defect was measured, the measurements were incorporated into a CAD drawing, and transferred to the 3D printer for segmenting. The design was printed out of pECM bioink with the topmost layer composed of only hyaluronic acid. Immediately post printing, the construct was applied to the defect region to promote polymerization post-implantation, a key process for native tissue integration.

4.5.15 Statistical Analysis

To test our hypotheses that treatment (either print density or surface type) influenced the scaffold properties (stiffness, surface roughness, adhesion, friction, cell viability), two-way analyses of variance (ANOVAs) were performed on generalized linear models with treatment as the predictor

and the resulting measurement variable as the response. In all data sets, if treatment (print density of surface type, depending on the experimental setup) was found to be a significant predictor then the p-value significance between each group was calculated using Tukey's Honest Significant Difference Test. Statistical significance in all experiments was defined as $p<0.05$, and noted if $p<0.001$. All statistical testing was performed using R software.

Bibliography

[1] Loeser, R. F., Goldring, S. R., Scanzello, C. R. & Goldring, M. B. Osteoarthritis: A disease of the joint as an organ. Arthritis and Rheumatism **64**, 1697–1707 (2012).

[2] Otsuki, S. et al. The effect of glycosaminoglycan loss on chondrocyte viability: a study on porcine cartilage explants. Arthritis Rheum **58**, 1076–1085 (2008). URL `http://www.ncbi.nlm.nih.gov/pubmed/18383360`.

[3] Quinn, T. M., Grodzinsky, A. J., Hunziker, E. B. & Sandy, J. D. Effects of injurious compression on matrix turnover around individual cells in calf articular cartilage explants. J Orthop Res **16**, 490–499 (1998). URL `http://www.ncbi.nlm.nih.gov/pubmed/9747792`.

[4] Cleveland, R. J. et al. Independent associations of socioeconomic factors with disability and pain in adults with knee osteoarthritis. BMC Musculoskeletal Disorders **14** (2013).

[5] Hochberg, M., Cisternas, M. & Watkins-Castillo, S. Osteoarthritis (2014).

[6] Bitton, R. The Economic Burden of Osteoarthritis. American Journal of Managed Care (2009).

[7] Hootman, J. M., Helmick, C. G., Barbour, K. E., Theis, K. A. & Boring, M. A. Updated Projected Prevalence of Self-Reported Doctor-Diagnosed Arthritis and Arthritis-Attributable Activity Limitation Among US Adults, 2015-2040. Arthritis & Rheumatology **68**, 1582–1587 (2016). URL `http://doi.wiley.com/10.1002/art.39692`.

[8] Zhang, L., Hu, J. & Athanasiou, K. A. The role of tissue engineering in articular cartilage repair and regeneration. Critical reviews in biomedical engineering **37**, 1–57 (2009).

[9] Mow, V. C., Gu, W. Y. & Chen, F. H. No Title. In Basic Orthopaedic Biomechanics and Mechano-Biology, chap. 5, 181–258 (Lippincott Williams & Wilkins, Philadelphia, PA, 2005), 3rd edn.

[10] Hardingham, T. Cartilage tissue regeneration. Electrospinning for Tissue Regeneration **1**, 111–126 (2011).

[11] Mow, V. C., Ateshian, G. A. & Spilker, R. L. Biomechanics of diarthrodial joints: a review of twenty years of progress. J Biomech Eng **115**, 460–467 (1993). URL `http://www.ncbi.nlm.nih.gov/pubmed/8302026`.

[12] Guilak, F., Nims, R. J., Dicks, A., Wu, C.-L. & Meulenbelt, I. Osteoarthritis as a disease of the cartilage pericellular matrix. Matrix Biology (2018).

[13] Wilusz, R. E., Sanchez-Adams, J. & Guilak, F. The structure and function of the pericellular matrix of articular cartilage (2014).

[14] Bayliss, L. E. et al. The effect of patient age at intervention on risk of implant revision after total replacement of the hip or knee: a population-based cohort study. The Lancet **389**, 1424–1430 (2017). URL http://dx.doi.org/10.1016/.

[15] Losina, E. et al. Lifetime medical costs of knee osteoarthritis management in the United States: Impact of extending indications for total knee arthroplasty. Arthritis care & research **67**, 203 (2015). URL http://www.ncbi.nlm.nih.gov/pubmed/25048053 http://www.pubmedcentral.nih.gov/articlerender.fcgi?artid=PMC4422214.

[16] Felson, D. T. et al. Osteoarthritis: new insights. Part 2: treatment approaches. Ann Intern Med **133**, 726–737 (2000). URL http://www.ncbi.nlm.nih.gov/pubmed/11074906.

[17] St-Onge, M. P. & Gallagher, D. Body composition changes with aging: The cause or the result of alterations in metabolic rate and macronutrient oxidation? (2010).

[18] Felson, D. T., Zhang, Y., Anthony, J. M., Naimark, A. & Anderson, J. J. Weight loss reduces the risk for symptomatic knee osteoarthritis in women. The Framingham Study. Ann Intern Med **116**, 535–539 (1992). URL http://www.ncbi.nlm.nih.gov/pubmed/1543306.

[19] Messier, S. P., Gutekunst, D. J., Davis, C. & DeVita, P. Weight loss reduces knee-joint loads in overweight and obese older adults with knee osteoarthritis. Arthritis and Rheumatism **52**, 2026–2032 (2005).

[20] Messier, S. P. et al. Effects of intensive diet and exercise on knee joint loads, inflammation, and clinical outcomes among overweight and obese adults with knee osteoarthritis: The IDEA randomized clinical trial. JAMA - Journal of the American Medical Association **310**, 1263–1273 (2013).

[21] Mithoefer, K., McAdams, T., Williams, R. J., Kreuz, P. C. & Mandelbaum, B. R. Clinical efficacy of the microfracture technique for articular cartilage repair in the knee: an evidence-based systematic analysis. Am J Sports Med **37**, 2053–2063 (2009). URL http://www.ncbi.nlm.nih.gov/pubmed/19251676.

[22] Williams, G. M. et al. Shape, loading, and motion in the bioengineering design, fabrication, and testing of personalized synovial joints. Journal of Biomechanics **43**, 156–165 (2010).

[23] Solheim, E. et al. Osteochondral autografting (mosaicplasty) in articular cartilage defects in the knee: results at 5 to 9 years. Knee **17**, 84–87 (2010). URL http://www.ncbi.nlm.nih.gov/pubmed/19666226.

[24] Huang, B. J., Hu, J. C. & Athanasiou, K. A. Cell-based tissue engineering strategies used in the clinical repair of articular cartilage. Biomaterials **98**, 1–22 (2016). URL http://linkinghub.elsevier.com/retrieve/pii/S0142961216301296.

[25] Bentley, G. et al. Minimum ten-year results of a prospective randomised study of autologous chondrocyte implantation versus mosaicplasty for symptomatic articular cartilage lesions of the knee. J Bone Joint Surg Br **94**, 504–509 (2012). URL http://www.ncbi.nlm.nih.gov/pubmed/22434467.

[26] Duif, C. et al. Combination of autologous chondrocyte implantation (ACI) and osteochondral autograft transfer system (OATS) for surgical repair of larger cartilage defects of the knee joint. A review illustrated by a case report. Technol Health Care **23**, 531–537 (2015). URL http://www.ncbi.nlm.nih.gov/pubmed/26410114.

[27] Knutsen, G. et al. A Randomized Multicenter Trial Comparing Autologous Chondrocyte Implantation with Microfracture: Long-Term Follow-up at 14 to 15 Years. J Bone Joint Surg Am **98**, 1332–1339 (2016). URL https://www.ncbi.nlm.nih.gov/pubmed/27535435.

[28] Peterson, L., Vasiliadis, H. S., Brittberg, M. & Lindahl, A. Autologous chondrocyte implantation: a long-term follow-up. Am J Sports Med **38**, 1117–1124 (2010). URL http://www.ncbi.nlm.nih.gov/pubmed/20181804.

[29] Camarero-Espinosa, S., Rothen-Rutishauser, B., Weder, C. & Foster, E. J. Directed cell growth in multi-zonal scaffolds for cartilage tissue engineering. Biomaterials **74**, 42–52 (2016). URL

[30] Knee Replacement in Younger Patients.

[31] Williams, S. N., Wolford, M. L. & Bercovitz, A. Hospitalization for Total Knee Replacement Among Inpatients Aged 45 and Over: United States, 2000-2010. NCHS Data Brief 1–8 (2015). URL http://www.ncbi.nlm.nih.gov/pubmed/26375255.

[32] Camarero-Espinosa, S., Rothen-Rutishauser, B., Foster, E. J. & Weder, C. Articular cartilage: From formation to tissue engineering (2016).

[33] Faust, H. J., Guo, Q. & Elisseeff, J. H. Cartilage Tissue Engineering. Principles of Regenerative Medicine 937–952 (2019). URL https://www.sciencedirect.com/science/article/pii/B9780128098806000539.

[34] United States Bone and Joint Initiative. The Burden of Musculoskeletal Diseases in the United States (2018).

[35] Arthritis Foundation. Arthritis by the Numbers (2019).

[36] Levy, Y. D., Görtz, S., Pulido, P. A., McCauley, J. C. & Bugbee, W. D. Do fresh osteochondral allografts successfully treat femoral condyle lesions? Knee. In Clinical Orthopaedics and Related Research, vol. 471, 231–237 (Springer New York LLC, 2013). URL /pmc/articles/PMC3528935/?report=abstract https://www.ncbi.nlm.nih.gov/pmc/articles/PMC3528935/.

[37] Torrie, A. M., Kesler, W. W., Elkin, J. & Gallo, R. A. Osteochondral allograft (2015). URL /pmc/articles/PMC4630219/?report=abstract https://www.ncbi.nlm.nih.gov/pmc/articles/PMC4630219/.

[38] Novak, T. et al. In Vivo Cellular Infiltration and Remodeling in a Decellularized Ovine Osteochondral Allograft. Tissue Eng Part A **22**, 1274–1285 (2016). URL https://www.ncbi.nlm.nih.gov/pubmed/27673714.

[39] Albro, M. B. et al. Raman spectroscopic imaging for quantification of depth-dependent and local heterogeneities in native and engineered cartilage. npj Regenerative Medicine **3**, 3 (2018). URL http://www.nature.com/articles/s41536-018-0042-7.

[40] Bergholt, M. S. et al. Raman Spectroscopy Reveals New Insights into the Zonal Organization of Native and Tissue-Engineered Articular Cartilage (2016). URL http://pubs.acs.org/journal/acscii.

[41] Bonifacio, A. et al. Chemical imaging of articular cartilage sections with Raman mapping, employing uni-and multi-variate methods for data analysis URL http://pubs.rsc.org/en/content/articlepdf/2010/AN/C0AN00459F.

[42] Fischenich, K. M. et al. Human articular cartilage is orthotropic where microstructure , micromechanics , and chemistry vary with depth and split-line orientation. Osteoarthritis and Cartilage 1–11 (2020).

[43] Goretti, M., Penido, M. G. & Alon, U. S. Phosphate homeostasis and its role in bone health URL www.endotext.org.

[44] Chan, S. M., Neu, C. P., DuRaine, G., Komvopoulos, K. & Reddi, A. H. Atomic force microscope investigation of the boundary-lubricant layer in articular cartilage. Osteoarthritis and Cartilage **18**, 956–963 (2010). URL http://dx.doi.org/10.1016/j.joca.2010.03.012.

[45] Ahsan, T. & Sah, R. L. Biomechanics of integrative cartilage repair. Osteoarthritis and Cartilage **7**, 29–40 (1999).

[46] Hunziker, E. B. Articular cartilage repair: Basic science and clinical progress. A review of the current status and prospects. Osteoarthritis and Cartilage **10**, 432–463 (2002).

[47] Bos, P. K., DeGroot, J., Budde, M., Verhaar, J. A. N. & van Osch, G. J. V. M. Specific enzymatic treatment of bovine and human articular cartilage: Implications for integrative cartilage repair. Arthritis & Rheumatism **46**, 976–985 (2002). URL http://doi.wiley.com/10.1002/art.10208.

[48] Boushell, M. K. et al. Polymeric mesh and insulin-like growth factor 1 delivery enhance cell homing and graftcartilage integration. Annals of the New York Academy of Sciences **1442**, 138–152 (2019). URL https://onlinelibrary.wiley.com/doi/abs/10.1111/nyas.14054.

[49] Hanley, E. N. Instructional Course Lectures. The Journal of Bone & Joint Surgery **86**, 2587–2588 (2004).

[50] Jiang, S. et al. Review Article Clinical Application Status of Articular Cartilage Regeneration Techniques: Tissue-Engineered Cartilage Brings New Hope (2020). URL https://doi.org/10.1155/2020/5690252.

[51] Gudas, R. et al. A prospective randomized clinical study of mosaic osteochondral autologous transplantation versus microfracture for the treatment of osteochondral defects in the knee joint in young athletes. Arthroscopy - Journal of Arthroscopic and Related Surgery **21**, 1066–1075 (2005).

[52] Rogers, B. A., David, L. A. & Briggs, T. W. R. Sequential outcome following autologous chondrocyte implantation of the knee: A six-year follow-up .

[53] Hangody, L. & Füles, P. Autologous osteochondral mosaicplasty for the treatment of full-thickness defects of weight-bearing joints: Ten years of experimental and clinical experience. In Journal of Bone and Joint Surgery - Series A, vol. 85, 25–32 (2003). URL https://pubmed.ncbi.nlm.nih.gov/12721342/.

[54] Aachoui, Y. & Ghosh, S. K. Extracellular matrix from porcine small intestinal submucosa (SIS) as immune adjuvants. PLoS ONE **6**, 27083 (2011). URL /pmc/articles/PMC3210130/?report=abstract https://www.ncbi.nlm.nih.gov/pmc/articles/PMC3210130/.

[55] Bejjani, G. K. & Zabramski, J. Safety and efficacy of the porcine small intestinal submucosa dural substitute: Results of a prospective multicenter study and literature review (2007). URL https://thejns.org/view/journals/j-neurosurg/106/6/article-p1028.xml.

[56] Brown, B. N. & Badylak, S. F. Extracellular Matrix as an Inductive Scaffold for Functional Tissue Reconstruction. In Translating Regenerative Medicine to the Clinic (2015).

[57] Ahern, B. J., Parvizi, J., Boston, R. & Schaer, T. P. Preclinical animal models in single site cartilage defect testing: a systematic review (2009).

[58] Chu, C. R., Szczodry, M. & Bruno, S. Animal Models for Cartilage Regeneration and Repair. Tech. Rep. URL www.liebertonline.com=ten.

[59] Cook, J. L. et al. Animal models of cartilage repair **3** (2014).

[60] Brehm, W. et al. Repair of superficial osteochondral defects with an autologous scaffold-free cartilage construct in a caprine model: implantation method and short-term results. Osteoarthritis and Cartilage **14**, 1214–1226 (2006).

[61] Dorotka, R., Bindreiter, U., Macfelda, K., Windberger, U. & Nehrer, S. Marrow stimulation and chondrocyte transplantation using a collagen matrix for cartilage repair. Osteoarthritis and Cartilage **13**, 655–664 (2005).

[62] Dorotka, R. et al. Repair of articular cartilage defects treated by microfracture and a three-dimensional collagen matrix. Biomaterials **26**, 3617–3629 (2005).

[63] Burks, R. T., Greis, P. E., Arnoczky, S. P. & Scher, C. The use of a single osteochondral autograft plug in the treatment of a large osteochondral lesion in the femoral condyle: An experimental study in sheep. American Journal of Sports Medicine **34**, 247–255 (2006). URL http://journals.sagepub.com/doi/10.1177/0363546505279914.

[64] Lane, J. G. et al. Follow-up of osteochondral plug transfers in a goat model: A 6-month study. American Journal of Sports Medicine **32**, 1440–1450 (2004). URL http://journals.sagepub.com/doi/10.1177/0363546504263945.

[65] Lu, Y. et al. Minced cartilage without cell culture serves as an effective intraoperative cell source for cartilage repair. Journal of Orthopaedic Research **24**, 1261–1270 (2006). URL http://doi.wiley.com/10.1002/jor.20135.

[66] Siebert, C. H. et al. Ingrowth of osteochondral grafts under the influence of growth factors: 6-month results of an animal study. Archives of Orthopaedic and Trauma Surgery **126**, 247–252 (2006). URL https://link.springer.com/article/10.1007/s00402-005-0061-x.

[67] Tibesku, C. O. et al. Hyaline cartilage degenerates after autologous osteochondral transplantation URL www.elsevier.com/locate/orthres.

[68] Tytherleigh-Strong, G., Hurtig, M. & Miniaci, A. Intra-articular hyaluronan following autogenous osteochondral grafting of the knee. Arthroscopy - Journal of Arthroscopic and Related Surgery **21**, 999–1005 (2005).

[69] von Rechenberg, B. et al. Changes in subchondral bone in cartilage resurfacing - An experimental study in sheep using different types of osteochondral grafts. Osteoarthritis and Cartilage **11**, 265–277 (2003).

[70] Kandel, R. A. et al. Repair of osteochondral defects with biphasic cartilage-calcium polyphosphate constructs in a Sheep model. Biomaterials **27**, 4120–4131 (2006).

[71] Niederauer, G. G. et al. Evaluation of multiphase implants for repair of focal osteochondral defects in goats. Biomaterials **21**, 2561–2574 (2000).

[72] Wang, D.-A. et al. Multifunctional chondroitin sulphate for cartilage tissue–biomaterial integration (2007). URL https://www.nature.com/articles/nmat1890.pdf.

[73] Boushell, M. K., Hung, C. T., Hunziker, E. B., Strauss, E. J. & Lu, H. H. Connective Tissue Research Current strategies for integrative cartilage repair (2016). URL https://www.tandfonline.com/action/journalInformation?journalCode=icts20.

[74] Barthold, J. E. et al. Percolation of Microparticle Matrix Promotes Cell Migration and Integration while Supporting Native Tissue Architecture. bioRxiv 2020.08.10.245589 (2020). URL https://doi.org/10.1101/2020.08.10.245589.

[75] Mainil-Varlet, P. et al. A new histology scoring system for the assessment of the quality of human cartilage repair: ICRS II. The American journal of sports medicine **38**, 880–90 (2010). URL http://www.ncbi.nlm.nih.gov/pubmed/20203290.

[76] Unal, M. et al. Assessing matrix quality by Raman spectroscopy helps predict fracture toughness of human cortical bone. Scientific Reports **9**, 1–13 (2019). URL http://dx.doi.org/10.1038/s41598-019-43542-7.

[77] Moore, A. C., Zimmerman, B. K., Chen, X., Lu, X. L. & Burris, D. L. Experimental characterization of biphasic materials using rate-controlled Hertzian indentation. Tribology International **89**, 2–8 (2015).

[78] Chandran, P. L., Dimitriadis, E. K., Mertz, E. L. & Horkay, F. Microscale mapping of extracellular matrix elasticity of mouse joint cartilage: an approach to extracting bulk elasticity of soft matter with surface roughness †. Soft Matter **14**, 2879 (2018).

[79] Hutter, J. L. & Bechhoefer, J. Calibration of atomic-force microscope tips. Review of Scientific Instruments **64**, 3789 (1993). URL https://doi.org/10.1063/1.1143970.

[80] Varenberg, M., Etsion, I. & Halperin, G. An improved wedge calibration method for lateral force in atomic force microscopy. Review of Scientific Instruments **74**, 3298 (2003). URL https://doi.org/10.1063/1.1584082.

[81] Fuhrmann, A. et al. AFM stiffness nanotomography of normal, metaplastic and dysplastic human esophageal cells. Physical Biology **8** (2011).

[82] Nečas, D. & Klapetek, P. Gwyddion: An open-source software for SPM data analysis. Central European Journal of Physics **10**, 181–188 (2012).

[83] Nobuyuki Otsu. A Threshold Selection Method from Gray-Level Histograms. IEEE Trans. Syst. Man Cybern **9**, 62–66 (1979).

[84] Labno, C. Two Ways to Count Cells with ImageJ. Tech. Rep., University of Chicago, Light Microscopy Core.

[85] Cox, T. R. & Erler, J. T. Remodeling and homeostasis of the extracellular matrix: Implications for fibrotic diseases and cancer (2011).

[86] Maroto, R. & Hamill, O. P. MscCa Regulation of Tumor Cell Migration and Metastasis. In Current Topics in Membranes (2007).

[87] Denais, C. M. et al. Nuclear envelope rupture and repair during cancer cell migration. Science **352**, 353–358 (2016).

[88] Wolf, K. et al. Physical limits of cell migration: control by ECM space and nuclear deformation and tuning by proteolysis and traction force. J Cell Biol **201**, 1069–1084 (2013). URL http://www.ncbi.nlm.nih.gov/pubmed/23798731.

[89] Li, Q. et al. Impacts of Maturation on the Micromechanics of the Meniscus Extracellular Matrix HHS Public Access. J Biomech **72**, 252–257 (2018).

[90] Qu, F. et al. Maturation State and Matrix Microstructure Regulate Interstitial Cell Migration in Dense Connective Tissues. Scientific Reports **8**, 3295 (2018). URL www.nature.com/scientificreports.

[91] Heo, S.-J. et al. Nuclear softening expedites interstitial cell migration in fibrous networks and dense connective tissues. Tech. Rep. (2020). URL http://advances.sciencemag.org/.

[92] Novak, T., Seelbinder, B., Twitchell, C. M., Voytik-Harbin, S. L. & Neu, C. P. Dissociated and Reconstituted Cartilage Microparticles in Densified Collagen Induce Local hMSC Differentiation. Advanced Functional Materials **26**, 5427–5436 (2016).

[93] Silva Garcia, J. M., Panitch, A. & Calve, S. Functionalization of hyaluronic acid hydrogels with ECM-derived peptides to control myoblast behavior. Acta Biomaterialia **84**, 169–179 (2019). URL https://doi.org/10.1016/j.actbio.2018.11.030.

[94] Spiller, K. L., Maher, S. A. & Lowman, A. M. Hydrogels for the repair of articular cartilage defects. Tissue Eng Part B Rev **17**, 281–299 (2011). URL http://www.ncbi.nlm.nih.gov/pubmed/21510824.

[95] Novak, T. et al. Mechanisms and Microenvironment Investigation of Cellularized High Density Gradient Collagen Matrices via Densification. Advanced Functional Materials **26**, 2617–2628 (2016).

[96] Sophia Fox, A. J., Bedi, A. & Rodeo, S. A. The basic science of articular cartilage: Structure, composition, and function. Sports Health **1**, 461–468 (2009).

[97] Linn, F. C. & Sokoloff, L. Movement and composition of interstitial fluid of cartilage. Arthritis & Rheumatism **8**, 481–494 (1965).

[98] Loebel, C., Mauck, R. L. & Burdick, J. A. Local nascent protein deposition and remodelling guide mesenchymal stromal cell mechanosensing and fate in three-dimensional hydrogels .

[99] Collins, M. N. & Birkinshaw, C. Hyaluronic acid based scaffolds for tissue engineering—A review. Carbohydrate Polymers **92**, 1262–1279 (2013). URL http://www.ncbi.nlm.nih.gov/pubmed/23399155 http://linkinghub.elsevier.com/retrieve/pii/S0144861712010478.

[100] Chen, Y. & Schuh, C. A. Elasticity of Random Multiphase Materials: Percolation of the Stiffness Tensor. Journal of Statistical Physics **162**, 232–241 (2016).

[101] Vernerey, F. J. & Bryant, S. 'The role of percolation in hydrogel-based tissue engineering and bioprinting'. Current Opinion in Biomedical Engineering **15**, 68–74 (2020). URL https://doi.org/10.1016/j.cobme.2020.01.005.

[102] Saberi, A. A. Recent advances in percolation theory and its applications. Physics Reports **578**, 1–32 (2015). URL http://dx.doi.org/10.1016/j.physrep.2015.03.003.

[103] Akkiraju, H. & Nohe, A. Role of Chondrocytes in Cartilage Formation, Progression of Osteoarthritis and Cartilage Regeneration. Journal of developmental biology **3**, 177–192 (2015). URL http://www.ncbi.nlm.nih.gov/pubmed/27347486 http://www.pubmedcentral.nih.gov/articlerender.fcgi?artid=PMC4916494.

[104] Crapo, P. M., Gilbert, T. W. & Badylak, S. F. An overview of tissue and whole organ decellularization processes. Biomaterials **32**, 3233–3243 (2011). URL http://www.ncbi.nlm.nih.gov/pubmed/21296410.

[105] Reing, J. E. et al. The Effects of Processing Methods upon Mechanical and Biologic Properties of Porcine Dermal Extracellular Matrix Scaffolds .

[106] Eng, D., Caplan, M., Preul, M. & Panitch, A. Hyaluronan scaffolds: A balance between backbone functionalization and bioactivity. Acta Biomaterialia **6**, 2407–2414 (2010). URL http://linkinghub.elsevier.com/retrieve/pii/S174270610900590X.

[107] Rowland, C. R., Colucci, L. A. & Guilak, F. Fabrication of anatomically-shaped cartilage constructs using decellularized cartilage-derived matrix scaffolds (2016). URL http://dx.doi.org/10.1016/j.biomaterials.2016.03.012.

[108] Xue, J. et al. Repair of articular cartilage defects with acellular cartilage sheets in a swine model. Biomedical Materials **13**, 025016 (2018).

[109] Movasaghi, Z., Rehman, S. & Rehman, I. U. Raman spectroscopy of biological tissues. Applied Spectroscopy Reviews **42**, 493–541 (2007).

[110] Mariani, E., Lisignoli, G., Borzì, R. M. & Pulsatelli, L. Molecular Sciences Biomaterials: Foreign Bodies or Tuners for the Immune Response? (2019). URL www.mdpi.com/journal/ijms.

[111] Herzmann, N., Salamon, A., Fiedler, T. & Peters, K. Analysis of migration rate and chemotaxis of human adipose-derived mesenchymal stem cells in response to LPS and LTA in vitro. Experimental Cell Research **342**, 95–103 (2016). URL http://dx.doi.org/10.1016/j.yexcr.2016.03.016.

[112] Ofek, G., Natoli, R. M. & Athanasiou, K. A. In situ Mechanical Properties of the Chondrocyte Cytoplasm and Nucleus .

[113] Sutherland, A. J. et al. Decellularized Cartilage May Be a Chondroinductive Material for Osteochondral Tissue Engineering (2015).

[114] Wang, Z. et al. Cartilaginous extracellular matrix derived from decellularized chondrocyte sheets for the reconstruction of osteochondral defects in rabbits. Acta Biomaterialia **81**, 129–145 (2018). URL https://www.sciencedirect.com/science/article/pii/S1742706118305956f0045.

[115] Pati, F. et al. Printing three-dimensional tissue analogues with decellularized extracellular matrix bioink. Nature Communications **5**, 1–11 (2014). URL http://dx.doi.org/10.1038/ncomms4935.

[116] Wolf, M. T. et al. A hydrogel derived from decellularized dermal extracellular matrix. Biomaterials (2012).

[117] Novak, T., Voytik-Harbin, S. L. & Neu, C. P. Cell encapsulation in a magnetically aligned collagen-GAG copolymer microenvironment. Acta Biomater **11**, 274–282 (2015). URL http://www.ncbi.nlm.nih.gov/pubmed/25257315.

[118] Cheng, C. W., Solorio, L. D. & Alsberg, E. Decellularized tissue and cell-derived extracellular matrices as scaffolds for orthopaedic tissue engineering. Biotechnol Adv **32**, 462–484 (2014). URL http://www.ncbi.nlm.nih.gov/pubmed/24417915.

[119] Huang, L. K. & Wang, M. J. J. Image thresholding by minimizing the measures of fuzziness. Pattern Recognition **28**, 41–51 (1995).

[120] Nih, Od, Oer & Olaw. Guide for the Care and Use of Laboratory Animals (2011). URL http://www.nap.edu.

[121] Do, A.-V., Khorsand, B., Geary, S. M. & Salem, A. K. 3D Printing of Scaffolds for Tissue Regeneration Applications. Advanced healthcare materials **4**, 1742–62 (2015). URL http://www.ncbi.nlm.nih.gov/pubmed/26097108 http://www.pubmedcentral.nih.gov/articlerender.fcgi?artid=PMC4597933.

[122] Goldring, S. R. & Goldring, M. B. Changes in the osteochondral unit during osteoarthritis: Structure, function and cartilage bone crosstalk. Nature Reviews Rheumatology **12**, 632–644 (2016). URL http://www.nature.com/doifinder/10.1038/nrrheum.2016.148.

[123] Luo, L., Chu, J. Y. J., Eswaramoorthy, R., Mulhall, K. J. & Kelly, D. J. Engineering Tissues That Mimic the Zonal Nature of Articular Cartilage Using Decellularized Cartilage Explants Seeded with Adult Stem Cells .

[124] Aisenbrey, E. A. et al. A Stereolithography-Based 3D Printed Hybrid Scaffold for In Situ Cartilage Defect Repair. Macromolecular Bioscience **18**, 1700267 (2018). URL http://doi.wiley.com/10.1002/mabi.201700267.

[125] Sears, N. A., Seshadri, D. R., Dhavalikar, P. S. & Cosgriff-Hernandez, E. A Review of Three-Dimensional Printing in Tissue Engineering. Tissue Engineering Part B: Reviews **22**, 298–310 (2016). URL https://www.liebertpub.com/doi/10.1089/ten.teb.2015.0464.

[126] Hung, K. C., Tseng, C. S., Dai, L. G. & Hsu, S. h. Water-based polyurethane 3D printed scaffolds with controlled release function for customized cartilage tissue engineering. Biomaterials **83**, 156–168 (2016).

[127] Lai, Y. et al. Porous composite scaffold incorporating osteogenic phytomolecule icariin for promoting skeletal regeneration in challenging osteonecrotic bone in rabbits. Biomaterials **153**, 1–13 (2018). URL

[128] Yang, X. et al. Collagen-alginate as bioink for three-dimensional (3D) cell printing based cartilage tissue engineering. Materials Science and Engineering C **83**, 195–201 (2018).

[129] Choi, J. S. et al. Human extracellular matrix (ECM) powders for injectable cell delivery and adipose tissue engineering. Journal of Controlled Release **139**, 2–7 (2009).

[130] Eckstein, F., Hudelmaier, M. & Putz, R. The effects of exercise on human articular cartilage (2006). URL /pmc/articles/PMC2100201/?report=abstract https://www.ncbi.nlm.nih.gov/pmc/articles/PMC2100201/.

[131] Mow, V. C. & Guo, X. E. Mechano-Electrochemical Properties of Articular Cartilage: Their Inhomogeneities and Anisotropies. Annu. Rev. Biomed. Eng **4**, 175–209 (2002). URL www.annualreviews.org.

[132] Wahlquist, J. A. et al. Indentation mapping revealed poroelastic, but not viscoelastic, properties spanning native zonal articular cartilage. Acta Biomaterialia **64**, 41–49 (2017).

[133] Neu, C. P., Komvopoulos, K. & Reddi, A. H. The interface of functional biotribology and regenerative medicine in synovial joints. Tissue Eng Part B Rev **14**, 235–247 (2008). URL http://www.ncbi.nlm.nih.gov/pubmed/18601586.

[134] Lin, W., Liu, Z., Kampf, N. & Klein, J. The Role of Hyaluronic Acid in Cartilage Boundary Lubrication. Cells **9** (2020). URL /pmc/articles/PMC7407873/?report=abstract https://www.ncbi.nlm.nih.gov/pmc/articles/PMC7407873/.

[135] Singh, A. et al. Enhanced lubrication on tissue and biomaterial surfaces through peptide-mediated binding of hyaluronic acid (2014).

[136] Swann, D. A. et al. Role of hyaluronic acid in joint lubrication. Annals of the Rheumatic Diseases **33**, 318–326 (1974). URL http://ard.bmj.com/.

[137] Park, S., Costa, K. D. & Ateshian, G. A. Microscale frictional response of bovine articular cartilage from atomic force microscopy. Journal of Biomechanics **37**, 1679–1687 (2004).

[138] Cigan, A. D. et al. Nutrient channels and stirring enhanced the composition and stiffness of large cartilage constructs. Journal of Biomechanics **47**, 3847–3854 (2014). URL http://dx.doi.org/10.1016/j.jbiomech.2014.10.017.

[139] Daly, A. C., Sathy, B. N. & Kelly, D. J. Engineering large cartilage tissues using dynamic bioreactor culture at defined oxygen conditions. Journal of Tissue Engineering **9** (2018).

[140] Ge, Z., Li, C., Heng, B. C., Cao, G. & Yang, Z. Functional biomaterials for cartilage regeneration. J Biomed Mater Res A **100**, 2526–2536 (2012). URL http://www.ncbi.nlm.nih.gov/pubmed/22492677.

[141] Jürgensen, K., Aeschlimann, D., Cavin, V., Genge, M. & Hunziker, E. B. A new biological glue for cartilage-cartilage interfaces: Tissue transglutaminase. Journal of Bone and Joint Surgery - Series A **79**, 185–193 (1997). URL https://pubmed.ncbi.nlm.nih.gov/9052538/.

Appendix A

Supplementary Figures

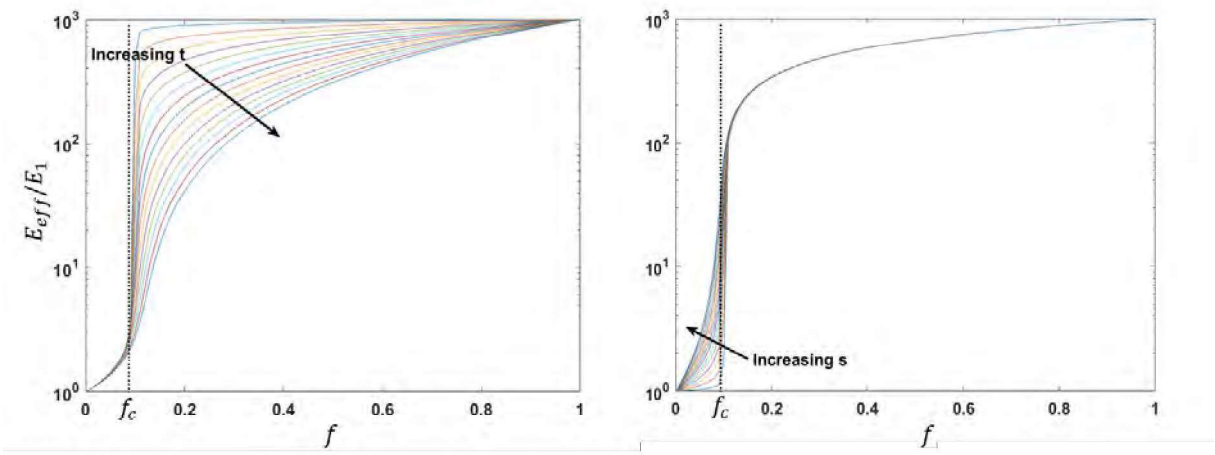

Figure A.1: Plots of the ratio of effective compressive modulus predicted by the GEM theory as a function of the volume fraction f of cartilage. The difference in the sharpness of transition from the modulus of the hydrogel E_1 to that of cartilage E_2 assumed to be 1000 times higher is illustrated with changes in the exponents s and t.

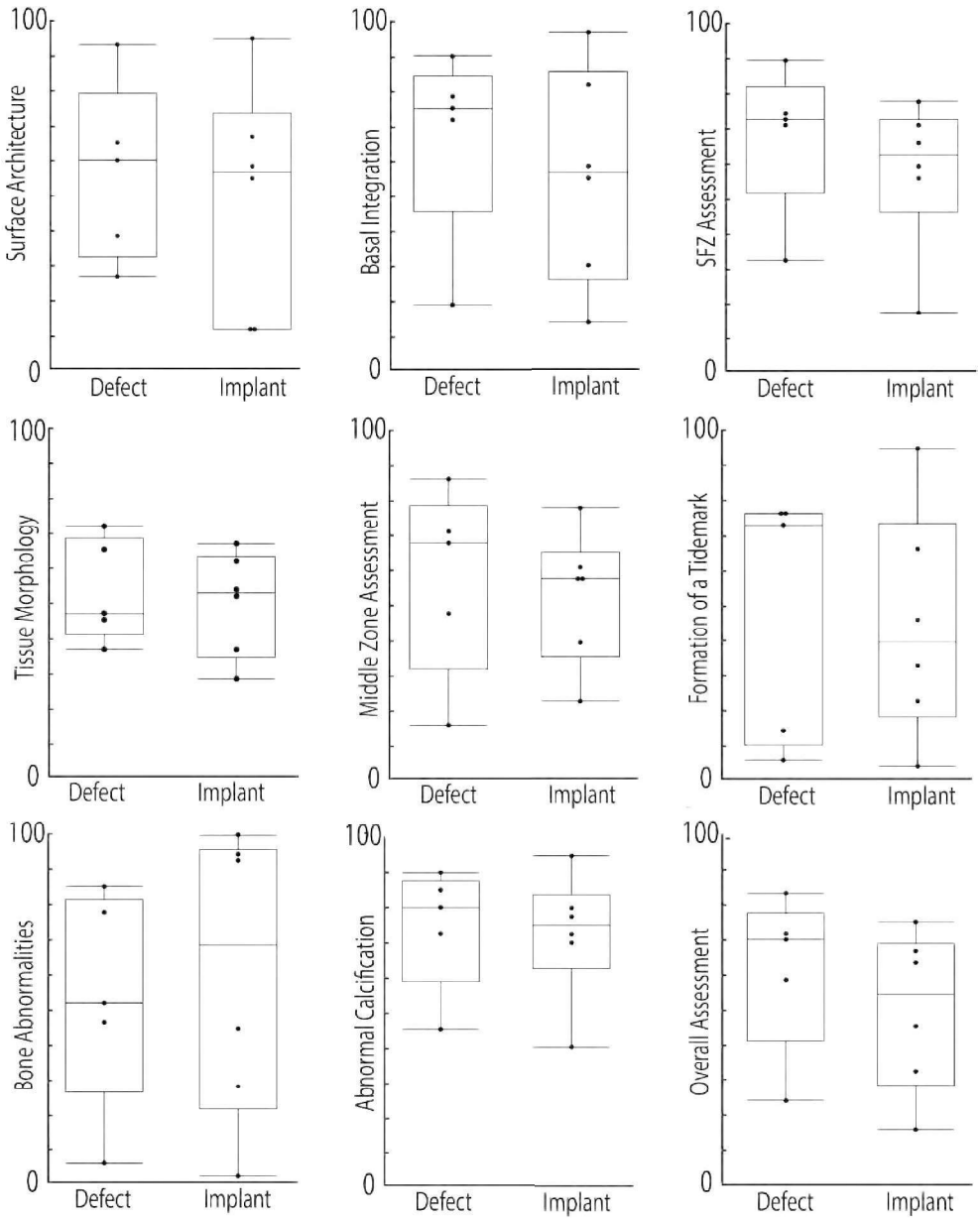

Figure A.2: ICRS II Scoring. ICRS II visual histological score comparisons between the defect and implant groups. Scoring was completed by 3 blinded and independent observers. For detailed instruction on how images were scored, reference ICRS II guidelines [75]. For all categories, a score of 100 indicates identical to native articular cartilage, where a score of 0 indicates no similarities to native cartilage.

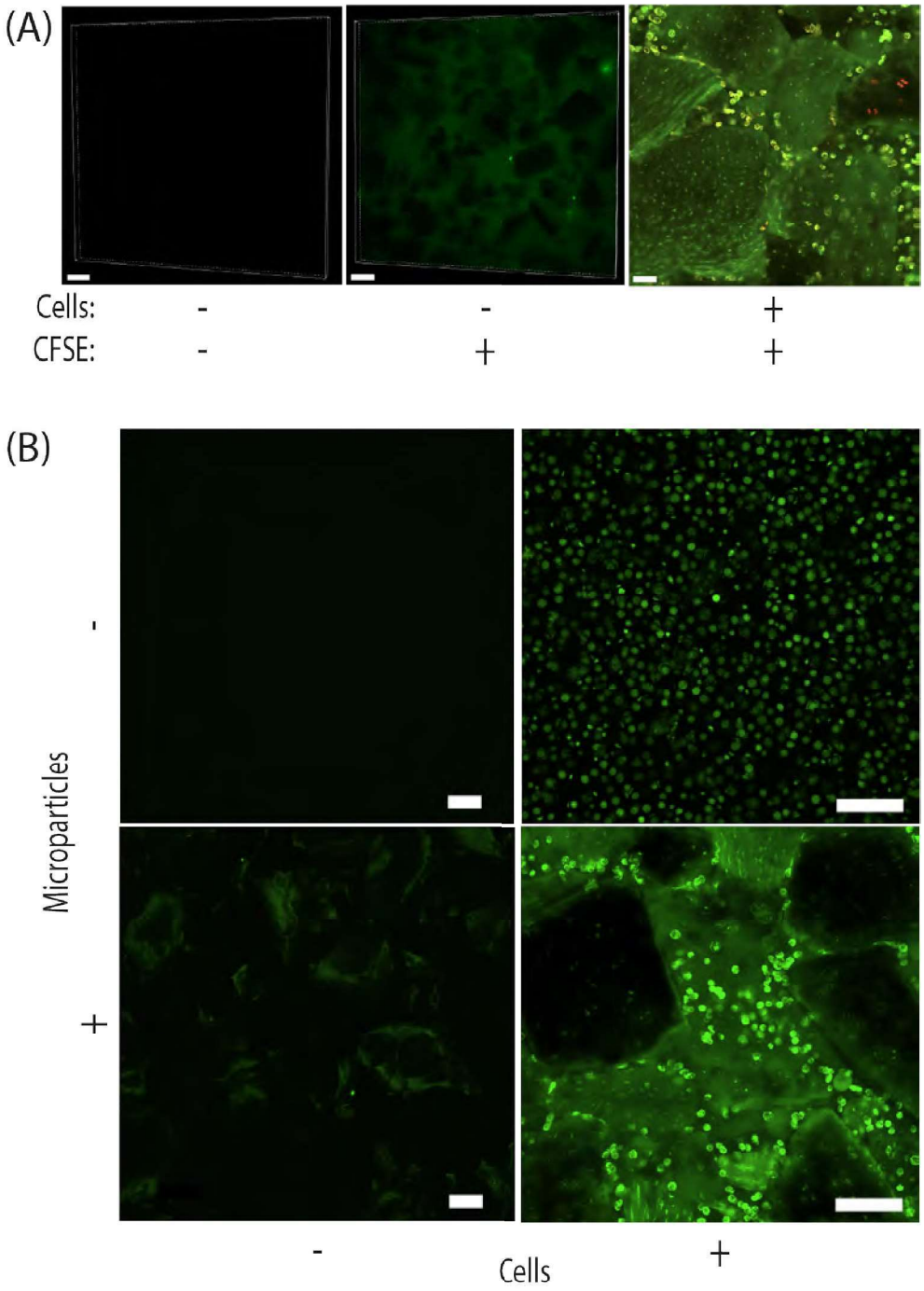

Figure A.3: Confirmation of CFSE staining of chondrocytes. (A) The addition of representative levels of CFSE to the microparticle gels does not show any bright localization to the particles. (B) Additionally, we do not observe staining due to imaging by confocal microscopy, or the microparticles alone, and we only observe a localization of signal with the addition of cells. Scale Bar = 100µm, final panel of (A), scale bar = 50µm.

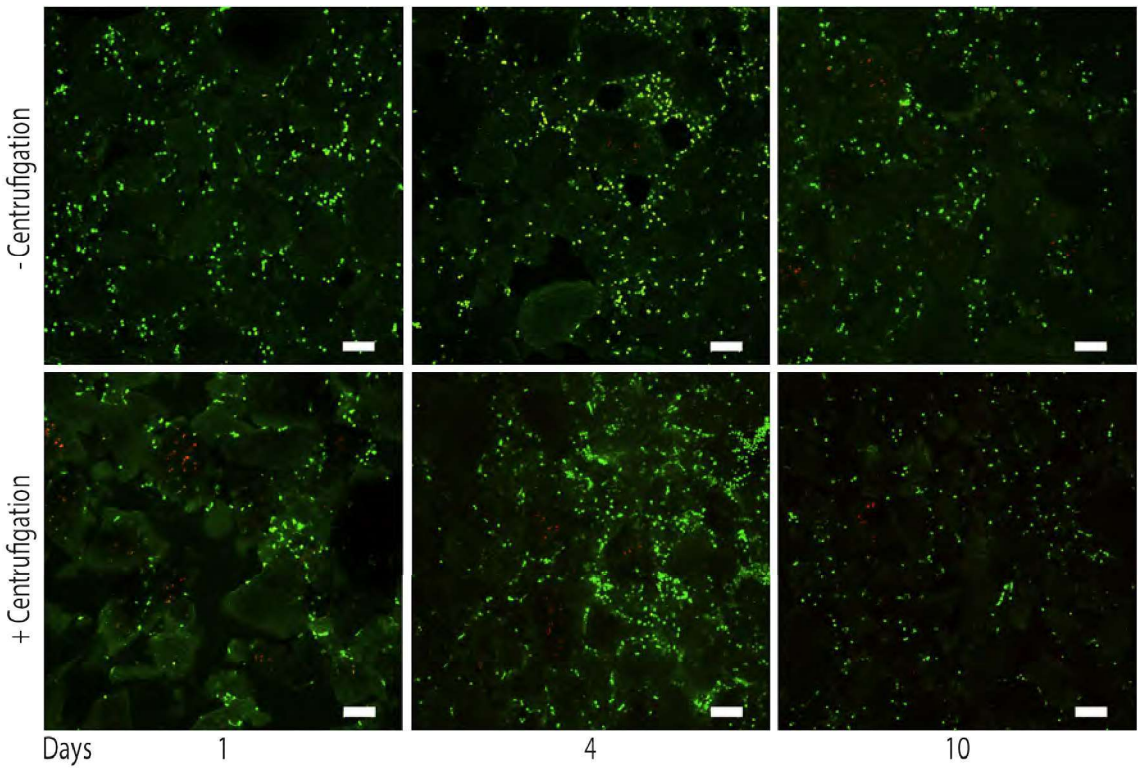

Figure A.4: Post-centrifugation live/dead staining. Live dead staining of the cells before and after centrifugation (scaffold packing) demonstrates no dramatic increase in cell death. Green = Live cells, Red = Dead cells. Scale Bar = 100µm.

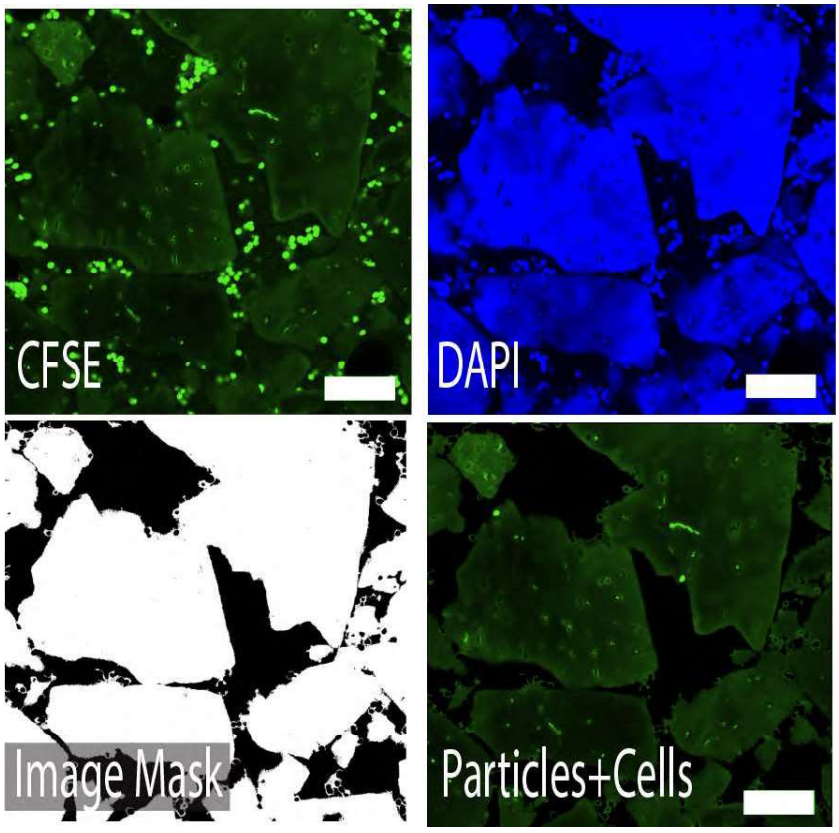

Figure A.5: Custom thresholding enabled quantification of the number of CFSE-stained cells that migrated into particles. Thresholding the particles using DAPI stain in the 405 nm channel allowed us to subtract the background. Once all cells in the hydrogel were subtracted from the background, particle measuring tools in ImageJ enabled quantification of CFSE stained cells in the particles at each time point. Scale Bar = 100µm.

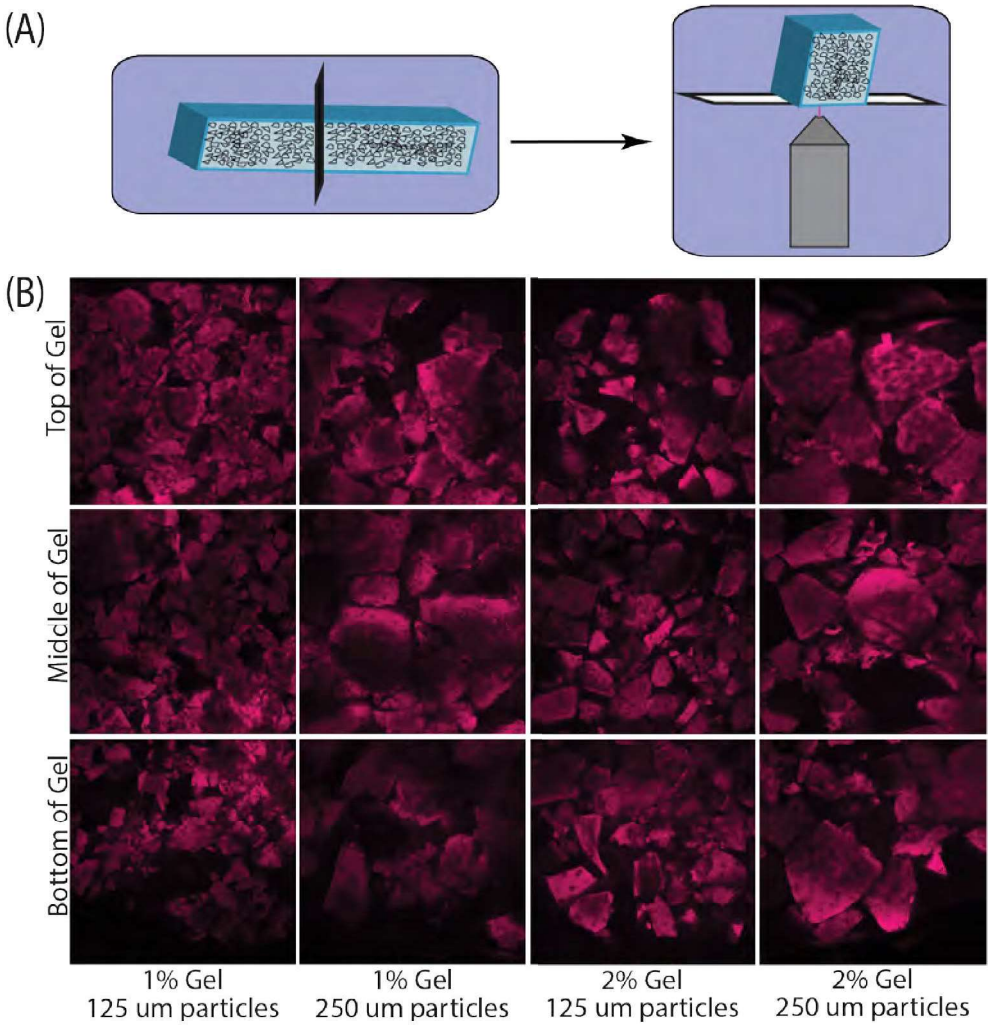

Figure A.6: Particle packing was consistent throughout large volumes of the engineered materials. Tissue clays maintain the volume density of particles throughout the depth of the scaffold; particles do not pack in higher density at the base of the scaffold. (A) Polymerized scaffolds are bisected and imaged throughout the depth, (B) Particles of different sizes in HA/PEGDA gels of differing densities pack evenly throughout the depth of the scaffold.

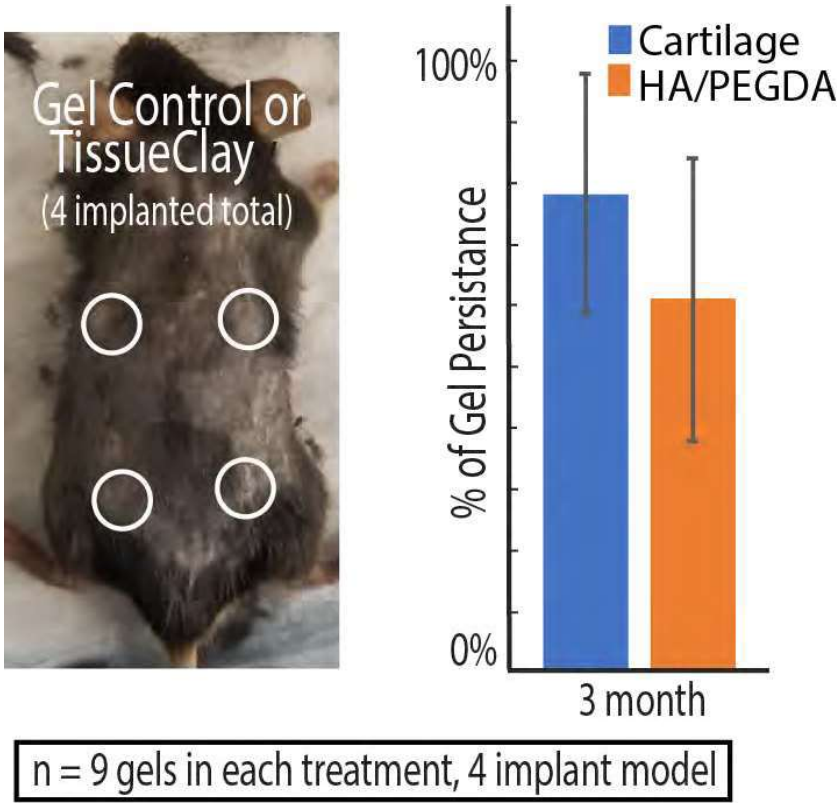

Figure A.7: Supplemental hydrogel persistance study over 3 months. In a supplementary subcutaneous mouse study, we implanted 4 gels (2 tissue clay hydrogels and 2 HA/PEGDA controls) in 3 different mice (gel type randomized among the 4 highlighted locations). Data shown here represent the hydrogel persistence over 3 months and the trends agree with the persistence results reported in the chapter 3.

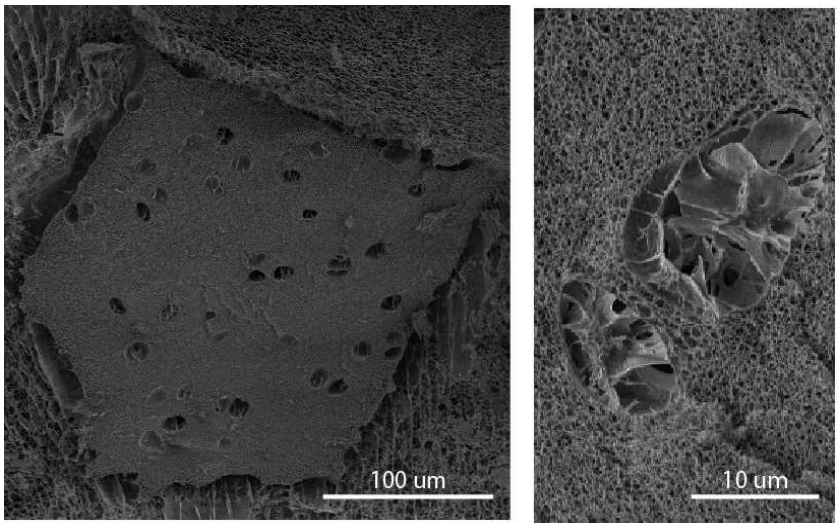

Figure A.8: Scanning electron microscopy images of acellular tissue particles. Regions previously formed for chondrons are 10-15 µm in diameter, providing several regions of much larger pores than the surrounding cartilage extracellular matrix (images taken by Tyler Novak).